

AD-A045 349

AIR FORCE INST OF TECH WRIGHT-PATTERSON AFB OHIO  
SURFACE CRACKS EMANATING FROM FASTENER HOLES. (U)

1976 T E KULLGREN  
AFIT-CI-77-21

UNCLASSIFIED

F/6 20/11

NL

1 OF 3  
AD  
A045349

1	2	3	4	5	6	7	8	9	10	11	12	13	14	15	16	17	18	19	20	21	22	23	24	25	26	27	28	29	30	31	32	33	34	35	36	37	38	39	40	41	42	43	44	45	46	47	48	49	50	51	52	53	54	55	56	57	58	59	60	61	62	63	64	65	66	67	68	69	70	71	72	73	74	75	76	77	78	79	80	81	82	83	84	85	86	87	88	89	90	91	92	93	94	95	96	97	98	99	100
---	---	---	---	---	---	---	---	---	----	----	----	----	----	----	----	----	----	----	----	----	----	----	----	----	----	----	----	----	----	----	----	----	----	----	----	----	----	----	----	----	----	----	----	----	----	----	----	----	----	----	----	----	----	----	----	----	----	----	----	----	----	----	----	----	----	----	----	----	----	----	----	----	----	----	----	----	----	----	----	----	----	----	----	----	----	----	----	----	----	----	----	----	----	----	----	----	----	----	-----

AD-A045349

J

77-21



0  
Department of  
Mechanical Engineering  
Colorado State University

DISSERTATION

SURFACE CRACKS EMANATING  
FROM FASTENER HOLES

THOMAS EDWARD KULLGREN

AD No.

DDC FILE COPY

D D C

REF ID: A651120  
OCT 20 1977

D

DISTRIBUTION STATEMENT A  
Approved for public release;  
Distribution Unlimited

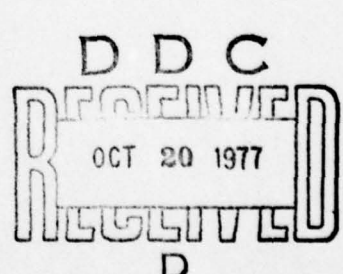
ACCESSION FOR	
#718	WHITE Section <input checked="" type="checkbox"/>
UGC	Buff Section <input type="checkbox"/>
UNANNOUNCED <input type="checkbox"/>	
JUSTIFICATION	
BY	
DISTRIBUTION/AVAILABILITY CODES	
DIST.	AVAIL. AND/OF SPECIAL
A	

DISSERTATION

SURFACE CRACKS EMANATING FROM FASTENER HOLES

Submitted by  
Thomas Edward Kullgren

In partial fulfillment of the requirements  
for the Degree of Doctor of Philosophy  
Colorado State University  
Fort Collins, Colorado  
Summer, 1976



**DISTRIBUTION STATEMENT A**  
Approved for public release;  
Distribution Unlimited

UNCLASSIFIED

(14) SECURITY CLASSIFICATION OF THIS PAGE (When Data Entered)		READ INSTRUCTIONS BEFORE COMPLETING FORM	
<b>AFIT</b> <b>REPORT DOCUMENTATION PAGE</b> REPORT NUMBER <b>CI-77-21</b>		2. GOVT ACCESSION NO. 3. SPECIDENTIC CATALOG NUMBER <b>9) Doctoral thesis</b>	
4. TITLE (and Subtitle) <b>Surface Cracks Emanating From Fastener Holes</b>		5. TYPE OF REPORT & PERIOD COVERED <b>Dissertation</b>	
6. PERFORMING ORG. REPORT NUMBER <b>10) THOMAS EDWARD KULLGREN</b> MAJOR, USAF		8. CONTRACT OR GRANT NUMBER(s)	
9. PERFORMING ORGANIZATION NAME AND ADDRESS <b>AFIT Student at Colorado State University, Fort Collins, Colorado</b>		10. PROGRAM ELEMENT, PROJECT, TASK AREA & WORK UNIT NUMBERS <b>11) Summer 1976</b>	
11. CONTROLLING OFFICE NAME AND ADDRESS <b>AFIT/CI Wright-Patterson AFB OH 45433</b>		12. REPORT DATE <b>13. NUMBER OF PAGES 181 pages</b>	
14. MONITORING AGENCY NAME & ADDRESS (if different from Controlling Office) <b>12) 201 p.</b>		15. SECURITY CLASS. (of this report) <b>16) Classified</b> CLASSIFICATION/DOWNGRADING SCHEDULE	
16. DISTRIBUTION STATEMENT (of this Report) <b>Approved for Public Release; Distribution Unlimited</b>			
17. DISTRIBUTION STATEMENT (of the abstract entered in Block 20, if different from Report) <b>18) JERAL F. GUESS, Captain, USAF APPROVED FOR PUBLIC RELEASE AFR 190-17. Director of Information, AFIT</b>			
19. KEY WORDS (Continue on reverse side if necessary and identify by block number)			
20. ABSTRACT (Continue on reverse side if necessary and identify by block number) <b>Attached</b>			

COLORADO STATE UNIVERSITY

JULY, 1976

WE HEREBY RECOMMEND THAT THE THESIS PREPARED UNDER OUR SUPERVISION  
BY THOMAS EDWARD KULLGREN ENTITLED SURFACE CRACKS EMANATING FROM  
FASTENER HOLES BE ACCEPTED AS FULFILLING IN PART REQUIREMENTS FOR THE  
DEGREE OF DOCTOR OF PHILOSOPHY.

Committee on Graduate Work

AB Kellogg  
Harry O. Ryner  
Frederick Smith  
Adviser

James P. Goodwin  
Eric Thompson

## ABSTRACT OF DISSERTATION

### SURFACE CRACKS EMANATING FROM FASTENER HOLES

The finite element-alternating method is used to determine stress intensity factors along the periphery of a part-elliptical crack emanating from a fastener hole in a finite-thickness plate. A sequence of iterations is performed between an analytic solution for an elliptical crack embedded in an infinite solid and a finite element solution for the uncracked plate with a fastener hole. The technique determines the stress field near the crack, the stress intensity factor and the crack opening displacements.

Mode-one stress intensity factors around the crack front are presented for three classes of crack location relative to the hole and numerous crack shapes and sizes. Calculations are performed for cracks emanating from both loaded and unloaded fastener holes. Crack opening displacements for all cases are presented.

The results of this study are compared with static fracture tests in polymethylmethacrylate and with experiments and estimates of other authors.

Thomas Edward Kullgren  
Department of Mechanical Engineering  
Colorado State University  
Fort Collins, Colorado 80523  
Summer, 1976

#### ACKNOWLEDGEMENT

The author wishes to express his appreciation to his advisor, Dr. Fred W. Smith, who provided continued guidance and encouragement during the course of this work. Additionally, without the sponsorship of Colonel Wallace E. Fluhr and the support of the United States Air Force Academy and the Air Force Institute of Technology, this study would not have been possible. Thanks go also to Major William M. Browning and Major Gary P. Ganong for their many hours of discussion regarding this work and to Merle Schwartzberg for her technical assistance in the experiments. Last, but surely not least, a special note of thanks is due my wife, Bonnie, and my two daughters for their support, encouragement, and understanding during the course of this work.

## TABLE OF CONTENTS

	<u>Page</u>
LIST OF TABLES . . . . .	vii
LIST OF FIGURES. . . . .	ix
CHAPTER	
1 INTRODUCTION . . . . .	1
1.1 Motivation for Study of Cracks Emanating from Fastener Holes. . . . .	1
1.2 Previous Work Leading to Stress Intensity Factors for Cracks Emanating from Open Fastener Holes . . . . .	2
1.3 Previous Work on Stress Fields in Plates with Loaded Fastener Holes. . . . .	8
1.4 Objectives . . . . .	11
2 THEORETICAL APPROACH . . . . .	13
2.1 General Problem Statement. . . . .	13
2.2 General Solution Method. . . . .	13
2.3 Previous Work. . . . .	14
2.4 Accuracy and Sensitivity Test of the Method. . .	16
2.5 Theoretical Solution Results for Single Quarter-Elliptical Cracks Emanating from an Open Fastener Hole. . . . .	20
2.6 Comparison of Theoretical Results with Two Independent Experiments. . . . .	27
3 DOUBLE SURFACE CRACKS EMANATING FROM AN OPEN FASTENER HOLE . . . . .	32
3.1 Problem Statement. . . . .	32
3.2 Finite Element Mesh Configuration. . . . .	32
3.3 Changes to the Finite Element-Alternating Method for the Double Crack Problem. . . . .	33
3.4 Three-Dimensional Analysis of a Two- Dimensional Test Problem . . . . .	34

CHAPTER	<u>Page</u>
3.5 Solution Results . . . . .	35
3.6 Comparison with an Estimate of Another Author . .	38
4 EMBEDDED CRACKS EMANATING FROM AN OPEN FASTENER HOLE . .	40
4.1 Problem Statement. . . . .	40
4.2 Finite Element Mesh Configuration. . . . .	40
4.3 Solution Results . . . . .	41
4.4 Comparisons with Estimates and Solutions of Other Authors. . . . .	43
5 CRACKS EMANATING FROM LOADED FASTENER HOLES. . . . .	47
5.1 Problem Statement. . . . .	47
5.2 Theoretical Approach . . . . .	47
5.3 Problem Modeling and Assumptions . . . . .	47
5.4 Calculation of Crack Plane Stress Distributions. . . . .	50
5.5 Theoretical Stress Intensity Factor Results for Cracks Emanating from Loaded Fastener Holes. . . . .	54
5.6 Stress Intensity Factors for Partial Load Transfer to the Fastener . . . . .	55
5.7 Comparison with Results of Other Authors . . . .	57
6 STATIC FRACTURE TESTS. . . . .	59
6.1 Introduction . . . . .	59
6.2 Modeling of the Fracture Process with PMMA . . .	59
6.3 Specimen Preparation . . . . .	60
6.4 Slow Growth in PMMA. . . . .	62
6.5 Specimen Testing . . . . .	63
6.6 Data Reduction . . . . .	64
6.7 Comparison of Theory with Experiments. . . . .	67

CHAPTER	<u>Page</u>
6.8 Some Observations on Crack Growth in the Present Experiments. . . . .	71
7 CRACK OPENING DISPLACEMENTS. . . . .	75
7.1 Problem Statement. . . . .	75
7.2 Solution Method. . . . .	75
7.3 Solution Results . . . . .	79
8 CONCLUSION . . . . .	80
8.1 Discussion . . . . .	80
8.2 Recommendations. . . . .	81
REFERE . . . . .	82
APPENDICES . . . . .	168
A Finite Element-Alternating Method Calculations and Stress Function Coefficients . . . . .	168
B Crack Opening Displacement Equation. . . . .	175
C Benchmark Problem. . . . .	176

## LIST OF TABLES

## LIST OF FIGURES

<u>Figure</u>		<u>Page</u>
1.1	A Single Through-Crack Emanating from a Hole in a Plate. . . . .	88
1.2	Double Through-Cracks Emanating from a Hole in a Plate . . . . .	89
1.3	A Finite Body Without a Crack, Subject to Surface Tractions . . . . .	90
1.4	An Elliptical Crack in an Infinite Solid. . . . .	91
1.5	Plate Loading Conditions. . . . .	92
2.1	Crack Types and Locations Relative to a Fastener Hole .	93
2.2	Finite Element-Alternating Method, Two Iterations . . .	94
2.3	Three-Dimensional Approximation of a Two-Dimensional Problem . . . . .	95
2.4	112-Element Finite Element Mesh, Single Corner Crack Problem, $d/t=1.0$ . . . . .	96
2.5	112-Element Finite Element Mesh, Single Corner Crack Problem, $d/t=0.5$ . . . . .	97
2.6	Magnification Factor Versus Angle from Front Surface, Single Corner Cracks, $a/t=0.9$ , $d/t=1.0$ , $Q/P=0.0$ . . .	98

Figure	Page
2.7 Magnification Factor Versus Angle from Front Surface, Single Corner Cracks, $a/t=0.75$ , $d/t=1.0$ , $Q/P=0.0$ . . .	99
2.8 Magnification Factor Versus Angle from Front Surface, Single Corner Cracks, $a/t=0.5$ , $d/t=1.0$ , $Q/P=0.0$ . . .	100
2.9 Magnification Factor Versus Angle from Front Surface, Single Corner Cracks, $a/t=0.25$ , $d/t=1.0$ , $Q/P=0.0$ . . .	101
2.10 Magnification Factor Versus Angle from Front Surface, Single Corner Cracks, $a/c=0.25$ , $a/t=0.125$ , $d/t=1.0$ , $Q/P=0.0$ . . . . .	102
2.11 Magnification Factor Versus Angle from Front Surface, Single Corner Cracks, $a/c=0.50$ , $a/t=0.25$ , $Q/P=0.0$ . . .	103
2.12 Comparison of Magnification Factor at the Hole, Single Corner Crack, Open Hole . . . . .	104
2.13 Comparison of Magnification Factor at the Front Surface, Single Corner Crack, Open Hole. . . . .	105
2.14 Comparison of Magnification Factor at the Hole, Single Corner Crack, Open Hole . . . . .	106
2.15 Comparison of Magnification Factors at the Front Surface, Single Corner Crack, Open Hole. . . . .	107
3.1 108-Element Finite Element Mesh, Double Corner Crack Problem, $d/t=1.0$ . . . . .	108

<u>Figure</u>	<u>Page</u>
3.2 108-Element Finite Element Mesh, Double Corner Crack Problem, $d/t=0.5$ . . . . .	109
3.3 Three-Dimensional Approximation of a Two-Dimensional Problem . . . . .	110
3.4 Magnification Factor Versus Angle from Front Surface, Double Corner Cracks, $a/t=0.9$ , $d/t=1.0$ , $Q/P=0.0$ . . .	111
3.5 Magnification Factor Versus Angle from Front Surface, Double Corner Cracks, $a/t=0.75$ , $d/t=1.0$ , $Q/P=0.0$ . . .	112
3.6 Magnification Factor Versus Angle from Front Surface, Double Corner Cracks, $a/t=0.5$ , $d/t=1.0$ , $Q/P=0.0$ . . .	113
3.7 Magnification Factor Versus Angle from Front Surface, Double Corner Crack, $a/c=0.5$ , $a/t=0.25$ , $d/t=1.0$ , $Q/P=0.0$ . . .	114
3.8 Magnification Factor Versus Angle from Front Surface, Double Corner Crack, $a/c=0.25$ , $a/t=0.125$ , $d/t=1.0$ , $Q/P=0.0$ . . .	115
3.9 Magnification Factor Versus Angle from Front Surface, Double Corner Cracks, $a/c=0.25$ , $a/t=0.125$ , $Q/P=0.0$ . .	116
4.1 112-Element Finite Element Mesh, Embedded Crack Problem, $d/t=1.0$ . . . . .	117

<u>Figure</u>		<u>Page</u>
4.2	112-Element Finite Element Mesh, Embedded Crack Problem, $d/t=0.5$ . . . . .	118
4.3	Magnification Factor Versus Angle from Minor Axis, Embedded Cracks, $a/t=0.125$ , $d/t=1.0$ , $Q/P=0.0$ . . . . .	119
4.4	Magnification Factor Versus Angle from Minor Axis, Embedded Cracks, $a/t=0.25$ , $d/t=1.0$ , $Q/P=0.0$ . . . . .	120
4.5	Magnification Factor Versus Angle from Minor Axis Embedded Cracks, $a/c=0.5$ , $d/t=1.0$ , $Q/P=0.0$ . . . . .	121
4.6	Magnification Factor Versus Angle from Minor Axis, Embedded Crack, $a/c=0.75$ , $d/t=1.0$ , $Q/P=0.0$ . . . . .	122
4.7	Magnification Factor Versus Angle from Minor Axis, Embedded Cracks, $a/c=0.50$ , $a/t=0.125$ , $Q/P=0.0$ . . . . .	123
4.8	Comparison of Present Results with Another Author's Estimate. . . . .	124
4.9	Comparative Parametric Plot, Estimates by Another Author Versus Present Solution Results. . . . .	125
4.10	Comparative Parametric Plot, Solution by Another Author Versus Present Solution Results. . . . .	126
5.1	96-Element Finite Element Mesh Used to Generate Crack Plane Stresses for Loaded Fastener Hole Cases . . . . .	127



<u>Figure</u>	<u>Page</u>
5.12 Magnification Factor Versus Angle from Minor Axis, Embedded Cracks, $a/c=0.5$ , $a/t=0.125$ , $d/t=1.0$ . . . . .	138
5.13 Magnification Factor Versus Angle from Minor Axis, Embedded Cracks, $a/c=0.5$ , $a/t=0.125$ , $d/t=0.5$ . . . . .	139
5.14 Superposition for Cases of Partial Load Transfer to a Fastener. . . . .	140
6.1 Cracking Jig for Growing Shallow Single and Double Corner Cracks . . . . .	141
6.2 Experimental Loading Arrangements . . . . .	142
6.3 Typical Fractured Surfaces in PMMA Specimen with Cracks Emanating from Fastener Holes . . . . .	143
6.4 Load-Displacement Record, Double Corner Cracks at an Open Fastener Hole. . . . .	144
6.5 PMMA Baseline Test, Plate No. 1 . . . . .	145
6.6 PMMA Baseline Test, Plate No. 2 . . . . .	146
6.7 Comparison of Theory and PMMA Experiments, Single Corner Crack, $d/t=1.0$ , $Q/P=0.0$ . . . . .	147
6.8 Comparison of Theory and PMMA Experiments, Single Corner Crack, $d/t=1.0$ , $Q/P=0.0$ . . . . .	148
6.9 Comparison of Theory and PMMA Experiments, Single Corner Crack, $d/t=1.0$ , $Q/P=1.0$ . . . . .	149

<u>Figure</u>		<u>Page</u>
6.10	Comparison of Theory and PMMA Experiments, Single Corner Crack, $d/t=1.0$ , $Q/P=1.0$ . . . . .	150
6.11	Comparison of Theory and PMMA Experiments, Double Corner Cracks, $d/t=1.0$ , $Q/P=0.0$ . . . . .	151
6.12	Comparison of Theory and PMMA Experiments, Double Corner Cracks, $d/t=1.0$ , $Q/P=0.0$ . . . . .	152
6.13	Comparison of Theory and PMMA Experiments, Double Corner Cracks, $d/t=1.0$ , $Q/P=1.0$ . . . . .	153
6.14	Comparison of Theory and PMMA Experiments, Double Corner Cracks, $d/t=1.0$ , $Q/P=1.0$ . . . . .	154
6.15	Comparison of Theory and PMMA Experiments, Embedded Crack, $d/t=1.0$ , $Q/P=0.0$ . . . . .	155
6.16	Comparison of Theory and PMMA Experiments, Embedded Crack, $d/t=1.0$ , $Q/P=1.0$ . . . . .	156
6.17	Comparison of Theory and PMMA Experiments, Single Corner Crack, $d/t=0.5$ , $Q/P=0.0$ . . . . .	157
6.18	Comparison of Theory and PMMA Experiments, Single Corner Crack, $d/t=0.5$ , $Q/P=0.0$ . . . . .	158
6.19	Comparison of Theory and PMMA Experiments, Double Corner Cracks, $d/t=0.5$ , $Q/P=0.0$ . . . . .	159

<u>Figure</u>		<u>Page</u>
6.20	Comparison of Theory and PMMA Experiments, Double Corner Cracks, $d/t=0.5$ , $Q/P=0.0$ . . . . .	160
6.21	Comparison of Theory and PMMA Experiments, Embedded Crack, $d/t=0.5$ , $Q/P=0.0$ . . . . .	161
6.22	Comparison of Theory and PMMA Experiments, Embedded Crack, $d/t=0.5$ , $Q/P=1.0$ . . . . .	162
6.23	Difference Between Theoretical and Experimental Results as a Function of Maximum Local Crack Plane Normal Stress in the Experiments. . . . .	163
6.24	Parametric Plot of Theory to Approximate Slow Growth, Single Corner Crack, $c/t=0.5$ , $d/t=1.0$ . . . . .	164
6.25	Parametric Plot of Theory to Approximate Slow Growth, Single Corner Crack, $d/t=1.0$ . . . . .	165
6.26	Parametric Plot of Theory to Approximate Slow Growth, Embedded Crack, $a/t=0.125$ , $d/t=1.0$ . . . . .	166
7.1	Crack Opening Displacement, Single Corner Flaw Adjacent to Open Fastener Hole, $a/c=2.0$ , $a/t=0.9$ . . . . .	167
C-1	Magnification Factor Versus Angle from Front Surface, Single Corner Crack, Benchmark Problem, $a/c=2.0$ , $a/t=0.2$ , $d/t=1.0$ , $Q/P=0.0$ . . . . .	179

<u>Figure</u>	<u>Page</u>
C-2 Magnification Factor Versus Angle from Front Surface, Single Corner Crack, Benchmark Problem, $a/c=2.0$ , $a/t=0.2$ , $d/t=1.0$ , $Q/P=1.0$ . . . . .	180
C-3 Parametric Plot of Theoretical Results, Single Corner Cracks, Open Hole, $a/c=2.0$ . . . . .	181

## CHAPTER 1

### INTRODUCTION

#### 1.1 Motivation for Study of Cracks Emanating from Fastener Holes

Cracks in aerospace structures have caused catastrophic failures resulting in loss of life, destruction of millions of dollars in equipment and severely reduced operational capabilities. While the elimination of possibilities for crack initiation and growth is a worthwhile endeavor, the fact remains that flaws due to material defects, manufacturing methods, and in-service conditions will always be present to some extent. This simple admission opens the door to design against failure in the presence of flaws existing at the onset of operational use and during periods of fatigue growth. The fact that a crack exists is, by itself, no longer a criteria for the scrapping of an aerospace system nor is it sufficient reason for extensive modifications.

The United States Air Force is currently developing a design criteria (1)\* to reduce the possibility of catastrophic failures caused by crack-like defects. This criteria will be established on the basis of three separate yet interdependent studies:

1. At the beginning of a particular operational period, determine the most serious initial crack which could exist in a structure and predict the most severe operational conditions that could occur.
2. Determine the crack sizes which would cause catastrophic failure.

---

\*Numbers in parentheses refer to references listed at the end of the text.

3. Using predicted system operational data, calculate the time or number of cycles for existing cracks to grow to critical size.

The first and last studies listed are largely measurement oriented and thus perhaps more easily completed than the frequently complicated theoretical problem posed by the second study. It is to the partial completion of the second study that this work is dedicated.

A comprehensive review of aerospace structural failures completed by the United States Air Force in 1971 (2) showed the origin of failures due to cracks, in order of increasing frequency of occurrence, to be:

1. Surface cracks
2. Corner cracks
3. Cracks emanating from fastener holes

A full one-third of all failures studied were due to cracks emanating from fastener holes. While progress in the solution of surface and corner crack problems has been promising, only two direct three-dimensional solutions (3,4) are known to date for the three-dimensional problem of cracks emanating from fastener holes. This work presents stress intensity factor solutions for three crack orientations at open and loaded fastener holes in a finite-thickness plate.

#### 1.2 Previous Work Leading to Stress Intensity Factors for Cracks Emanating from Open Fastener Holes

The first major advance in the study of cracks emanating from open holes in plates was due to Bowie (5) in 1956. He solved the two dimensional problem of single and double through-cracks at an open hole (Figures 1.1 and 1.2) using complex variable methods. Although not an

exact solution, Bowie's results have served as a basis in the framing of other studies. Perhaps more important is the almost universal use of his solution to establish the accuracy of other methods designed to provide answers for the more complicated problems being attempted today.

Tweed and Rooke (6) considered the single through-crack problem at a later date. They used a Mellin transform technique to predict stress intensity factor relationships. Their solution is claimed to have greater accuracy, especially for smaller crack lengths, than the Bowie solution.

Since the publication of Bowie's work, theoretical approaches to the more complicated three-dimensional problem of a surface flaw emanating from a fastener hole in a plate have been limited largely to estimates based upon extensions of related problem solutions. In general, these estimates suffer from an incomplete application of the many factors influencing the problem and from oversimplifications. Nevertheless, it is worthwhile to review some of these estimates to impress upon the reader the various directions taken in the study of this problem.

Kobayashi (7) estimated stress intensity factors for a semi-elliptical embedded crack adjacent to an open fastener hole in a very thick plate (Figure 2.1c). A linear approximation to the plane strain stress distribution near the hole was applied to a circular crack in an infinite solid without a hole. The stress intensity factor for an elliptical crack was formed through an estimated shape correction to the results for the circular crack. Surface effects and the through-thickness stress variation seen in the three-dimensional problem are neglected.

Hsu and Liu (8) estimated stress intensity factors for a corner crack at a hole in a plate (Figure 2.1a) by using as a basis the solution for an elliptical crack in an infinite solid. They applied a series of estimated correction factors to account for the presence of the hole and plate surfaces. Bowie's two-dimensional through-crack solution was assumed to provide a valid hole correction while an interpolation between three special crack shapes produced a front surface correction. No back surface correction was introduced.

Liu (9) considered a quarter-circular crack at a hole in a plate. He applied Smith's (10) solution to approximately account for the hole surface and front surface, Kobayashi's (11) solution as an approximate back surface correction, and Bowie's (5) two-dimensional solution to approximate the three-dimensional hole effect. The resulting stress intensity estimate was limited to a point on the crack periphery midway between the front and hole surfaces.

Perhaps one of the more complete estimates is that of Shah (12). He began by applying the plane strain stress distribution near a hole in a plate under uniaxial loading to a circular crack and used a Green's function to find stress intensity factors. He reasoned that these results also applied to two embedded semi-circular cracks emanating from a fastener hole. Estimated crack shape correction factors were applied to extend the estimate to elliptical shapes and Shah and Kobayashi's (13) results were applied as approximate back surface correction factors. A constant front surface correction, independent of location on the crack border, was assumed. A final factor was applied to relate single crack results to those for double cracks. Shah also used his

procedure to estimate stress intensity factors for cases of cracks emanating from a neat-filled loaded fastener hole.

Grandt (14) recently applied a linear superposition technique suggested by Rice (15) to the Bowie problem. He extended Bowie's results to cases of through-cracks adjacent to cold worked holes, open holes with varying remote loads, and interference-fit loaded fasteners. A necessary prerequisite for this method is a knowledge of stress intensity factors and crack opening displacements for one particular crack shape and orientation. The current lack of such information has limited extension of Grandt's results beyond the two-dimensional through-crack problem.

The very nature of the estimates of Kobayashi (7), Hsu and Liu (8), Liu (9), Shah (12) and others has caused many investigators to intensify their efforts in seeking results through experimental means.

Hall and Finger (16) completed a series of static fracture tests on specimens fashioned from 2219-T87 aluminum and 5A1-2.5 Sn (ELI) titanium alloys. They suggested two empirical failure criteria for one location on the crack front and restricted to the crack geometries tested.

Hall, Shah, and Engstrom (17) performed similar experiments in 4340 steel plates along with a wide range of fatigue and spectrum loading tests.

Static fracture tests of engineering metals, while useful when specific data on a particular material is needed, are subject to difficulties when compared to theories based upon principles of linear elastic fracture mechanics. If specimen sizing is too small, gross plastic deformations can produce results which are quite different from

elastic predictions. Additionally, the point of initial failure on the crack border is difficult to locate in metals. This has led many investigators to the use of transparent, brittle polymers such as polycarbonate, epoxy, and polymethylmethacrylate (PMMA) as better materials for modeling the fracture process.

Jolles, McGowan, and Smith (18) experimentally studied the single crack adjacent to an open fastener hole using established stress freezing photoelasticity techniques. They extended their earlier work (19) to more crack shapes and added the calculation of stress intensity factors at two intermediate locations on the crack front to those at the hole and surface intersections.

Snow (20) followed the lead of Grant and Hinnerichs (21) with a series of fatigue experiments in PMMA. Single cracks adjacent to open fastener holes were introduced and fatigued while crack growth data was recorded photographically. Suitable baseline tests produced additional information allowing for solution of the Paris fatigue relationship for stress intensity factors. Results are published only for the intersections of the crack front with the hole and with the front surface.

While the techniques of experimental fracture mechanics are surely becoming more sophisticated and capable of producing some credible results, theoretical solutions to the three-dimensional problem are still few in number.

Browning (3) formed a solution based upon the Schwartz-Neumann alternating method to obtain results for a single, embedded, semi-circular crack emanating from an open fastener hole in a finite thickness plate (Figure 2.1c). Two solutions were used in the alternating procedure:

1. Stress in a finite body due to surface tractions using a three-dimensional finite element method (Figure 1.3).
2. Stress in an infinite body due to arbitrary normal loading applied to an embedded circular crack.

Iteration between these two solutions removes tractions on the finite body free surfaces and the crack surface. The accumulated residuals from freeing of the crack surface are used to compute stress intensity factors from the circular crack solution. Browning's results showed trends similar to the estimates of Kobayashi (7). Unfortunately, his solution took a large amount of computer time and suffered some difficulties in the interpolation of stresses from finite element nodal points to Gaussian quadrature points. This necessitated a specific finite element mesh arrangement for each crack shape considered. Nevertheless, Browning's pioneering work provided the basis for further studies.

Ganong (4) extended the work of Browning by replacing solution 2 indicated above with the solution of Shah and Kobayashi (22) for stresses in an infinite medium due to arbitrary normal loading on an embedded elliptical crack (Figure 1.4). He also decreased the computational time required by using Cholesky decomposition of the finite element stiffness matrix and direct calculation of stresses at the Gaussian quadrature points on the finite element models. Ganong presented results for a number of single quarter-elliptical cracks emanating from open fastener holes. The versatility of the finite element-alternating method has several facets:

1. Once the finite element stiffness matrix is decomposed, stress intensity factor results for a wide variety of crack shapes

can be found at the expense of only 250 seconds of CDC 6400 central processor time per crack problem.

2. The finite element portion of the alternating method controls the geometry of the finite body containing the crack and is capable of modeling the complex geometries of actual machine parts.
3. The procedure gives stress intensity factors directly and does not rely on extrapolating stresses or fitting crack opening displacements as do some of the direct finite element schemes.

### 1.3 Previous Work on Stress Fields in Plates with Loaded Fastener Holes

The first step of the finite element-alternating method applies a known pressure distribution to the crack plane. In the case of an open hole, the three-dimensional analytic solution of Sternberg and Sadowsky (23) is used. Stress intensity factor results for certain cases of load transfer to a filled fastener hole can be found in the same manner if the crack plane stress distribution is known. The necessity for knowledge of crack plane stress distributions is not unique to the finite element-alternating method. Most of the estimates discussed earlier have the same requirement. While both two-dimensional and three-dimensional stress distributions are available for the open hole case, the complexity of the loaded fastener hole problem has limited available results to two-dimensions and less generality. Figure 1.5 shows the pin-loaded hole case considered in this work where the ratio  $Q/P$  ranges from 0.0 for an open hole to 1.0 for 100% load transfer to the fastener.

Perhaps the earliest attempt to define the stress distribution near a pin-loaded hole in a plate was a series of photoelastic studies by Coker (24) during the years 1913 to 1919. He was the first to notice very large tensile stresses on the plane of minimum cross-section in a plate of limited width.

Bickley (25), at the urging of Coker, used a classical elasticity approach in two dimensions to analytically find stresses around a circular hole in an infinite elastic solid due to surface tractions on the hole boundary. Results for several realistic hole surface tractions were calculated.

In 1935, Knight (26) made a significant contribution with a theoretical solution which, even today, has not been greatly improved upon. He recognized that hole surface tractions were important and assumed their form from a study by Howland and Stevenson (27). Using general elasticity theory, Knight then accounted for a finite plate width of twice the hole diameter. Theocaris (28) extended Knight's work to three additional hole diameter to plate width ratios in 1956.

Twelve years later, Gregory (29) solved the same problem (Figure 1.5) with the theory of infinite systems of linear equations. For tractions on the hole boundary, he assumed that

$$\sigma_{rr} = \begin{cases} -3/4 \left(\frac{Th}{a}\right) (1-\cos 2\beta) & \text{for } 0 \leq \beta \leq \pi \\ 0 & \text{for } -\pi < \beta < 0 \end{cases} \quad (1.3.1)$$

and

$$\sigma_{r\theta} = 0 \quad \text{for all } \beta \quad (1.3.2)$$

where  $a$  is the hole radius,  $h$  the plate half-width,  $T$  the remote

uniaxial tensile stress, and  $\beta$  the angle measured from the hole edge at the minimum cross-section. This boundary condition simulates a smooth, rigid, neat-fit pin. Gregory presented only stress concentration factor results at  $\beta=0$  for a large range of hole diameter to plate width ratios,  $a/h$ . These results compared well with experiments, particularly at the lower ratios of  $a/h$ .

The work of Bickley (25), Knight (26), Theocaris (28), and Gregory (29) represent the extent of present analytic solutions for the pin-loaded hole problem. Many important effects remain unaccounted for in their work and the increased problem complexities cause more recent investigations to be directed toward experimentation and approximation with finite element methods.

Frocht and Hill (30) used photoelasticity with bakelite specimens and strain gage mountings on aluminum plates to experimentally determine stress concentration factors for plates with pin-loaded holes. In addition to a wide range of plate geometries, they tested effects of differing pin clearances and lubrications.

Jessop, Snell, and Hollister (31) also applied photoelastic techniques to the problem, considering the interaction of various pin load levels with three different pin clearances. Again, results were limited to the pin-loaded hole boundary.

Cox and Brown (32) reviewed and coordinated available experimental data in 1963 in an attempt to sort out and explain the many results. In addition, they clarified the theoretical background as it applied to the various findings.

These studies, while enlightening, consider only one or two special effects of pin-plate interaction and generally present rather limited

results. The increasing flexibility of the finite element method lends itself to studies of the many effects acting simultaneously.

Harris, Ojalvo, and Hooson (33) solved a wide variety of pin-load problems using finite element methods. They considered both linear and non-linear stress and deformation of mechanically fastened joints and included effects of pin clearance and interference, load levels, plate and pin geometry, residual stresses, and fastener bending.

Mohaghegh (34) prepared a report including 22 combinations of fastener and plate loading, again with finite element methods. Two-dimensional results are presented in the form of stresses around the periphery of a fastener hole containing a rigid, smooth pin.

Brombolich (35) considered the effects of plasticity, load sequence, and fastener interference and contact. His results again were obtained using finite element methods and are restricted to unloaded fasteners in plates under remote uniaxial tension.

Due to the many effects present in the case of a pin-loaded hole in a plate, choice of a suitable crack plane stress distribution for adaptation to a stress intensity factor solution is not as straightforward as it might at first seem. In all likelihood, an appropriate distribution for a specific case understandably will not be found in the literature and it becomes necessary to generate needed results independently.

#### 1.4 Objectives

The objectives of this work were to:

1. Extend Ganong's (4) analysis to more crack shapes and to two additional classes of crack location relative to the hole.

2. Apply the finite element-alternating method to cases of cracks emanating from pin-loaded fastener holes.
3. Design and perform a series of static fracture tests to verify the theoretical results.
4. Calculate mode-one crack opening displacements for cracks emanating from fastener holes.
5. Assess accuracy by comparing the theory with experiments of other investigators.

In the process of fulfilling these objectives, the finite element-alternating method will be shown to accurately and efficiently calculate stress intensity factors for a variety of cracks emanating from both open and loaded fastener holes in finite-thickness plates.

## CHAPTER 2

### THEORETICAL APPROACH

#### 2.1 General Problem Statement

Consider part-elliptical cracks emanating from a hole in a finite thickness plate (Figure 2.1). The crack center is located at the hole edge and the crack lies in a plane perpendicular to the axis of loading. The finite plate geometry and loading conditions are such that the plane of the crack is a plane of symmetry for open hole problems. Mode-one stress intensity factors are to be calculated around the crack border for cases of remote uniaxial loading on a plate with an open fastener hole, and partial and total transfer of load to a filled fastener hole (Figure 1.5).

#### 2.2 General Solution Method

The finite element-alternating method used in this work separates the problem into two problems with stress intensity factor results obtained through an iterative procedure. Figure 2.2 schematically presents two iterations of the procedure where the fastener hole has been omitted in the interest of clarity. The top row of figures represents Solution 1 while the bottom row shows Solution 2. In the description to follow, letters in parentheses refer to steps in the iteration process as shown on the figure.

The first solution, hereafter referred to as Solution 1, is that of stresses in an unflawed finite body due to the applied remote loading. Solution 1 produces a normal stress distribution,  $p_0$ , on the plane where the crack is to be located due to remote loads (Step a). The second solution, hereafter referred to as Solution 2, is that of

stresses in an infinite body due to a pressure,  $-p_0$ , applied to the surface of an embedded elliptical crack. The solution to this problem results in stresses at locations in the infinite body corresponding to points on the surface of the finite body and frees the crack of residual stress (Step b). The stresses calculated by Solution 2 at surface locations on the finite body are reversed to free its surfaces and Solution 1 again produces a normal pressure distribution at the location of the crack in the unflawed finite body (Step c). Iteration between the two solutions is continued until stresses on the finite body surfaces predicted by Solution 2 and stresses at the crack location from Solution 1 are small. The superposition of results from all iterations then gives a close approximation to the desired solution for remote uniaxial loading on a finite body with a crack where the crack surface is stress free and the finite body surfaces have the prescribed stress boundary conditions. The total of normal stresses applied to the crack from all iterations to free its surfaces produces mode-one stress intensity factors,  $K_I$ , which are computed directly from Solution 2.

It should be mentioned that in actual practice, Solution 1 is not used to define the initial distribution of pressure on the crack plane for remote uniaxial loading (Step a). Rather, the three-dimensional analytic solution of Sternberg and Sadowsky (23) for the same loading case provides the necessary stress distribution.

### 2.3 Previous Work

The finite element-alternating method has its basis in the Schwartz-Newman method as reported by Kantorovich and Krylov (36). Similar

alternating methods have been widely used in the solution of stress intensity factor problems (13, 37, 38, 39).

Prior to Browning (3), the modeling of Solution 1 (Figure 1.3) was formed by overlapping semi-infinite solids which greatly complicated the alternating routine and restricted the finite body to a flat plate. Brownings' introduction of a three-dimensional finite element method as Solution 1 not only simplified the algorithm but allowed modeling of more complex bodies such as plates with fastener holes. Wilson's (40) SSAP3 finite element program with 20 node isoparametric elements was extensively modified by Browning for this purpose.

The problem of an elliptical crack embedded in an infinite solid (Figure 1.4), which is used as Solution 2 in the finite element-alternating method, was first considered by Green and Sneddon (41). They solved for stresses when the crack was subjected to a uniform normal pressure. Shah and Kobayashi (22) extended the work of Green and Sneddon to the case of arbitrary normal pressure on the crack where this pressure is expressible as a ten term polynominal in  $x$  and  $y$ ;

$$p(x,y,o) = \sum_{m=0}^{3} \sum_{n=0}^{3} A_{mn} x^m y^n \quad (2.3.1)$$

where  $m + n \leq 3$ .

The ten term limitation is due to the extensive and tedious work required in the calculation of stresses. Smith and Sorenson (39) programmed this solution for three stresses and six terms in the pressure polynominal. Ganong (4) extended the solution to ten terms and all six stresses.

Ganong also performed some auxiliary studies to understand the character of the finite element-alternating method. First, he noted that Solution 1 predicted normal stresses only on a portion of the crack plane where the full elliptical crack and the finite body overlapped. Since Solution 2 requires definition of the distribution over the entire elliptical crack surface, the question of how to describe the pressure on the portion of the crack lying "outside" the finite body had to be answered. Ganong chose the edge crack problem as a test case. Five different valid pressure distributions were applied to the "outside" section of the crack. Results for all cases agreed to within 1% but convergence was quite different. To study the accuracy of the polynomial fit to these crack pressures, he ran the same test cases for 19 iterations. Based on the best accuracy and most rapid convergence, a description of the crack pressure "outside" was chosen and labeled "linear decay." This produced a pressure distribution "outside" which linearly decays toward zero based upon the pressure along the crack-finite body boundaries and the crack dimensions.

Ganong also established the convergence and accuracy of the finite element portion of the solution. He applied uniaxial loading to meshes of 16, 45, 96 and 112 elements and compared tangential stresses on the plane  $z=0$  to those due to the analytic solution of Sternberg and Sadowsky. This study showed that finer divisions of the plate improved accuracy with the finest division, 112 elements, having a maximum average deviation of 2.5%.

#### 2.4 Accuracy and Sensitivity Test of the Method

A three-dimensional approximation to the two-dimensional through-crack problem (Figure 1.1) was made using two different finite element

mesh configurations in Solution 1 of the finite element-alternating method. The purpose of this comparison was to test both the accuracy of the method and sensitivity to the number of finite elements covered by the crack.

The first mesh configuration will be discussed later in this chapter and is designed to solve the problem of a single quarter-elliptical crack emanating from a fastener hole. It is pictured in Figure 2.4. The other mesh (Figure 4.1) is as described in Chapter 4 for use in the solution of the problem of an embedded crack adjacent to a fastener hole. This mesh is an exact division of the single crack mesh in the vicinity of the crack. The result is twice the number of elements through the plate thickness and across the plate width.

The through-crack was approximated by a very slender part-elliptical crack with a major to minor axis ratio of 2.5 or greater as shown in Figure 2.3. The crack center is located at the hole edge in the center of the plate.

In the finite element portion of the solution method presented in this chapter, the order of the shape functions determines the order of the displacement field modeled. The shape functions for the 20-node isoparametric element are quadratic in any one local coordinate direction. Application of the strain-displacement equation results in a linear description of strain. A constitutive law links stresses with strains and preserves the linear order. The concern here is that the finite element method approximates a non-linear stress field with a linear one over a crack which is confined to the boundaries of a small number of finite elements resulting in excessive stress intensity factor errors. These comments apply to the order of displacements,

strains and stresses prior to mapping into another coordinate system which may or may not preserve this order. However, in this work all mid-edge nodal points are located midway between the corner nodes which maintains linearity in stresses and strains during transformations.

A major portion of this possible difficulty is avoided as follows. Instead of initially solving for stresses at the crack location in the unflawed finite body using the finite element method (Step a, Figure 2.2) an analytic solution provides this information. Stress gradients over the crack from later iterations are more linear and thus the finite element approximation is better. Furthermore, these iterations contribute only about 25% of the final answer.

Results of the accuracy and sensitivity tests are listed in Table 2.1 and depicted in Figure 2.2. Comparisons are made with the through crack results of Tweed and Rooke (6) for  $L/R=1.5, 1.0, \text{ and } 0.5$ . In the finite element-alternating method, as  $L/R$  decreases the total number of elements covered by the crack decreases. It is convenient to view this as a reduction in layers of elements in the width direction but not through the thickness.

Inspection of Table 2.1 shows that deviations from the Tweed and Rooke results do not exceed 3.2%. The maximum difference occurs when the crack is positioned over only one layer of elements across the width indicating that one element coverage in the width direction gives sufficient accuracy.

The coverage of layers of elements through the plate thickness is always four for the more coarse single crack mesh and eight for the embedded crack mesh, regardless of  $L/R$ . The stress gradient through the thickness is more shallow than across the plate width. The finite

Table 2.1 Finite Element-Alternating Method Sensitivity  
to Number of Elements Covered by a Through-Crack

L/R	Single Crack Mesh (coarse)			Embedded Crack Mesh (fine)		
	Total Number of Elements Covered by Crack	Layers of Elements Covered Across Plate Width	% Difference From Tweed and Rooke ( 6 )	Total number of Elements Covered by Crack	Layers of Elements Covered Across Plate Width	% Difference From Tweed and Rooke ( 6 )
1.5	12	3	+1.02	48	6	+1.68
1.0	8	2	-1.31	32	4	-0.53
0.5	4	1	-3.2	16	2	-3.2

lement solution can produce a better approximation to this shallow gradient. If one element coverage in the width direction is sufficient, surely one element in the thickness direction is adequate for reasonable results. Therefore, very small cracks bounded by only one finite element can be used with the assurance that stress intensity factors may be only slightly less accurate than those for larger cracks.

Results for several small cracks can be found in this work. The next section shows a comparison with a fatigue experiment by another author. One crack considered has  $a/c=1.4$  and  $a/t=0.3$ . Appendix C presents results for a "benchmark" problem with  $a/c=2.0$  and  $a/t=0.2$ . Both of these cracks lie essentially within the boundaries of one finite element and results are reasonable with no signs of ill behavior in the solution.

## 2.5 Theoretical Solution Results for Single Quarter-Elliptical Cracks

### Emanating from an Open Fastener Hole

Figure 2.1a shows a single quarter-elliptical corner crack emanating from an open fastener hole in a finite thickness plate. The crack center lies at the intersection of the hole and front surface. The plate is subjected to uniaxial tensile loading in a direction perpendicular to the crack plane.

The finite element mesh to model Solution 1 of the finite element-alternating method for this crack configuration is shown in Figure 2.4 for a hole diameter to plate thickness ratio,  $d/t$ , of 1.0 and in Figure 2.5 for  $d/t=0.5$ . The mesh is semicircular with 112 elements and  $z=0$  is a plane of symmetry. There are four layers of elements through the thickness and seven divisions across the plate half-width. Planes

inclined at 10°, 20°, and 90° from the z=0 plane further divide the plate. Finer element divisions exist on the side of the hole where the crack is to be located to provide improved definition of stress gradients there.

Ganong (4) used the finite element-alternating method to find mode-one stress intensity factors for a series of single quarter-elliptical cracks emanating from an open fastener hole. In the interest of completeness, his results are presented in Figures 2.6 through 2.9. Several new results for cases not considered by Ganong has been added and will be discussed later in this chapter.

The calculations performed for numerous single quarter-elliptical corner cracks emanating from an open fastener hole are listed in Appendix A. Figures 2.6 through 2.11 are plots of magnification factor versus parametric angle from the front surface where the magnification factor is defined as

$$MF = \frac{K_I}{\sigma \sqrt{\pi a}} . \quad (2.5.1)$$

$K_I$  is the mode-one stress intensity factor,  $a$  is the crack dimension along the hole edge, and  $\sigma$  is the remote uniaxial tensile stress. The parametric angle,  $\theta$ , is defined by the parametric equations for an ellipse

$$\begin{aligned} x &= A \sin \theta & x &= A \cos \theta \\ && \text{or} & \\ y &= B \cos \theta & y &= B \sin \theta \end{aligned} \quad (2.5.2)$$

where  $A$  and  $B$  are the semi-major and semi-minor axes of the ellipse,

and  $x$  and  $y$  are coordinates of a point on the periphery of the ellipse. All finite element-alternating method calculations in this work are for a plate having a modulus of elasticity of  $30 \times 10^6$  psi and a Poisson's ratio of 0.25.

Ganong showed results for crack shapes of  $a/c=0.99$  and  $1.01$  which are omitted here for reasons to follow. These crack shapes were used to approximate a circular crack with a near-circular elliptical crack for comparison with results of other authors. Due to the limiting forms of stresses in the solution of the elliptical crack problem (Solution 2), exact circles cannot be duplicated. Ganong reasoned that since results for  $a/c=0.99$  and  $a/c=1.01$  were very close, both were accurate. Unfortunately, further study shows that both cases are subject to excessive errors. The difficulties lie in the formation of the matrix which yields stress function coefficients in Solution 2 of the finite element-alternating method. Inspection of the equations describing terms in this matrix shows definite tendencies for large round-off errors in the numerical calculations when the major and minor axes of the elliptical crack are nearly equal. Shah and Kobayashi (22) alluded to this round-off error problem when the circular crack shape was approximated too closely by a near-circular elliptical crack. As a result, they simulated a penny-shaped crack with an elliptical crack of shape  $a/c=0.982$ . In the finite element-alternating method, the improper formation of the matrix results in incorrect values of the stress function coefficients. This, in turn, causes the calculation of incorrect stresses on the surface of the finite body by Solution 2. When these stresses are reversed to free the surfaces and applied to the finite body to find the new crack plane stress distribution, the

body has a tendency to attempt a large rigid body translation. Because one nodal point is always fixed in x and y, (0, 0, 6) in this case, the body cannot translate but bends instead. The result is large errors in the description of the crack plane stresses and incorrect stress intensity factors. As an example of the magnitude of these errors, if Ganong's results for a single quarter-elliptical crack of  $a/c=1.01$  and  $a/t=0.5$  are added to the parametric plot in Figure 6.24, a 30% error in the value of the stress intensity factor at the front surface is seen. Calculations have been successfully carried out for crack shapes of  $a/c=0.90$  and  $1.10$ . No calculations have been completed in the range  $0.90 < a/c < 0.99$ , yet it is thought that due to Shah and Kobayashi's observation, the shapes to avoid are probably  $0.98 < a/c < 1.02$ .

Ganong (4) identified six effects which control the variation of magnification factor around the crack periphery. He interpreted the results in Figures 2.6 to 2.9 in terms of these six effects. Except for some general observations, his detailed comments will not be repeated. However, the six effects will be described here because they will be useful later.

1. Hole Stress Concentration Effect. Stress intensity factors are sensitive to the local stress field in the vicinity of the crack. Cracks having large  $c/r$  (Figure 2.1a), where  $r$  is the hole radius, extend into regions of lower stresses away from the hole and would be expected to have lower stress intensity factors. The reverse is true when low  $c/r$  places the entire crack in an area of elevated stress and stress intensity factors rise.

2. Front Surface Effect. Cracks intersecting a free surface can open more than cracks embedded in a solid under identical loading. Increased crack opening is reflected in higher stress intensity factors.
3. Back Surface Effect. As the ratio  $a/t$  increases and the crack approaches the back surface, stress intensity factors increase. This is due to the decreased rigidity of the ligament between the crack and back surface.
4. Hole Surface Effect. For small cracks, the hole surface acts like a free surface. This allows the crack to open and consequently increases stress intensity factors. For larger cracks, the hole acts to restrict crack opening and stress intensity is lowered.
5. Crack Shape Effect. The largest stress intensity factor for an elliptical crack under uniform loading occurs at the ends of the minor axis. The crack shape effect decreases as an elliptical crack approaches a circular shape.
6. Through-Thickness Stress Variation Effect. For a hole diameter to plate thickness ratio of 1.0, the stress concentration at the hole edge varies from 2.7 at the plate surfaces to 3.1 at the center of the plate. A similar variation occurs through the thickness at locations removed from the hole and results in like trends in stress intensity factors.

In the present study, it is not possible to separate the six effects and show their importance independent of one another. To do so would require corresponding results for a problem in which one of the effects was not important. Attempts to accomplish this usually

result in two or more effects changing simultaneously rather than just one. Only the shape effect can be so isolated at present as suggested by Kobayashi (42). He normalizes the magnification factor (Equation 2.5.1) by multiplying by  $N$ , where

$$N = A^2 / (A^2 \cos^2 \theta + B^2 \sin^2 \theta)^{1/4}, \quad (2.5.3)$$

$A$  and  $B$  are the semi-major and semi-minor axes of the elliptical crack and  $\theta$  is the parametric angle from the minor axis.

Figures 2.6 through 2.9 are plots at constant  $a/t$  for varying crack shapes,  $a/c$ . At the front surface intersection, magnification factors change no more than about 8% over a wide range of crack shapes due to a balance maintained between a number of effects. Increasing  $a/c$  means decreased  $c/r$  which raises stress intensity factors due to the hole surface effect. Decreasing  $c/r$  also places the crack border near the front surface in a region of higher stresses which leads to higher stress intensities. For cracks with  $a/c < 3.0$ , the increase in magnification factor as the front surface is approached is due to a combination of front surface and crack shape effects.

Ganong (4) remarked that magnification factors were always highest at the hole intersection due to the dominant character of the hole stress concentration effect. While this may be true for single quarter-elliptical cracks of  $a/c \leq 2.0$  as considered by Ganong, it is not the case for  $a/c > 2.0$ . Figures 2.6 and 2.8 show magnification factors for  $a/c = 3.0$  and  $a/t$  of 0.9 and 0.5. In both cases, the location of maximum stress intensity is shifted to an intermediate point along the crack periphery and nearer the front surface. This is again due to a combination of several effects. As  $a/c$  increases to 3.0,  $c/r$  decreases and

locations on the crack border near the front surface lie in an area of higher stresses. Also, the crack shape effect causes stress intensity factors to decrease at the hole intersection.

The variation in magnification factor along the crack periphery for cracks with  $a/c < 1.0$  is wider than for  $a/c > 1.0$  as can be seen in Figures 2.8, 2.9 and 2.10. Since the crack minor axis is along the front surface for  $a/c < 1.0$ , the crack shape effect does not reduce the elevated stress intensity at the hole intersection as happens with higher  $a/c$  values. The shape effect, hole surface effect and hole stress concentration effect combine to lower stress intensity factors at the front surface for cracks which are long in that direction. Figures 2.9 and 2.10 show this to be strong enough to overcome the effect of the front surface.

Figure 2.11 shows magnification factor versus parametric angle for the same crack with hole diameter to plate thickness ratios of 1.0 and 0.5. This reduction was accomplished by halving the hole diameter while leaving all other plate and crack dimensions unchanged. Thus, the only effects on the magnification factor should be those of the hole surface and the hole stress concentration. As expected, the hole stress concentration effect dominates, resulting in a lowering of magnification factor everywhere as the increased  $c/r$ , due solely to reduced hole radius, places the crack in a region of lower stresses. The effect of the hole surface can be seen in the wider separation of the two curves at the hole intersection. The reduction in  $c/r$  increases the rigidity of the hole with respect to the unchanged crack size. This increased rigidity is reflected in reduced crack opening and lowered stress intensity factors for  $d/t = 0.5$ .

It is perhaps important to recognize that stress intensity factors presented in this work at the hole and surface intersections may be somewhat in error. Hartranft and Sih (43) studied the semi-circular surface flaw in a semi-infinite solid in great detail and discovered that stress intensity factors on the crack periphery near the surface dropped sharply toward zero. Sih (44) explains this result with the observation that the state of stress is very complex near a surface. At all other locations, Hartranft and Sih's results compare closely with those of Smith (45). This decrease in stress intensity factor near the surface intersections was not seen in the present work, due probably to the nature of the approximations used. However, experiments conducted by the author show cracks to propagate at points of highest stress intensity factor, not lowest. A small shift in this location, while theoretically important, has little practical significance.

## 2.6 Comparison of Theoretical Results with Two Independent Experiments

Snow (20) reports a series of seven tests resulting in predicted stress intensity factors for some single quarter-elliptical cracks at open fastener holes (Figure 2.1a). In his work, a starter crack was introduced at the intersection of a hole and a surface in a plate of polymethylmethacrylate (PMMA). The plate was cycled under low load levels and the crack grew by fatigue. At periodic intervals, 35 mm photographs were taken perpendicular to the crack plane. Measurements from the photographs gave crack length versus number of cycles data.

The Paris fatigue relationship,

$$\frac{da}{dn} = C(\Delta K)^m \quad (2.6.1)$$

was assumed to apply where C and m are material dependent constants,

$\Delta K$  is the change in stress intensity factor during cycling, and  $da/dn$  is the crack growth rate.  $C$  and  $m$  were determined from a single through-crack baseline test (Figure 1.1) where  $da/dn$  was measured and  $\Delta K$  was known. Crack length versus cycles data from the fastener hole tests required careful differentiation to yield crack growth rates. Knowledge of  $da/dn$ ,  $C$ , and  $m$  permits solution of the Paris relationship for stress intensities.

The most complete results shown by Snow are for an average  $a/c$  of 1.4 and a range of  $a/t$  from 0.23 to 0.84. Magnification factors are presented at the hole and surface intersections only. The average hole diameter to plate thickness ratio,  $d/t$ , for the seven tests was 1.05. This close agreement in plate geometries between Snow's experiment and the finite element-alternating method model permits a valid comparison of results from the two studies.

To form this comparison, stress intensity factors were calculated by the finite element-alternating method for single quarter-elliptical cracks emanating from an open fastener hole where  $a/c=1.4$ ,  $d/t=1.0$ , and  $a/t$  ranged from 0.3 to 0.8. Figures 2.12 and 2.13 are plots of magnification factor versus  $a/t$  for the experiments of Snow and the theoretical results of the finite element-alternating method. Agreement at the hole intersection is within 2%. Agreement at the front surface intersection is not as close but trends with increasing  $a/t$  are identical. Here, the finite element-alternating method predicts magnification factors which average 13% below Snow's results.

Figures 2.14 and 2.15 show a similar comparison for an average  $a/c$  of 1.5. Agreement between Snow's results and those of the finite element-alternating method is within 3% at both the hole and surface

intersections for  $a/t=0.5$  and trends with increasing  $a/t$  are in close accord.

The Poisson's ratio of PMMA is 0.35 while all finite element-alternating method calculations are for a value of 0.25. Smith (46) noted a 3% increase in back surface magnification factors when Poisson's ratio was increased from 0.25 to 0.39 in his theoretical study of semi-elliptical surface cracks. If all theoretical results shown in Figures 2.12 through 2.15 are increased by this amount, the maximum disagreement is reduced to 10%.

McGowan and Smith (19) used stress-freezing photoelasticity to experimentally determine stress intensity factors. Their results were limited to the points of intersection of the crack with the hole and front surface. Table 2.2 shows a comparison of magnification factors from McGowan and Smith's experiments with results from the finite element-alternating method. Only three of the eight tests have plate and crack geometries close to those of existing finite element-alternating method results. The striking feature of most of the experimental tests is a higher magnification factor at the front surface than at the hole. McGowan and Smith claim this is due to load transfer to the side of the hole opposite the crack which tends to lower the magnification factor at the hole intersection. Test 4 shows this lowered value for a crack with  $a/c=1.10$  and  $a/t=0.48$ . Figure 6.25 is a parametric plot of stress intensity factor versus various values of  $a/c$  and  $a/t$  from finite element-alternating method calculations to explain slow growth in the experiments discussed in Chapter 6. This plot shows that the change in location of maximum magnification factor for cracks with  $a/t=0.5$  should not occur until

Table 2.2 Comparison with Stress-Freezing  
Photoelasticity Experiments

McGowan and Smith (19)	a/t	a/c	d/t	$K_I$	
				Surface	$\frac{\sigma}{\sqrt{\pi a}}$
Test 4	0.48	1.10	0.88	0.90	0.89
Test 6	0.46	1.55	0.94	0.98	0.94
Test 7	0.74	1.98	0.95	1.08	0.66
Finite Element- Alternating Method (equivalent to)					
Test 4	0.50	1.10	1.00	1.03	1.36
Test 6	0.50	1.50	1.00	1.04	1.24
Test 7	0.75	2.00	1.00	0.94	1.06

$a/c$  is larger than 2.0. This suggests that McGowan and Smith may be observing a valid trend but that onset of the shift in location of maximum magnification factor is being seen at crack shapes that are much too small.

Static fracture tests of plates having cracks of various shapes and locations relative to fastener holes were performed by the author. Comparison of the present theory with a large number of these experiments is presented in Chapter 6.

## CHAPTER 3

### DOUBLE SURFACE CRACKS EMANATING FROM AN OPEN FASTENER HOLE

#### 3.1 Problem Statement

Figure 2.1b shows double quarter-elliptical surface cracks emanating from an open fastener hole in a finite-thickness plate. The crack centers lie at the intersection of the hole and the front surface. The plate is subject to uniaxial tensile loading in a direction perpendicular to the plane containing both cracks. Regardless of the orientation of the crack major and minor axes, "a" refers to that crack dimension along the edge of the hole while "c" is along the front surface of the plate. Both cracks are of the same shape and depth. This double crack configuration is seen in fatigue failures when, following initiation of a single crack, a second crack propagates on the side of the hole opposite the first. Mode one stress intensity factors are to be calculated around the peripheries of both cracks.

#### 3.2 Finite Element Mesh Configuration

The finite element mesh used in the solution of the double crack problem is quarter-circular with 108 elements (Figure 3.1). This mesh is arranged similar to those for the single and embedded crack configurations. There are four layers of elements through the thickness and nine divisions across the plate half-width. Planes inclined at 10° and 20° from the plane  $z=0$  further divide the plate. Finer element divisions exist near the hole to provide improved definition of the stress gradients there. The planes  $z=0$  and  $y=0$  are assumed planes of symmetry and are rollered to prevent displacements in the  $z$  and  $y$  directions,

respectively. The mesh is pictured in Figure 3.1 for a hole diameter to plate thickness ratio,  $d/t$ , of 1.0 and in Figure 3.2 for  $d/t=0.5$ .

### 3.3 Changes to the Finite Element-Alternating Method for the Double Crack Problem

The finite element-alternating method as applied to the problem of single quarter-elliptical cracks emanating from a fastener hole uses as one solution that of a single elliptical crack in an infinite medium subjected to an arbitrary pressure distribution. No solution is currently available for the companion problem of two cracks. The difficulties caused by use of the single crack solution coupled with the finite element mesh of Figures 3.1 or 3.2 for the double crack problem stem from a mismatch in planes of symmetry. While symmetry about the  $y=0$  plane is forced upon the finite element solution, the crack solution has no such symmetry about this plane. The only symmetries recognized by the crack solution are those about planes passing through the crack center, none of which coincide with the plane  $y=0$  because the crack center is offset from the hole center. Therefore, changes to the finite element-alternating method were necessary to allow for the presence of the second crack and to produce a match in the symmetries.

The following changes were made to the solution method for the double crack problem and represent one iteration. The crack referred to as the "right" crack has its center at the intersection of the fastener hole and front surface on the side of the plate actually modeled by the finite element mesh. The "left" crack is a mirror image of the "right" crack about the  $y=0$  plane. Between Steps a and b, Figure 2.2, Solution 2 of the finite element-alternating method calculates residual

stresses at the location of the left crack due to the freeing of residual stress on the right crack. These residuals are combined and applied to the right crack (Step b, Figure 2.2). Solution 2 then solves for stresses at locations on the finite body and mirror image locations on a fictitious quarter plate mirrored about the  $y=0$  plane (Figure 3.1). Combined stresses from actual and mirror locations are residuals to be removed from the finite body surfaces (Step c, Figure 2.2).

Some care must be exercised in the use of this double crack algorithm. If the major or minor axis of one crack touches the center of the second crack, the elliptical crack solution is asked to calculate singular stresses on the crack boundary. The obvious correction is to avoid crack dimensions which create this problem. At first glance, the overlapping of the two cracks also raises questions of solution validity. Crack overlap causes the elliptical crack solution to calculate stresses on the plane  $z=0$  inside the crack which in itself causes no problems. Results presented in this thesis are for cracks which overlap only in regions outside the boundaries of the finite body. Since the stresses in these regions are linearly decayed prior to the polynomial fitting procedure which describes the crack plane stress distribution, any possible problems due to crack overlap are eliminated.

### 3.4 Three Dimensional Analysis of a Two-Dimensional Test Problem

Bowie (5) solved the two-dimensional problem of double through-cracks emanating from a hole in a plate subjected to uniaxial loading (Figure 1.2). His well respected solution employed complex variable techniques to calculate stress intensity factors. To form a comparison using the present method, double through-cracks were approximated by

two very slender part-elliptical cracks with major to minor axis ratios of 2.5 or greater. This configuration is pictured in Figure 3.3 along with results from the finite element-alternating method and Bowie's solution. Calculations were performed for L/R of 1.5, 1.0, and 0.5. Results at the center of the plate are presented to minimize the effects of the surfaces and thus more closely model a plane strain situation. The three-dimensional finite element-alternating method analysis of this two-dimensional problem shows agreement to within 5% of the Bowie results.

### 3.5 Solution Results

A list of calculations performed for various double cracks emanating from open holes is shown in Appendix A. Comparative plots of magnification factor versus parametric angle from the front surface are presented in Figures 3.4 through 3.9. The magnification factor is defined as before,

$$MF = \frac{K_I}{\sigma\sqrt{\pi a}} . \quad (3.5.1)$$

Crack shapes and depths used in the double crack calculations were identical to those used by Ganong (4) for single cracks. This was done with forethought so that effects of the addition of a second crack could be analyzed. The results for the corresponding single cracks are shown and discussed in Chapter 2 and form a basis for comparison of double crack results. Both this author and Ganong analyzed the single crack results with respect to the six effects mentioned in Chapter 2. These comments apply equally well to the double crack results with the possible exception of the hole surface effect.

For small single cracks, the hole surface acts like a free surface which tends to elevate stress intensity factors. Bowie (5) noted for through-cracks that when the crack length to hole radius ratio is small, stress intensity factors for one and two cracks are approximately the same. As cracks get larger, however, the effect of the hole is quite different for single and double cracks. For larger single cracks, hole rigidity restricts crack opening which lowers stress intensity factors. The addition of a second large crack has the opposite effect since it reduces hole rigidity and allows both cracks to open more. This produces elevated stress intensity factors with respect to the single crack case. All double crack calculations presented here exhibit this trend.

Casual inspection of plots of magnification factor versus parametric angle (Figures 3.4 through 3.9) shows little difference from the single crack results (Figures 2.6 through 2.10). While differences do appear subtle, they can be as large as 8%. In all cases, the maximum elevation in stress intensity factors with respect to the single crack occurred not at crack intersections with surfaces but rather at parametric angles of from 30 to 50 degrees. At these locations, stress intensity factors for double cracks were 4-8% higher than for the corresponding single cracks. The amount of increase appears to be a function of the crack length along the front surface versus hole radius ratio,  $c/r$ , regardless of crack shape or depth. As  $c/r$  increases from 0.5 to 1.0, the difference in stress intensity factors for double versus single cracks increases uniformly from 4 to 8% at the 30 to 50 degree location. From  $c/r$  of 1.0 to 1.34 the difference remained at the high of 7 to 8%.

Increases in stress intensity factors at the hole and front surface intersections for double versus single cracks were lower than at the 30-50 degree location. The amount of change was a definite function of  $a/t$  as might be expected, since as  $a/t$  increases hole rigidity decreases. For  $a/t=0.5$ , double crack results show no increase at the hole intersection but a 3-5% increase at the front surface. As  $a/t$  becomes larger, stress intensity factors at the hole intersection begin to increase until they are 2-5% above single crack results while values at the front surface remain about 3-5% higher.

Figure 3.9 shows magnification factors for the same double crack shape and hole diameter to plate thickness ratios,  $d/t$ , of 1.0 and 0.5. As with the corresponding single crack problem discussed in Chapter 2, the only dimensional change in the reduction of  $d/t$  from 1.0 to 0.5 was the hole diameter. Both cracks extend like distances along the hole and front surfaces yet the ratio  $c/r$  is doubled for the  $d/t=0.5$  case. The depth ratio,  $a/t$ , remains the same. Earlier observations on double versus single crack results linked magnification factor differences at the hole and surface intersections to  $a/t$  and at intermediate points to  $c/r$ . The same trend in reverse seem to be occurring here for changing  $c/r$ . As this ratio increases, magnification factors decrease at intermediate points, but do not change appreciably near the hole and front surfaces. Again, this lends support to the dominant effect of the hole stress concentration which overshadows effects of the hole surface. Increasing  $c/r$  for double cracks would be expected to elevate stress intensity factors due to decreased hole rigidity yet the fact that the crack lies in a region of lowered stress is still more important.

### 3.6 Comparison with an Estimate of Another Author

Shah (12) used a Green's function technique to find stress intensity factors for two semi-elliptical embedded cracks emanating from a fastener hole. He applied correction factors for the surface effects and reasoned that for through-cracks (Figure 1.2)

$$(K_I)_{\substack{\text{one} \\ \text{crack}}} = \sqrt{\frac{2R+L}{2R+2L}} (K_I)_{\substack{\text{two} \\ \text{cracks}}}. \quad (3.6.1)$$

The corresponding elliptical crack relationship was assumed to be

$$(K_I)_{\substack{\text{one} \\ \text{crack}}} = \sqrt{\frac{2R+\frac{\pi ac}{4t}}{2R+\frac{2\pi ac}{4t}}} (K_I)_{\substack{\text{two} \\ \text{cracks}}} \quad (3.6.2)$$

where  $\frac{\pi ac}{4t}$  is the crack length of a through-crack having the same area as an elliptical crack of depth  $a$  and length  $c$ . Shah's estimates could be discussed at length in a comparison with solutions by the finite element-alternating method. This author chooses to deal solely with the one-to-two crack corrections predicted by both methods. Shah's factor actually corrects double crack results to find stress intensity factors for a single crack but comments below will treat this in reverse for comparison with the present study.

While Shah's one-to-two crack correction factor tends to overestimate the average differences found with the finite element-alternating method by only about 1 to 2%, his factor predicts a constant correction for all locations on the crack front. The present study indicates there can be as much as an 8% variation along the crack border. His factor is also necessarily limited to  $a/c \leq 1.0$ , not only because these are the shapes he considered but because crack orientation

is important. Consider two cracks with identical areas but one having the major axis along the front surface ( $a/c < 1.0$ ) and the other with the major axis along the hole ( $a/c > 1.0$ ). The finite element-alternating method predicts correction factors differing by as much as 5% for these two cases while Shah's correction factors would be identical. Figure 3.7 shows a comparison of Shah's estimate with present results for double cracks having  $a/c = 0.5$  and  $a/t = 0.25$ .

Static fracture tests of plates having cracks of various shapes and locations relative to fastener holes were performed by the author. Comparison of the theory with a large number of these experiments is presented in Chapter 6.

## CHAPTER 4

### EMBEDDED CRACKS EMANATING FROM AN OPEN FASTENER HOLE

#### 4.1 Problem Statement

Figure 2.1c shows a single half-elliptical crack emanating from an open fastener hole in a finite-thickness plate. The crack center is located at the edge of the hole, midway through the plate thickness. The crack major axis is always parallel to the hole centerline. The crack has no front or back surface intersections but some results are shown for cases where  $2c=t$ . This configuration will be referred to as an embedded crack. The finite width plate is subject to uniaxial tensile loading in a direction perpendicular to the crack plane. Stress intensity factors are to be calculated along the crack periphery. While many in-service failures have resulted from corner cracks at fastener holes, the embedded crack has recently gained attention due to failures in aircraft jet engine turbine rotors due to cracks of this type.

#### 4.2 Finite Element Mesh Configuration

The finite element mesh used in the solution of the embedded crack problem (Figure 4.1) is similar to that used by Ganong (4) for the single corner crack emanating from a fastener hole. Both meshes have 112 elements with the difference that the embedded crack mesh has symmetry about the  $x=0$  plane in addition to the  $z=0$  plane. Therefore, all 112 elements lie in the direction of the positive  $x$ -axis and are distributed over the plate half-thickness. This mesh arrangement is pictured in Figure 4.1 for a hole diameter to plate thickness ratio,  $d/t$ , of 1.0 and in Figure 4.2 for  $d/t=0.5$ .

### 4.3 Solution Results

A list of calculations performed for numerous embedded cracks emanating from an open fastener hole is shown in Appendix A. Comparative plots of magnification factor versus parametric angle from the crack minor axis are presented in Figures 4.3 through 4.7. The magnification factor is defined as

$$MF = \frac{K_I}{\sigma\sqrt{\pi a}} \quad (4.3.1)$$

or for ease of comparison in some of the plots,

$$MF = \frac{K_I}{\sigma} \quad (4.3.2)$$

where  $K_I$ ,  $\sigma$  and  $a$  are as defined earlier.

The six effects assumed to alter the stress intensity factor around the crack periphery for single and double corner cracks emanating from a fastener hole, in general, also apply to the embedded crack. These effects are listed in Chapter 2. Two important differences must be noted, however. The ends of the crack major axis approach the front and back surfaces of the plate equally. The effect here is the same as the back surface effect for corner cracks and will be referred to simply as the surface effect. Also, since the crack never intersects the plate surfaces in the results presented here, the front surface effect does not apply to the embedded crack configuration.

In all results shown, the effect of the hole stress concentration is of great importance and accounts for a large share of the variation in magnification factor along the crack front. Thus, portions of the crack nearest the hole would be expected to have elevated stress intensities while those removed from the hole would have smaller values.

The following discussion deals more with deviations from this behavior caused by other effects than with this effect directly.

Figures 4.3 and 4.4 show comparative plots for five crack shape and two crack depth ratios. Since the crack depth to hole radius ratio,  $a/r$ , is constant in each figure, the hole surface effect is deemed not a factor in comparisons between results on the same figure. Figure 4.3 shows the dominant character of the crack shape effect. The surface and hole stress concentration effects expected to occur at the hole intersections are overshadowed by the strong shape effect which tends to reduce stress intensity at the ends of the crack major axis. Additionally, the magnification factor changes only slightly at this location with rather large changes in crack shape. This is the result of a balance as  $a/c$  increases between:

1. Decreasing surface effect ( $K_I$  decreases)
2. Increasing shape effect ( $K_I$  increases)
3. Increasing through-thickness stress concentration  
( $K_I$  increases)

Figure 4.4 shows trends similar to those noted in Figure 4.3 except that shape effects are now smaller due to higher  $a/c$  values. Here the surface effect is more important as seen by the decrease in magnification factor at the hole intersection as the crack major axis moves away from the surfaces (increasing  $a/c$ ). Again, a balance between the same effects noted in the previous paragraph maintains identical magnification factor values at the hole intersection as  $a/c$  increases from 0.67 to 0.75.

Figures 4.5 and 4.6 show comparative plots for two  $a/c$  and four  $a/t$  ratios. Since the crack shape is constant in each figure, the crack

shape effect is not a factor when comparisons are between cases on the same figure. The choice of  $K_I/\sigma$  as a magnification factor more clearly shows the effect of crack proximity to the surfaces. As cracks become larger in both figures, magnification factors at  $\theta=0$  are increased no more than 15%. In Figure 4.5 for cracks with  $a/c=0.5$ ,  $a/t=0.125$  and 0.1875, the crack shape effect dominates resulting in a maximum stress intensity at about 50 degrees of parametric angle from the minor axis. However, when  $a/t$  reaches 0.25, the surface effect takes over, shifting the point of maximum stress intensity to the hole intersection. The results shown in Figure 4.6 are similar with respect to the strong surface effect but due to the larger  $a/c$  ratios, the shape effect is of lesser importance.

Figure 4.7 shows magnification factor versus parametric angle for the same crack with hole diameter to plate thickness ratios of 1.0 and 0.5. As with similar single and double corner crack results, the reduction in  $d/t$  involved only the hole diameter while all other plate and crack dimensions remained unchanged. The hole stress concentration effect again dominates the results by lowering magnification factors everywhere since the crack for the  $d/t=0.5$  case extends into regions of lower stress.

#### 4.4 Comparisons with Estimates and Solutions of Other Authors

Kobayashi (7) considered the problem of an embedded crack emanating from an open fastener hole in a very thick plate. He used a superposition method based upon removing residual crack surface tractions predicted by the stress distribution in an uncracked plate. The stress intensity factor for a through-crack is calculated using

$$K_I = \frac{1}{\sqrt{\pi a}} \left[ \int_{-a}^0 \sigma_{yy}^-(x,0) \sqrt{\frac{a+x}{a-x}} dx + \int_0^a \sigma_{yy}(x,0) \sqrt{\frac{a+x}{a-x}} dx \right] \quad (4.4.1)$$

where  $\sigma_{yy}(x,0)$  is the plane strain stress distribution in an uncracked plate with a hole,  $\sigma_{yy}^-(x,0)$  is the mirror image of  $\sigma_{yy}(x,0)$  and  $a$  is the crack length.  $\sigma_{yy}$  is approximated by the linear distribution

$$\sigma_{yy} = 3 - \frac{r}{r} \quad 4.4.2)$$

where  $r$  is the hole radius and  $n$  is the slope of the straight line distribution which minimizes differences from the true distribution. Correction is made to the through-crack stress intensity to produce corresponding values for semi-elliptical embedded cracks.

Figure 4.8 shows a comparison of magnification factor versus parametric angle from the hole intersection for an embedded crack with  $a/c=0.4$  as considered by Kobayashi and  $a/c=0.5$  from the finite element-alternating method. Since Kobayashi's estimate is for a very thick plate, no surface correction is made. Also, the plane strain stress distribution obviously does not account for through-thickness stress variations and Kobayashi admits that the hole surface effect could amount to a 5% change in his results.

The comparison in Figure 4.8 shows the magnification factor from the finite element-alternating method 10% higher than Kobayashi's result at the hole intersection. At least 5% of this is due to the surface effect unaccounted for in Kobayashi's result. Another 2% can be attributed to differences in describing the stress distribution over the crack. The remaining difference is accounted for by the shape and hole surface effects, both of which have the tendency to elevate stress

intensity factors at the hole intersection in the finite element-alternating method result.

At  $\theta=0$ , the finite element-alternating method result is 8% below that of Kobayashi. The major portion of this difference is from the representation of the stress field over the crack. Kobayashi's linear simplification overestimates the three dimensional Sternberg and Sadowsky (23) solution used in the present method by about 7%.

Figure 4.9 is a parametric plot of magnification factor at the hole intersection versus  $2c/t$  for a series of results from the finite element-alternating method solution for  $a/r=0.25$  and Kobayashi's estimate for  $a/r=0.20$ . The lack of agreement at low  $2c/t$  is due to the effects mentioned earlier. Of interest is the large difference, due essentially to the surface effect, as  $2c/t$  approaches 1.0 and the nearly constant magnification factor predicted by the finite element-alternating method as  $2c/t$  increases from 0.375 to 1.0.

Browning (3) applied the finite element-alternating method to find magnification factors for embedded circular cracks emanating from fastener holes in finite-thickness plates. While the current version of this method is not suited to solution of the circular crack problem as mentioned in Chapter 2, parametric plots show agreement with Browning's results. Figure 4.10 is a plot of magnification factor versus  $2c/t$  for  $a/r=0.5$ . As  $2c/t$  decreases, the current study predicts a reduction in magnification factor at the hole intersection due to reduced surface effects. As the crack approaches a circular shape, however, the surface effect becomes small and the shape effect dominates, increasing the magnification factor at this location. At  $\theta=0$ , the

reduction in magnification factor is seen throughout the range of  $2c/t$  as expected for cracks over which the average stress has decreased.

## CHAPTER 5

### CRACKS EMANATING FROM LOADED FASTENER HOLES

#### 5.1 Problem Statement

Previous chapters presented stress intensity factor results for three classes of crack location relative to an open hole in a finite-thickness plate. The plate was loaded in uniaxial tension perpendicular to the plane of the crack. In the problems to follow, the hole is filled with a pin or fastener to which all or a portion of the remote load is transferred (Figure 1.5b).

#### 5.2 Theoretical Approach

The finite element-alternating method as applied to the open fastener hole problem assumed symmetry about the plane  $z=0$ , thus only the upper portion of the full plate was modeled (Figure 2.4). Necessarily, the upper portion of the hole was treated as a free surface. If it can be shown that these two requirements can be approximately met for the loaded fastener hole case, the solution method need not be changed and the finite element stiffness matrices from the open hole cases can be used at a great savings in computer time. Crack plane stress distributions for the open hole case (Step a, Figure 2.2) can then be replaced by distributions for partial or total transfer of load to the filled fastener hole.

#### 5.3 Problem Modeling and Assumptions

To approximately meet the requirements of the preceding section and also to form a realistic problem the following assumptions are made:

1. Fastener Stiffness and Loading Conditions. The fastener is taken to be rigid and is loaded in double shear (Figure 1.5b). A rigid fastener cannot bend and double shear loading requires the pin to remain perpendicular to the plate surfaces. Thus, bearing stresses on the hole boundary are constant through the plate thickness. Resulting normal stresses on the plane perpendicular to the loading direction at the minimum section are also assumed constant through the thickness. These assumptions are thought to be realistic since in practice any through-thickness variations are small for double shear loading. Fastener rigidity is reflected in fastener to plate stiffness ratios. For steel fasteners in aluminum plates this ratio is 3 to 1 while for the same fastener in Plexiglas, it is 7 to 1. For the 7 to 1 ratio, Harris, Ojalvo, and Hooson (33) suggest a through-thickness correction of 6% to the bearing stress exerted on the hole by a rigid fastener in double shear. The resulting through-thickness variation in normal stresses on the crack plane due to pin bending surely is much smaller.
2. Hole Boundary Conditions. The fastener is assumed to be smooth and thus transmits only radial loads to the hole. Shear at the interface is assumed to have little effect on the crack plane normal stress field. Support for these assumptions can be found in the results of Frocht and Hill (30) who noted only a 4% decrease in hole stress concentration factors when loaded steel and aluminum fasteners in aluminum plates were lubricated. Additionally, shear on the interface does not affect the normal stress distribution at other locations on the crack plane to

any great degree. Finite element results of this chapter for loaded smooth pins are compared to the analytic solution of Theocaris (28) which included shear between the fastener and the hole (Figure 5.5). Differences in the stresses on the crack plane in the vicinity of the hole predicted by the present method and the Theocaris solution are small.

3. Fastener-to-Hole Contact. The fastener load is assumed to be transferred over the lower half of the hole,  $0 \leq \beta \leq \pi$  (Figure 1.5b). Harris, et al., (33) showed that this contact condition realistically simulates fastener clearances from a net fit (no clearance or interference) at low loads to a neat fit (0.4% clearance) at high load levels. Greater fastener clearance or interference shifts the location and magnitude of the maximum tensile stress yet Frocht and Hill (30) noted for neat fit fasteners that this maximum always occurred on the hole edge at the minimum section.
4. Stress Intensity Factor. Mode-one stress intensity factors are assumed to dominate over mode-two effects. Fastener loading produces non-zero shearing stresses along the line  $\beta=0$  (Figure 1.5b). For the same fastener loading considered here but for double through-cracks (Figure 1.2), Cartwright and Ratcliffe (47) reasoned that the mode-two stress intensity factor was no more than 1/10 the magnitude of the mode-one stress intensity factor for pin loading. Sih (44) studied the relative importance of mode-one and mode-two stress intensity factors for a through-crack oriented at different angles to the axis of remote tensile loading. For cracks nearly

perpendicular to the loading axis, the mode-two influence on the stress intensity factor is perhaps at the most 2% for the ratio suggested by Cartwright and Ratcliffe. Therefore, although mode-two effects are present, they are small and will be neglected in this work.

5. Displacement Symmetry. Displacements in the  $x$  direction along the line  $\beta=0$  are assumed to be zero (Figure 1.5b). This is obviously not precisely correct. The asymmetry in loading and asymptotic behavior of the normal stresses about the  $y$ -axis near the hole cause a displacement and rotation of this line. Results of the two-dimensional finite element study of this chapter show these displacements and rotations small enough in all load transfer cases to neglect.

#### 5.4 Calculation of Crack Plane Stress Distributions

The assumptions of the previous section are realistic and at the same time allow the finite element stiffness matrices formed and decomposed for the open hole cases to be used without change to find stress intensity factors for loaded hole problems. It is necessary, however, to describe the crack plane normal stress distribution due to the loaded fastener. This information will be substituted for the open hole distribution due to Sternberg and Sadowsky (23) which is shown as Step a in the finite element-alternating method diagram of Figure 2.2.

Crack plane normal stress distributions for the loaded fastener hole cases were generated using established two-dimensional finite element procedures for linear elasticity. This was necessary for the following reasons. Current literature contains distributions for

specialized cases, none of which match the hole boundary conditions, plate dimensions, and load transfer ratios of the problems considered here. In the loaded hole problem as plate width changes under conditions of constant hole diameter and remote stresses, the stress distribution on the crack plane varies widely. Thus, it is imperative that plate hole diameter to width ratios in the present work be carefully matched when generating crack plane stress distributions for the cases of load transfer to a fastener.

The finite element mesh for generation of crack plane stresses is shown in Figure 5.1 for  $d/t=1.0$  where the hole diameter to plate width ratio,  $\lambda$ , is 0.0833. For  $d/t=0.5$  and  $\lambda=0.04167$ , the plate width in Figure 5.1 is simply doubled. The 96 elements are of the eight node isoparametric type. Since precise values for stress concentration factors at the hole were not an issue, extremely fine divisions in this region were unnecessary. Rather, sufficient divisions across the minimum section to accurately approximate the gradient was deemed more important.

As a test of accuracy, the plate was loaded in uniaxial tension with the hole unloaded. A mesh of 72 elements having six divisions across the minimum section rather than the eight shown in Figure 5.1 was formed for a hole diameter to plate width ratio of 0.2. Figure 5.2 shows tangential (normal) stress across the minimum section versus distance from the hole edge. Results shown on Figure 5.2 compare well with those from the analytic solution reported by Savin (48) for the same problem.

For the loaded fastener hole case, equations 1.3.1 and 1.3.2 describe the surface tractions applied to the hole boundary. These

were integrated using Gaussian quadrature to produce nodal forces. Loading conditions were scaled to produce the desired load transfer ratios. Crack plane normal stress distributions for both values of hole diameter to plate width and three load transfer cases are shown in Figures 5.3 and 5.4. Results were calculated for a plate modulus of elasticity of  $30 \times 10^6$  psi and a Poisson's ratio of 0.25. For inclusion in the finite element-alternating method, these distributions were expressed as polynomials,

$$P(x) = A_0 + \sum_{n=1}^5 A_n x^n \quad (5.4.1)$$

over a range of  $x$  measured from the hole edge which encompassed the largest crack to be considered. A least square fit procedure produced the necessary coefficients and good accuracy with a fifth-order polynomial. The coefficients and limits of the polynomial expressions are listed in Table 5.1 for all three load transfer cases and the two hole diameter to plate width ratios.

To illustrate the convergent behavior of this method, the case of all the remote load transferred to the fastener was solved with meshes of 32, 72, and 96 elements. The increase from 32 to 72 elements changed the crack plane normal stress a maximum of 2% except at the far edge of the plate where the difference was 10%. A further increase to 96 elements altered 72 element results less than 1% everywhere. Exact division of the element arrangement was not possible here, thus this is not a strict convergence study.

Figure 5.5 shows results due to the present work for 72 finite elements compared to the analytic solution reported by Theocaris (28) where  $\lambda=0.2$  and Poisson's ratio is 0.365 in both methods. The results

Table 5.1 Polynomial Coefficients Describing Crack Plane Pressure for Load Transfer to a Fastener

d/t	d/w	Polynomial Coefficients	Q/P		
			1.0	0.5	0.1
0.5	0.04167	$A_0$	18.17	10.45	4.272
		$A_1$	-95.29	-52.44	-18.31
		$A_2$	202.10	111.2	39.11
		$A_3$	-203.90	-112.0	-39.55
		$A_4$	97.64	53.55	18.95
		$A_5$	-17.81	-9.76	-3.46
$(0 \leq \frac{x}{r} \leq 1.80)$					
1.0	0.0833	$A_0$	10.88	6.96	3.826
		$A_1$	-46.43	-28.17	-13.56
		$A_2$	93.95	57.25	27.89
		$A_3$	-95.15	-58.07	-28.40
		$A_4$	46.70	28.52	13.97
		$A_5$	-8.816	-5.38	-2.638
$(0 \leq \frac{x}{r} \leq 1.72)$					

$$P(x) = A_0 + \sum_{n=1}^5 A_n x^n$$

of Theocaris are expected to be somewhat different due to boundary conditions at the hole which permit shear in addition to radial loading yet great differences are not noted near the hole where the crack is to be located.

Cox and Brown (32) reported experimental photoelastic stress concentration factors at the minimum section found by Jessop, Snell and Hollister for neat fit loaded fasteners. For the cases of  $\lambda=0.04167$  and 0.0833, the finite element solution agrees to within 7% of these experimental results.

### 5.5 Theoretical Stress Intensity Factor Results for Cracks Emanating from Loaded Fastener Holes

Figures 5.6 through 5.13 present finite element-alternating method stress intensity factor results for cracks emanating from loaded fastener holes in finite-thickness plates. Results are shown for numerous crack locations with respect to the fastener hole, many crack shapes, and two hole diameter to plate thickness ratios. The magnification factor and parametric angle are as defined for the open hole problems. With the exception of Figure 5.6, each figure shows results for open holes ( $Q/P=0.0$ ) and 100% transfer of load to the fastener ( $Q/P=1.0$ ) only. This is to facilitate linear superposition to find stress intensity factors for cases of partial load transfer to the fastener. This linear superposition technique will be discussed in the next section.

All results for  $Q/P=1.0$  show the expected large increases in magnification factor, especially near the hole, due to the elevated stresses. This same steep stress gradient tends to magnify subtle

differences in stress intensity factor along the crack periphery seen in the open hole results for the same crack.

Figures 5.12 and 5.13 show magnification factors for the same embedded crack and two hole diameter to plate thickness ratios. The open hole case was discussed in Chapter 4 where the decrease in magnification factor with decreasing  $d/t$  was noted. When this same situation occurs in the loaded hole case, the asymptotic behavior of the normal stress field near the hole causes the average stress in the region of the crack to increase for the  $d/t=0.5$  situation with respect to the  $d/t=1.0$  case. Thus magnification factors are now increased with decreasing  $d/t$ .

Figures 5.8 and 5.9 show results for single and double cracks of the same shape. The comments of Chapter 3 regarding magnification factor differences for single and double cracks emanating from an open hole are also true for the case of 100% load transfer to a fastener filled hole. Again, the maximum difference of about 8% occurs in the vicinity of a parametric angle of 30 degrees with smaller differences occurring at the hole and front surface intersections.

### 5.6 Stress Intensity Factors for Partial Load Transfer to the Fastener

Stress intensity factors for partial transfer loads,  $0.0 < Q/P < 1.0$ , (Figure 1.5b) can be found by linear superposition of results for the open hole ( $Q/P=0.0$ ) and 100% load transfer ( $Q/P=1.0$ ) cases. As an example, suppose stress intensity factors are to be found for a single quarter-elliptical crack emanating from a fastener hole with  $a/c=0.5$ ,  $a/t=0.25$ ,  $d/t=1.0$ , and a 10% transfer of load to the fastener ( $Q/P=0.1$ ).

Figure 5.14 shows how linear superposition of the open hole and 100%

load transfer results forms this partial load transfer and Figure 5.6 shows the magnification factors for the  $Q/P=0.0$  and  $1.0$  cases. From Figure 5.6, a stress intensity factor is calculated for these two cases using magnification factors at some location along the crack periphery and the adjusted remote stress suggested in Figure 5.14. Addition of these stress intensity factors produces the desired partial load transfer stress intensity factor at the same location on the crack front.

Figure 5.6 includes results for  $Q/P=0.1$  and  $0.5$  which are not linear superposition results but rather are from direct calculations using the finite element-alternating method and the appropriate stress distributions for these load transfer cases. This provides a check on the accuracy of partial load transfer stress intensity factors found with linear superposition. For  $Q/P=0.5$ , linear superposition results agree to within 2% of results from direct finite element-alternating method calculations and within 4% for  $Q/P=0.1$ . Thus, Figures 5.7 through 5.13 present only open hole and 100% load transfer results since linear superposition is capable of producing accurate stress intensity factors for any intermediate partial load transfer to the fastener.

The fact that linear superposition is accurate raises another interesting point. Solution 2 of the finite element-alternating method requires that pressure over the crack be expressed as a ten-term polynomial (Equation 2.3.1). For cases of load transfer to the fastener, this is accomplished by a least-square-fit to the crack pressure predicted by the two-dimensional finite element results of this chapter. As the amount of load transferred to the fastener increases, the normal stress gradient at the hole becomes steeper (Figure 5.3) and, one would

think, subject to greater errors when approximated by the polynomial. On the contrary, the fact that linear superposition agrees closely with direct calculations for partial load transfer to the fastener indicates that errors in the load transfer results are no worse than for the open hole case where the mean deviation in the crack pressure averages about 8% of the maximum value.

It should be noted that this superposition applies only to the hole diameter to plate width ratios used in this work. Theoretical results were calculated based upon crack plane stress distributions for two specific plate sizes. The 100% load transfer case is very sensitive to the hole diameter to plate width ratio with crack plane normal stresses varying greatly with the changing plate dimensions. While it is possible to use linear superposition to extend results to other plate widths, it should be recognized that errors can be induced and in no case should these results be extended to hole diameter to plate width ratios greater than 0.2.

### 5.7 Comparison with Results of Other Authors

Stress intensity factor results for cracks emanating from loaded fastener holes to compare with the present work are rather limited. Cartwright and Ratcliffe (47) used experimental compliance methods to produce stress intensity factors for double through-cracks at a loaded fastener hole (Figure 1.2), but hole diameter to plate width ratios are so different as to prevent comparison with the present work.

Shah (12) applied his Green's function approach to estimate stress intensity factors for the loaded hole case. He presents two-dimensional stress intensity factors for single (Figure 1.1) and double (Figure 1.2)

through-cracks and three-dimensional results for circular cracks emanating from loaded fastener holes. For a comparison by the finite element-alternating method, the two-dimensional through-cracks were approximated by slender part-elliptical cracks as described in Chapters 2 and 3 and stress intensity factors for loaded hole cases where  $L/R=1.5$  were calculated. The finite element-alternating method predicted the stress intensity factor for the single through-crack to be 17% below Shah's result and for double through-cracks to be 10% low. The differing plate dimensions and resulting expressions for crack plane stresses account for the majority of these differences. Figure 5.11 shows a typical three dimensional Shah estimate and the corresponding finite element-alternating method result. Shah neglects crack shape effects and presents results for circular cracks only. This accounts for the difference in magnification factor near the front surface intersection. Differences near the hole are probably due to the differing expressions for the gradient near the hole in the two methods.

Grandt (14) also presents stress intensity factors for the single through-crack at a loaded fastener hole (Figure 1.1). A stress distribution due to Harris, et al., (33) for a plane inclined at  $\beta=8^\circ$  (Figure 1.5b) is sufficiently different from the results of the present work that the stress intensity factor calculated by the finite element-alternating method is now 10% higher than Grandt's result for  $L/R=1.5$ .

Comparisons of the present theory with a large number of static fracture tests performed by the author are presented in Chapter 6. Agreement is more consistent over a wider variety of three-dimensional crack shapes and locations relative to the fastener hole than the comparisons shown above.

## CHAPTER 6

### STATIC FRACTURE TESTS

#### 6.1 Introduction

A series of static fracture tests on polymethylmethacrylate (PMMA) specimens was performed to verify the theoretical solution method presented in this work. These tests included numerous crack shapes and locations relative to both open and loaded fastener holes in plates with two hole diameter to plate thickness ratios (Figures 2.1 and 1.5). Comparisons with experiments are made at locations on the crack periphery where the stress intensity factors are maximum as determined by the theory.

#### 6.2 Modeling of the Fracture Process with PMMA

Many researchers have used polymers such as epoxy, polycarbonates and PMMA to model the fracture process (21, 46, 49, 50, 51). Transparency of these materials allows viewing of the crack front which is hidden in engineering metals. Additionally, the fatigue properties and fractured surface characteristics of polymers are similar to those of metals.

PMMA is ideally suited to the large number of tests performed in the present experiment due to its commercial availability in bulk under the trade name Plexiglas. PMMA is also relatively isotropic and brittle. Under normal testing conditions, it has a tensile strength of about  $7 \times 10^3$  psi, a modulus of elasticity of  $4.5 \times 10^5$  psi and an elongation at fracture of about 5%.

### 6.3 Specimen Preparation

Specimen blanks were cut from two 4 x 8 foot sheets of commercial Plexiglas having a nominal thickness of 1/2 inch. Each blank was oriented in the same direction with respect to the sheet from which it was cut. Specimens were approximately 7 inches long and 3 inches wide where the length was limited by the maximum grip spacing of the testing machine. The width was chosen to approximate that of an infinite plate for the open hole case while at the same time providing economy in the number of specimens fashioned from a Plexiglas sheet. Additionally, all plate and crack dimensions were far greater than the parameter B, where

$$B = 2.5 (K_{IC}/\sigma_{ys})^2 . \quad (6.2.1)$$

Jones and Brown (52) suggest that this should be the case for a valid plane strain fracture toughness test where plasticity effects must be small and localized.

To grow single corner cracks with  $a/c < 1.0$  (Figure 2.1a), the specimen was placed in bending using the cracking jig shown in Figure 6.1. A razor blade was touched to the tension side of the blank producing a semi-elliptical surface crack whose center is offset the length of a hole radius from the specimen centerline. The fastener hole and remote loading holes were then carefully drilled and reamed.

Preparation of double crack specimens with  $a/c < 1.0$  (Figure 2.1b) was similar with one important exception. Here, the dual cracks were grown in the same cracking jig using a specially fashioned razor blade which simultaneously produced separate surface cracks on opposite sides of the hole location. As before, the fastener hole was then

drilled and reamed such that the major axis of each surface crack was bisected by the hole.

A new device was designed and procedures developed to grow single and double cracks with  $a/c > 1.0$  (Figures 2.1a and 2.1b) and embedded cracks (Figure 2.1c) emanating from fastener holes. First, the fastener holes and appropriate loading holes were drilled and reamed. The specimen was then loaded at remote holes offset from the specimen centerline to produce combined axial loading and bending. The crack was introduced on the side of the fastener hole where the tensile stresses due to the axial loading were reduced by the compression due to bending. This allowed for better control and prevented unstable growth during placement of the crack.

The cracking jig is shown in place on a specimen in Figure 6.2c. A small razor blade is a fixed to a rod which is aligned parallel to the hole centerline. With load on the specimen, the jig is tightened which presses the blade against the edge of the hole. Centering the jig at the center of the plate through-the-thickness produces an embedded crack while offset of the jig toward a plate surface produces a single corner crack at the hole. Double corner cracks were grown in a similar manner. First one crack was placed as explained above for the single deep corner crack. The load was then reduced and the cracking jig rotated to the opposite side of the plate where the second crack was grown.

In all cases, crack sizes and shapes could be controlled with razor blade length and loading conditions. Exact duplication of crack geometries was, however, not possible yet the growth of cracks with similar geometries was deemed important due to the inherent scatter

in fracture tests of this type. Thus, comparisons with the present theory are always made with more than one experimental result.

#### 6.4 Slow Growth in PMMA

Fracture in PMMA frequently includes slow growth preceding rapid crack extension. The region of slow growth on the fractured surface is rippled while the region of rapid crack extension is identified by a mirrored surface. This is clearly seen on all the fractured surfaces pictured in Figure 6.3. In tests performed here, slow growth began at specific points on the crack front which could be identified visually. The location of initial slow growth depended upon the crack shape and orientation with respect to the hole and can be assumed to coincide with the location of maximum stress intensity. The benefit here is that experimental and theoretical comparisons can be done at a specific location on the crack periphery rather than the gross comparison necessary if the experiment does not show where the maximum stress intensity occurs.

A series of load versus crack opening displacement curves was obtained for surface flawed PMMA specimens with and without fastener holes. This was done in order to assess the relative importance of the slow growth and the accuracy of the visual procedure in predicting its onset. A small linear differential transformer was mounted over the cracks and connected to an x-y plotter. A typical curve is shown in Figure 6.4 for double surface cracks emanating from a fastener hole. In all cases, the onset of slow growth could be visually seen to begin at loads no more than 3% above those predicted by the load-displacement records. The load at the onset of slow growth, determined visually,

was taken as the critical load for calculation of an experimental magnification factor to be compared with the theoretical predictions. The location of the initial growth was assumed to be the location of maximum stress intensity.

A series of experiments was recorded on high-speed 16 mm movie film. Analysis of this film qualitatively supports the observations noted above. Additionally, when these films are used in conjunction with inspection of the fractured surfaces and parametric plots of stress intensity factors from the present theory, interesting conclusions regarding crack growth can be formed. The fractured surfaces from some of the movie tests are pictured in Figure 6.3 and remarks on the slow growth seen will be made later in this chapter.

### 6.5 Specimen Testing

Prior to testing, specimen widths and thicknesses were recorded. All specimens were loaded to failure in an Instron Testing Machine at a loading rate of 0.02 inches per minute to avoid strain rate effects. For each specimen, the location on the crack periphery at which slow growth began and the corresponding load were noted. Crack dimensions were measured with a dial gage following failure.

The loading arrangements for open holes and 100% load transfer to a fastener are shown in Figures 6.2a and 6.2b. All loading fixtures were carefully machined and aligned to eliminate plate bending effects. The fastener was machined to 0.4% clearance to simulate a neat fit and lubrication was applied to approximate the smoothness condition at the hole-fastener interface.

The laboratory atmosphere was not controlled specifically during testing. Minor changes in temperature and humidity which did occur are deemed not significant.

### 6.6 Data Reduction

A data reduction method referred to as the baseline method is used in this work. This method has been applied in a number of earlier studies (46, 50, 53) and will be used here as follows. For a semi-elliptical surface crack in a finite thickness plate, the stress intensity factor can be defined as

$$K_I = M_1 M_2 \sigma \sqrt{\pi a / Q} \quad (6.6.1)$$

where  $M_1$  and  $M_2$  are the front surface and back surface correction factors respectively, and  $Q$  is the usual crack shape parameter. The front surface correction factor,  $M_1$ , is a function of  $a/2c$  while the back surface correction factor,  $M_2$ , is a function of both  $a/2c$  and  $a/t$ . As  $a/t$  approaches zero, the back surface effect disappears and  $M_2$  approaches a value of unity. Smith and Alavi (37) solved for stress intensity factors around the periphery of a semi-elliptical crack in the surface of a semi-infinite solid. For small  $a/2c$  values, the deepest position on the crack front is most critical and the above authors approximated the front surface correction factor at this location by

$$M = 1.12 - .0476 (a/2c) - .227 (a/2c)^2, \quad (a/2c \leq 0.42) \quad (6.6.2)$$

More recent investigations by Smith and Sorensen (39) and Shah and Kobayashi (13) predict front surface effects which are about 2% lower

over the range of crack shapes considered here. Nevertheless, Equation 6.6.2 provides a useful functional relationship for the purposes of this study. Thus for low values of  $a/2c$  and small  $a/t$ , the front surface correction is known and the back surface correction can be taken as unity. If the remote failure stress and crack dimensions can be measured using suitable surface cracked baseline specimens, the critical value of  $K_I$ , or the fracture toughness, can be determined for the material. This value will be defined as the apparent fracture toughness,

$$AK_{IC} = M_1 \sigma \sqrt{\pi a / Q} . \quad (6.6.3)$$

Separate baseline tests were conducted for each of the two PMMA sheets. Baseline specimens were approximately 1.5 inches wide versus 3 inches for the fastener hole specimens. All other dimensions were the same as for the fastener hole tests. Smith (46) showed that for surface flaws, specimen width effects were unimportant for  $a/2c < 0.3$  if  $w/2c$  is larger than 3 where  $w$  is the specimen width. Several baseline specimens fell slightly outside this range yet no evidence of width effects could be seen.

The results of the two baseline studies are shown in Figures 6.5 and 6.6. The values of  $AK_{IC}$  were taken as the average of values for all specimens tested from each plate. The maximum data scatter in each test was  $\pm 7\%$ . Fracture toughness results obtained here agree well with those of other experiments (55).

The slow growth phenomena in PMMA raises questions about the validity of the apparent fracture toughness values obtained from the baseline tests performed here. Brown and Srawley (56) commented to

great lengths on the original concept of Irwin (57) regarding resistance to crack extension during a fracture toughness test. Irwin proposed that the crack extension force,  $G$ , was balanced by increasing resistance to crack extension,  $R$ . A condition of equilibrium between  $G$  and  $R$  is maintained to the point of crack instability. Should large amounts of crack slow growth occur, it is possible that the instability point could be located incorrectly, resulting in values for fracture toughness which are in error. Crack opening displacement plots made on surface flawed baseline specimens in this work showed slow growth to occur within no more than 3% of the maximum load. Additionally, this growth was very rapid and nearly impossible to view, being detected primarily on the fractured surfaces after failure. Therefore, the author feels slow growth in the PMMA baseline tests performed here to have little effect on the resulting fracture toughness values presented. Also, since the load at the onset of slow growth and the load at which specimen separation occurs are so close, the separation load is used to calculate the apparent fracture toughness values.

The apparent fracture toughness found from the baseline tests is used in the reduction of experimental data from the fastener hole tests as follows. The magnification factor is defined as

$$MF = \frac{AK_{IC}}{\sigma\sqrt{\pi b}} \quad (6.6.4)$$

where  $\sigma$  is the remote stress at the onset of slow growth in an open hole test and  $b$  is the crack minor axis regardless of crack orientation. For cases of 100% load transfer to the fastener, the stress is expressed as a bearing stress,

$$\sigma_b = \frac{P}{dt} , \quad (6.6.5)$$

where  $P$  is the remote load at the onset of slow growth,  $d$  is the hole diameter, and  $t$  is the plate thickness. This is necessary in comparisons with the theory due to differing theoretical and experimental plate widths. The definition of magnification factor shown above does not separate the various effects on the stress intensity factor mentioned in Chapter 2 but describes a combined effect for each problem. This is entirely suitable for the purpose of verification of the present theory since the theoretical magnification factors predicted in this work also do not distinguish between these effects.

### 6.7 Comparison of Theory with Experiments

Figures 6.7 through 6.22 present comparisons of experimental and theoretical magnification factors. Each figure shows results for a particular crack location with respect to open and loaded fastener holes. Experimental magnification factors as defined in the previous section are plotted versus the non-dimensional crack depth,  $a/t$ , and the range of crack shapes in each figure is small. Theoretical calculations were made for crack shapes and depths which are close to the average experimental crack shape and depth values for the experiments plotted. The theoretical magnification factor is defined as

$$MF = \frac{K_I}{\sigma_b \sqrt{\pi b}} \quad (6.7.1)$$

for open hole cases or

$$MF = \frac{K_I}{\sigma_b \sqrt{\pi b}} \quad (6.7.2)$$

for 100% transfer of load to a fastener where  $\sigma_b$  and  $b$  are as defined for the experimental magnification factor. Problem dimensions are as depicted in Figure 2.1.

Magnification factor comparisons are made at points on the crack periphery corresponding to the location of onset of slow growth in the experiments. In most cases this also corresponded to the location of maximum theoretical magnification factor. One exception is the series of tests for hole diameter to plate width ratios,  $d/t$ , of 0.5. These specimens exhibited little or no slow growth so it was impossible to determine from the experiment at what position along the crack border to make comparison with the theory. Therefore, comparisons are made at locations on the crack periphery where the theory predicts the magnification factor to be maximum. Another exception is the embedded crack where the slow growth region was very small, but it covered a range of the crack border encompassing the location of the maximum theoretical magnification factor.

Experimental data scatter in 11 of the 15 comparative plots is less than  $\pm 9\%$ . The remaining four figures (6.9, 6.13, 6.16, and 6.20) show larger data scatter. This is generally the result of one data point being separated from an otherwise close grouping of experimental results. Scatter in these four figures is reduced to less than  $\pm 10\%$  if the separated data points are not considered. However, if all points are used, experimental data scatter ranges from  $\pm 11\%$  to  $\pm 18\%$  in these four cases.

Theoretical calculations are for a material with a Poisson's ratio of 0.25 while for PMMA this value is about 0.35. Smith (46) noted a 3% increase in theoretical back surface correction factors with an

increase in Poisson's ratio from 0.25 to 0.39 in studies of semi-elliptical surface cracks. Assuming this increase would also apply in the present work, all theoretical magnification factors should be raised 3%. However, it was noted in an earlier section that the visual procedure used to predict loads at the onset of slow growth in PMMA was about 3% high. If such a correction was applied to all experimental points, magnification factors would increase 3%. Since the Poisson's ratio effect and the correction to the visual procedure both predict adjustment in the same direction, all experimental and theoretical points on the figures would simply be higher by about 3%. The offsetting nature of these corrections is rather unimportant in the present comparison and thus is not shown on the figures to follow.

For purposes of explaining the differences between theoretical and experimental results shown in Figure 6.7 through 6.22, a percent difference will be defined as:

$$\% \text{ Difference} = \frac{MF_{\text{Theoretical}} - MF_{\text{Experimental}}}{MF_{\text{Theoretical}}} \times 100 \quad (6.7.3)$$

Figure 6.7 through 6.10 show comparisons of experimental and theoretical magnification factors for single corner cracks adjacent to both open and loaded fastener holes where the hole diameter to plate width ratio,  $d/t$ , is 1.0. The open hole comparisons are within 8% while the two cases of 100% load transfer to the fastener show differences of 13% and 17%.

Double crack comparisons for  $d/t=1.0$  and both open and loaded holes are shown in Figures 6.11 through 6.14. The open hole comparison in Figure 6.11 is very close while in Figure 6.12 the average experimental value is about 6% below the theoretical prediction. Figures

6.13 and 6.14 show 100% load transfer comparisons and have the experimental results about 16% and 5% lower, respectively, than the theory.

Comparisons of theoretical and experimental magnification factors for embedded cracks are shown in Figures 6.15 and 6.16 for  $d/t=1.0$ . The open hole case of Figure 6.15 has the experimental results about 9% low while the 100% load transfer case comparison in Figure 6.16 is very good.

Figures 6.17 through 6.22 show comparisons for cases of  $d/t=0.5$ . All three crack locations with respect to the hole are represented. With the exception of Figure 6.22 which is for 100% load transfer to a fastener, comparisons shown are for open holes. The embedded crack cases of Figures 6.21 and 6.22 show very good agreement with the present theory. Single and double crack comparisons in Figures 6.17 through 6.20 have the experimental results from 19% to 31% lower than the theory.

Although the agreement between theoretical and experimental magnification factors in most cases presented here is good, the differences which do occur can perhaps be at least qualitatively explained. The existence of a small yield zone around the periphery of a crack has been well established. The size of this crack-tip yield zone increases with increasing local stresses in the neighborhood of the crack. All cracks in this study are located in a region of high stress concentration near a hole in a plate. Additionally, comparisons between experiments and theory are generally made at points of intersection of the crack with a plate surface. Crack-tip plastic zones at these locations are expected to be larger than at other locations along the crack periphery.

Using experimental failure loads, estimates of stresses in the vicinity of cracks emanating from fastener holes in the PMMA tests performed here can be made. It is then possible to obtain a qualitative judgment of the importance of plastic deformation in the experiment. A plot of percent deviation between theory and experiment versus the ratio  $\sigma_{\max}/\sigma_{ys}$  is shown in Figure 6.23 for all cases except embedded cracks which will be discussed later. A strong trend in this plot indicates deviations from the theory of from 12% to 31% for experiments in which  $\sigma_{\max}/\sigma_{ys}$  exceeded 0.75. However, when  $\sigma_{\max}/\sigma_{ys}$  was less than 0.75, agreement was good and the deviation never exceeded 8%. It is thus not possible to ignore plasticity effects in the experiments for high ratios of  $\sigma_{\max}/\sigma_{ys}$  which probably accounts for much of the deviation from the theory for the  $d/t=0.5$  and 100% load transfer cases.

The closest theoretical to experimental agreement for a particular crack location with respect to a fastener hole occurred for cases of embedded cracks regardless of loading conditions or hole diameter to plate thickness ratios. Although local stresses were also high in these tests, magnification factors are compared at a location well removed from the hole surface and plate lateral surfaces. Yield zones are most probably smaller at this location than at surface intersections where comparisons are made for most other cases.

#### 6.8 Some Observations on Crack Growth in the Present Experiments

The experiments conducted by the author were for the expressed purpose of verification of the present theory. In the course of the experimentation, however, interesting slow growth near cracks emanating from fastener holes in PMMA was noted. For certain cases, this

phenomena was recorded on movie film and for all tests the fractured surfaces were carefully inspected. An analysis of the growth behavior using the present theory is of sufficient interest to be included here.

Figure 6.3 shows photographs of six specimens following fracture. High speed 16 mm movies were also taken of these same specimens during loading. The upper four photographs in the figure are open hole cases and have the initial crack shape outlined for better definition. The bottom two pictures are for 100% transfer of load to the fastener. Here, the initial crack shape is more easily seen and is not outlined. The fractured surfaces on the six specimens are representative of surfaces seen in all experiments.

In the photographs of Figure 6.3, the regions of slow growth are the rippled surfaces while rapid crack extension is typified by the mirrored surfaces. Theocaris (59) explained that the wavy surface of the slow growth region is caused by a similarly wavy elastic area outside a circular highly strained zone around the crack tip. As the crack grows through this rippled elastic region, the fractured surface likewise becomes wavy.

Figures 6.3a and 6.3b show fractured surfaces for single and double corner cracks of low  $a/c$ . Slow growth initiates at the hole intersection in both cases and growth patterns are similar. Rarely is any growth seen at the front surface intersection. Figure 6.24 is a plot of  $K_I/\sigma$  versus  $a/c$  using the present theoretical results in an attempt to explain this growth pattern where slow growth is depicted from left to right on the figure. As slow growth proceeds from regions near the hole, stress intensity factors increase at both the hole and surface intersections but more so at the front surface. The crack

grows in such a fashion as to attempt to equalize stress intensity factors all along the crack periphery.

Figure 6.3c shows a photograph of double cracks which are longer in the hole direction than along the front surface. Here and in similar single crack cases, slow growth begins at the front surface intersection but soon occurs everywhere along the crack periphery. Figure 6.25 is a parametric plot of theoretical results for this observed growth pattern where slow growth is depicted from left to right on the figure. At step 1 on this figure ( $a/c=3.0$ ,  $a/t=0.5$ ) the stress intensity factor at the front surface intersection is largest so growth begins there. Between Steps 1 and 2 ( $a/c=2.0$ ,  $a/t=0.5$ ), the location of maximum stress intensity shifts to the hole intersection and growth begins at this point also. Steps 3 and 4 ( $a/c=1.5$ ,  $a/t=0.75$ , 0.9) show increases everywhere as growth continues all along the crack border.

The fractured surface shown in Figure 6.3d is typical for an embedded crack emanating from an open hole in PMMA. A small slow growth area is seen between the initial crack and one plate lateral surface. The remaining fractured surface is mirrored. Figure 6.26 is a parametric plot of theoretical results approximating this case where slow growth is depicted from right to left on the figure. Growth is assumed to initiate at the location of maximum stress intensity, in this case at a parametric angle of about 40 degrees from the crack minor axis. The crack shape changes in such a manner that stress intensities rapidly increase at this location but decrease at the hole intersection and rapid fracture follows.

Figures 6.3e and 6.3f are photographs of typical fractured surfaces for two cases in which 100% of the remote load is transferred to

the fastener-filled hole. Here, either rapid crack extension or slow growth followed by rapid crack extension begins at the hole intersection. Crack arrest occurs when the crack shape approximates that of a through-crack for which stress intensity factors are lower. This is followed by more slow growth of the new through-crack shape over rather large distances across the plate half-width.

## CHAPTER 7

### 'CRACK OPENING DISPLACEMENTS

#### 7.1 Problem Statement

Unlike the method presented in this work, some stress intensity factor solution use prior knowledge of crack opening displacements. The calculation of these displacements, while not a primary objective of this work since stress intensity factors are calculated independently, is sometimes useful in extending solutions to cracks of other geometries. Therefore, a simple relationship for opening displacements of surface cracks emanating from fastener holes is presented in this section.

#### 7.2 Solution Method

One of the solutions used in the finite element-alternating method is that of an embedded elliptical crack in an infinite solid. Shah and Kobayashi (13) extended the solution by Green and Sneddon (41) for this problem to allow arbitrary normal loading on the crack where this loading is expressible as a ten-term polynomial in  $x$  and  $y$ . The details of their work are widely known and will not be presented here. However, a brief description of the problem and their solution method is necessary to provide background for the present work.

Navier's displacement equations of elasticity are identically satisfied by a harmonic function,  $\phi$ , if  $\phi$  satisfies Laplace's equation,

$$\nabla^2\phi = 0 , \quad (7.2.1)$$

provided shear is zero on the plane  $z = 0$ . The  $z$  displacement component of interest here is

$$w = z \frac{\partial^2 \phi}{\partial z^2} - 2(1-\eta) \frac{\partial \phi}{\partial z} . \quad (7.2.2)$$

On the crack plane,  $z = 0$ , this equation reduces to

$$w = - 2(1-\eta) \frac{\partial \phi}{\partial z} \quad (7.2.3)$$

where  $\eta$  is Poisson's ratio.

Ellipsoidal coordinates  $\lambda$ ,  $\mu$ , and  $\nu$  are introduced to solve the boundary value problem, where these coordinates are roots of the equation in  $s$ ,

$$\frac{x^2}{a^2+s} + \frac{y^2}{b^2+s} + \frac{z^2}{s} - 1 = 0 , \quad (7.2.4)$$

and the ellipsoidal and cartesian coordinates are related by

$$a^2(a^2-b^2)x^2 = (a^2+\lambda)(a^2+\mu)(a^2+\nu) , \quad (7.2.5)$$

$$b^2(b^2-a^2)y^2 = (b^2+\lambda)(b^2+\mu)(b^2+\nu) , \quad (7.2.6)$$

$$a^2b^2z^2 = \lambda\mu\nu , \quad (7.2.7)$$

subject to the standard restriction,

$$-a^2 \leq \nu \leq -b^2 \leq \mu \leq 0 \leq \lambda < \infty .$$

In the ellipsoidal coordinate system,  $\lambda = 0$  represents the region in the  $z = 0$  plane, interior to the crack, while  $\mu = 0$  represents the region outside the crack in this same plane.

Segedin (60) suggested the use of a harmonic potential function

$$\psi^{(n)} = \int_{\lambda}^{\infty} \frac{w^n(s)ds}{\sqrt{Q(s)}} \quad (7.2.8)$$

where

$$w(s) = 1 - \frac{x^2}{a^2+s} - \frac{y^2}{b^2+s} - \frac{z^2}{s} \quad (7.2.9)$$

and

$$Q(s) = s(a^2+s)(b^2+s) \quad (7.2.10)$$

The general stress function,  $\phi$ , is formed as a polynomial in  $v^{(n)}$ ,

$$\phi = \sum_{i=0}^3 \sum_{j=0}^3 \frac{c_{ij} v^{(i+j+1)}}{\partial x^i \partial y^j} \quad (i+j \leq 3) \quad (7.2.11)$$

or  $\phi$  itself can be expressed as the double series,

$$\phi = \sum_{i=0}^3 \sum_{j=0}^3 \phi_{ij} \quad (i+j \leq 3) \quad (7.2.12)$$

From equation (7.2.3), the calculation of crack opening displacements involves only the first derivative of  $\phi$  and each term in the series (7.2.12) can be differentiated separately. In the interest of brevity, only  $\frac{\partial \phi_\infty}{\partial z}$  will be presented in detail to illustrate the procedure.

From equation (7.2.8),

$$\frac{\partial \phi_\infty}{\partial z} = C_\infty \frac{\partial}{\partial z} \int_{\lambda}^{\infty} \frac{w(s) ds}{s \sqrt{Q(s)}} \quad (7.2.13)$$

where  $C_\infty$  differs from  $c_\infty$  by an integral constant. Using the Leibnitz rule for differentiating integrals,

$$\frac{\partial \phi_\infty}{\partial z} = -2zC_\infty \int_{\lambda}^{\infty} \frac{ds}{s^2 \sqrt{Q(s)}} \quad (7.2.14)$$

The integral in equation (7.2.14) can be expressed in terms of elliptic integrals and Jacobian elliptic functions and the limiting form of  $\frac{\partial \phi_\infty}{\partial z}$  can be found by setting  $\mu = 0$  and approaching the crack tip from outside. While this seems straightforward, the work necessary to obtain the ten first derivatives needed for crack opening displacements

AD-A045 349

AIR FORCE INST OF TECH WRIGHT-PATTERSON AFB OHIO  
SURFACE CRACKS EMANATING FROM FASTENER HOLES. (U)  
1976 T E KULLGREN  
AFIT-CI-77-21

UNCLASSIFIED

F/6 20/11

NL

2 OF 3  
AD  
A045349



is excessive and tedious. Nevertheless, several derivatives were calculated in this fashion resulting in answers identical to those obtained by the easier approach which follows.

If a limiting process in  $z$  is applied directly to the integral in equation (7.2.14), the amount of tedious calculation and bookkeeping is considerably reduced. Approaching the crack plane from above,

$$\frac{\partial \Phi_{\infty}}{\partial z} = -2C_{\infty} \lim_{z \rightarrow 0} \frac{f(z)}{1/z} \quad (7.2.15)$$

where

$$f(z) = \int_{\lambda}^{\infty} \frac{ds}{s\sqrt{Q(s)}} \quad (7.2.16)$$

Since equation (7.2.15) is an indeterminate form, applying L'Hospital's rule yields

$$\frac{\partial \Phi_{\infty}}{\partial z} = -2C_{\infty} \lim_{z \rightarrow 0} \frac{f'(z)}{-1/z^2} \quad (7.2.17)$$

Again, using the Leibnitz rule,

$$f'(z) = -\frac{1}{\lambda\sqrt{Q(\lambda)}} \frac{\partial \lambda}{\partial z} \quad (7.2.18)$$

Calculating  $\frac{\partial \lambda}{\partial z}$  from (7.2.7), substituting  $Q(\lambda)$  from (7.2.10), and performing the necessary algebra leads to

$$\frac{\partial \Phi_{\infty}}{\partial z} = -\frac{4C_{\infty}\sqrt{\mu\nu}}{a^2b^2} \quad (7.2.19)$$

where  $\mu\nu = a^2b^2 - b^2x^2 - a^2y^2$ . The calculation of the remaining nine derivatives proceeds in a similar fashion. The final crack opening displacement equation is shown in Appendix B.

To check the limiting process used in obtaining the ten derivatives along with the algebra involved, crack opening displacements were

calculated for a circular crack under constant and linearly varying normal pressure. The circular crack was approximated by a near-circular elliptical crack with  $a/b = 0.99$ . Since this analysis is being done algebraically, there is no concern about the ratio  $a/b$  causing numerical difficulties such as those mentioned in Chapter 2. Shah and Kobayashi (22) provide the necessary stress function coefficients for the two loading cases. Smith (45) solved this same problem for loading expressed in the form of a Fourier series. Crack opening displacements calculated by the present method compare with Smith's values to within 0.50% for both loading cases. This small difference is probably due to the approximation of a circular crack with a near-circular elliptical crack.

### 7.3 Solution Results

A necessary prerequisite to the calculation of crack opening displacements using the method of this section is a knowledge of the stress function coefficients,  $C_{ij}$ , for a given problem geometry. For each iteration of the finite element-alternating method, stress intensity factors and stress function coefficients are calculated based upon the freeing of normal stress on the crack plane.

A final set of stress function coefficients for a particular case is formed by summing like coefficients for each iteration. Appendix A lists the final stress function coefficients for all problems solved. Crack opening displacements are found by using the equation in Appendix B together with a set of stress function coefficients from Appendix A. Figure 7.1 shows a typical result in the form of a three-dimensional plot of crack opening displacements for the case of a single corner crack emanating from an open hole in an infinite plate.

## CHAPTER 8

### CONCLUSION

#### 8.1 Discussion

A new method developed by Browning (3), Ganong (4) and the author was used to predict stress intensity factors for three-dimensional linear fracture mechanics problems not previously solved. This technique, called the finite element-alternating method, produced stress intensity factors around the periphery of surface cracks emanating from fastener holes in finite-thickness plates. Problems solved included three crack locations with respect to the hole and numerous crack shapes. Two hole diameter to plate thickness ratios were considered and results were presented for both open and fastener-filled holes to which a portion of the remote load is transferred.

The solution method presented is accurate, economical and capable of modeling complex three-dimensional geometries. Comparisons of present results with estimates of other authors showed similar trends but better accuracy due to the accounting for all effects in the problems considered. Agreement with independent fatigue experiments by Snow (20) is good for the several crack shapes and depths considered. Comparisons of the present theory with stress freezing photoelastic experiments by McGowan and Smith (19) are erratic at best. The author feels that the results from these experiments are in error, particularly at locations of crack intersection with a hole.

Static fracture tests in PMMA were conducted to provide additional verification of the theoretical calculations performed. New experimental procedures allowed for testing of specimens having three crack

orientations with respect to the hole and many different crack shapes. Two hole diameter to plate thickness ratios were duplicated and specimens with load transfer to a fastener were tested. Agreement between these experiments and the present theory at specific locations on the crack periphery was good in most cases. This provided verification of the theory for crack locations with respect to the hole and plate loading conditions not considered in previous experiments.

### 8.2 Recommendations

The finite element-alternating method presented in this work uses as one solution that of stresses in an infinite body due to pressure on an embedded elliptical crack where this pressure is described by a ten-term polynomial. In the present solution, a least-square fit to the actual pressure produces the required polynomial coefficients. This polynomial approximation accurately predicts the total force applied to the crack and correctly reflects trends in the stress gradients yet subtleties in the pressure are not precisely reproduced. The resulting magnification factors are probably slightly in error. A more accurate representation of this portion of the finite element-alternating method, such as a Green's function solution, would be an improvement.

## REFERENCES

1. Military Specification MIL-A-XXXX(USAF), "Airplane Damage Tolerance Design Requirements," October 1973.
2. Gran, R. J., Orazio, F. D., Paris, P. C., Irwin, G. R. and Herzberg, R., "Investigation and Analysis Development of Early Life Aircraft Structural Failures," Technical Report AFRL-TR-70-149, Wright-Patterson Air Force Base, Ohio, March 1971.
3. Browning, W. M., "The Analysis of a Semi-Circular Crack Emanating from a Hole in a Plate," Doctoral Thesis, Colorado State University, December 1974.
4. Ganong, G. P., "Quarter-Elliptical Cracks Emanating from Holes in Plates," Doctoral Thesis, Colorado State University, July 1975.
5. Bowie, O. L., "Analysis of an Infinite Plate Containing Radial Cracks Originating at the Boundary of an Internal Circular Hole," Journal of Mathematics and Physics, Vol. 35, 1956, pp. 60-71.
6. Tweed, J. and Rooke, D. P., "The Distribution of Stress Near the Tip of a Radial Crack at the Edge of a Circular Hole," International Journal of Engineering Science, Vol. 11, 1973, pp. 1185-1195.
7. Kobayashi, A. S., "A Simple Procedure for Estimating Stress Intensity Factor in Region of High Stress Gradient," Significance of Defects in Welded Structures, Proceedings of the Japan-U.S. Seminar, Tokyo, 1973.
8. Hsu, T. M. and Liu, A. F., "Stress Intensity Factors for Truncated Elliptical Cracks," Seventh National Symposium on Fracture Mechanics, College Park, Maryland, August 1973.
9. Liu, A. F., "Stress Intensity Factor for a Corner Flaw," Engineering Fracture Mechanics, Vol. 4, 1972, pp. 175-179.
10. Smith, F. W., Emery, A. F. and Kobayashi, A. S., "Stress Intensity Factors for Semicircular Cracks," Journal of Applied Mechanics, Vol. 34, December 1967.
11. Kobayashi, A. S. and Moss, W. L., "Stress Intensity Magnification Factors for Surface-Flawed Tension Plate and Notched Round Tension Bar," Fracture 1969, Chapman and Hall, London, 1969.

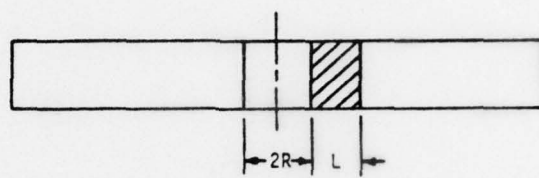
12. Shah, R. C., "Stress Intensity Factors for Through and Part-Through Cracks Originating at Fastener Holes," Eighth National Symposium on Fracture Mechanics, Brown University, August 1974.
13. Shah, R. C. and Kobayashi, A. S., "Stress Intensity Factors for an Elliptical Crack Approaching the Surface of a Semi-Infinite Solid," International Journal of Fracture, Vol. 9, No. 2, 1973.
14. Grandt, A. F., Jr., "Stress Intensity Factors for Some Thru-Cracked Fastener Holes," Seventh National Congress of Applied Mechanics, University of Colorado, June 1974.
15. Rice, J. R., "Some Remarks of Elastic Crack-Tip Stress Fields," International Journal of Solids and Structures, Vol. 8, No. 6, pp. 751-758, 1972.
16. Hall, L. R. and Finger, R. W., "Investigation of Flaw Geometry and Loading Effects on Plane Strain Fracture in Metallic Structures," Technical Report NASA-CR-72659, Boeing Company, December 1971.
17. Hall, L. R., Shah, R. C. and Engstrom, W. L., "Fracture and Fatigue Crack Growth Behavior of Surface Flaws and Flaws Originating at Fastener Holes," AFFDL-TR-74-47, Air Force Flight Dynamics Laboratory, 1974.
18. Jolles, M., McGowan, J. J. and Smith, C. W., "Stress Intensities for Cracks Emanating from Holes in Finite Thickness Plates," Technical Report VPI-E-75-15, Virginia Polytechnic Institute and State University, August 1975.
19. McGowan, J. J. and Smith, C. W., "Stress Intensity Factors for Deep Cracks Emanating from the Corner Formed by a Hole Intersecting a Plate Surface," Technical Report VPI-E-74-1, Virginia Polytechnic Institute and State University, January 1974.
20. Snow, J. R., "A Stress Intensity Factor Calibration for Corner Flaws at an Open Hole," Technical Report AFML-TR-74-282, Air Force Materials Laboratory, Wright-Patterson Air Force Base, Ohio, May 1975.
21. Grandt, A. F., Jr. and Hinnerichs, T. D., "Stress Intensity Factor Measurements for Flawed Fastener Holes," Army Symposium on Solid Mechanics, Cape Cod, Massachusetts, September 1974.
22. Shah, R. C. and Kobayashi, A. S., "Stress Intensity Factor for an Elliptical Crack Under Arbitrary Normal Loading," Journal of Engineering Fracture Mechanics, Vol. 3, No. 1, July 1971.

23. Sternberg, E. and Sadowsky, M. A., "Three-Dimensional Solution for the Stress Concentration Around a Circular Hole in a Plate of Arbitrary Thickness," *Journal of Applied Mechanics*, Vol. 16, No. 1, 1949, pp. 27-38.
24. Coker, E. G. and Filon, L. N. G., "Stress Distribution Due to a Load on a Pin or Rivet," in A Treatise on Photo-Elasticity, Cambridge, 1931.
25. Bickley, W. G., "The Distribution of Stress Round a Circular Hole in a Plate," *Philosophical Transactions of the Royal Society of London*, Series A, Vol. 227, 1928, pp. 383-415.
26. Knight, R. C., "The Action of a Rivet in a Plate of Finite Breadth," *Philosophical Magazine and Journal of Science*, Series 7, Vol. 19, No. 127, March 1935, pp. 517-540.
27. Howland, R. C. J. and Stevenson, A. C., "Bi-Harmonic Analysis in a Perforated Strip," *Royal Society of London, Philosophical Transactions*, Series A, Vol. 232, 1933, pp. 155-222.
28. Theocaris, P. S., "The Stress Distribution in a Strip Loaded in Tension by Means of a Central Pin," *Journal of Applied Mechanics*, Vol. 23, No. 1, 1956.
29. Gregory, R. D., "Stress Concentration Around a Loaded Bolt in an Axially Loaded Bar," *Cambridge Philosophical Society Proceedings*, Vol. 64, Part 4, October 1968, pp. 1215-1236.
30. Frocht, M. M. and Hill, H. N., "Stress-Concentration Factors Around a Central Circular Hole in a Plate Loaded Through Pin in the Hole," *Journal of Applied Mechanics*, Vol. 62, March 1940, pp. A5-A9.
31. Jessop, H. T., Snell, C. and Hollister, G. S., "Photoelastic Investigation on Plates with Single Interference-Fit Pins with Load Applied (a) to Pin only and (b) to Pin and Plate Simultaneously," *The Aeronautical Quarterly*, Vol. 9, 1958, pp. 147-163.
32. Cox, H. L. and Brown, A. F. C., "Stresses Round Pins in Holes," *The Aeronautical Quarterly*, Vol. 15, 1964, pp. 357-372.
33. Harris, H. G., Ojalvo, I. U. and Hooson, R. E., "Stress and Deflection Analysis of Mechanically Fastened Joints," Technical Report AFFDL-TR-70-49, Air Force Flight Dynamics Laboratory, Wright-Patterson Air Force Base, Ohio, May 1970.
34. Mohaghegh, M., "Biaxial Stress Analysis of a Plate with a Fastener," Boeing Document No. D6-24757TN, The Boeing Company, Renton, Washington, 1971.

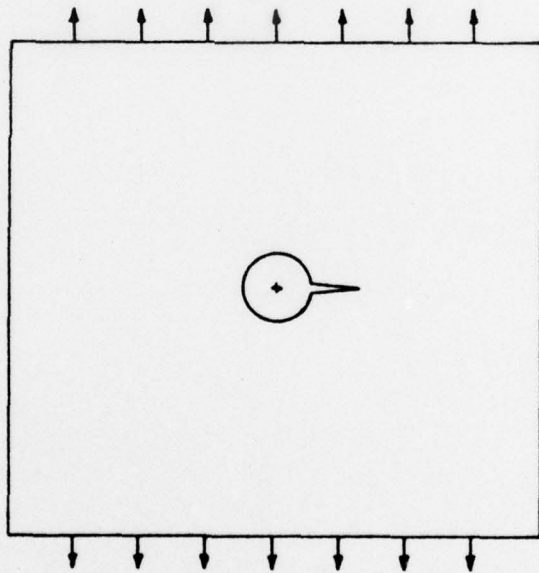
35. Brombolich, L. J., "Elastic-Plastic Analysis of Stresses Near Fastener Holes," Eleventh Aerospace Sciences Meeting of the American Institute of Aeronautics and Astronautics, Washington, D. C., January 1973.
36. Kantorovich, L. V. and Krylov, V. I., Approximate Methods of Higher Analysis, translated by C. D. Berster. New York, Interscience Publishers, Inc., 1958.
37. Smith, F. W. and Alavi, M. J., "Stress Intensity Factors for a Part-Circular Surface Flaw," Proceedings of the First International Conference on Pressure Vessel Technology, Delft, Holland, 1969.
38. Thresher, R. W. and Smith, F. W., "Stress Intensity Factors for a Surface Crack in a Finite Solid," Journal of Applied Mechanics, Vol. 39, No. 1, March 1972.
39. Smith, F. W. and Sorensen, D. R., "Mixed Mode Stress Intensity Factors for Semielliptical Surface Cracks," Technical Report No. 5, NASA Grant NGL-06-002-063, Colorado State University, June 1974.
40. Wilson, E. L., "Finite Element Analysis of Mine Structures," Technical Report Bureau of Mines OFR27-73, Denver Mining Research Center, Contract No. H0110231, September 1972.
41. Green, A. E. and Sneddon, I. N., "The Distribution of Stress in the Neighborhood of a Flat Elliptical Crack in an Elastic Solid," Proceedings of the Cambridge Philosophical Society, Vol. 46, 1950.
42. Kobayashi, A. S., "Stress Intensity Factor of a Corner Crack," Interim Technical Report No. 3, United States Army Research Office, Durham, Grant No. DA-ARO-D-31-124-73-G38, August 1974.
43. Hartranft, R. J. and Sih, G. C., "Alternating Methods Applied to Edge and Surface Crack Problems," Technical Report NASA-RT-72-1, April 1972.
44. Sih, G. C., Mechanics of Fracture I, Noordhoff International Publishing, Leyden, the Netherlands, 1973.
45. Smith, F. W., "Stress Near a Semi-Circular Edge Crack," Ph.D. Thesis, University of Washington, 1966.
46. Smith, F. W., "Stress Intensity Factors for a Surface Flawed Fracture Specimen," Technical Report No. 1, NASA Grant MGR-06-002-063, Colorado State University, September 1971.

47. Cartwright, D. J. and Ratcliffe, G. A., "Strain Energy Release Rate for Radial Cracks Emanating from a Pin Loaded Hole," International Journal of Fracture Mechanics, Vol. 8, No. 2, June 1972.
48. Savin, G. N., Stress Concentrations Around Holes, Pergamon Press, New York, 1961.
49. McEvily, A. J., Boettner, R. C. and Johnston, R. L., "On the Formation and Growth of Fatigue Cracks in Polymers," in Fatigue - An Interdisciplinary Approach, Proceedings of the 10th Sagamore Army Materials Research Conference, Syracuse University Press, 1964.
50. Larson, L. J., "Depth Effect for Semi-Elliptical Surface Flaws," Master's Thesis, Colorado State University, August 1968.
51. Grandt, A. F., Jr. and Sinclair, G. M., "Stress Intensity Factors for Surface Cracks in Bending," in Stress Analysis and Growth of Cracks, ASTM Special Technical Publication 513, 1969.
52. Jones, M. and Brown, W. F., "The Influence of Crack Length and Thickness in Plane Strain Fracture Toughness Tests," in Review of Developments in Plane Strain Fracture Toughness Testing, ASTM Special Technical Publication 463, 1970.
53. Smith, F. W., and Brown, R. A., "Fracture Testing of Penetrated Surface Flaws," Technical Report No. 2, NASA Grant NGL-06-002-063, September 1972.
54. Brown, W. F., Jr. and Srawley, J. E., Plane Strain Crack Toughness Testing of High Strength Metallic Materials, ASTM Special Technical Publication 410, 1966.
55. Pitoniak, F. J., "Experimental Study of Fatigue Crack Propagation and Retardation Using Polymethylmethacrylate," Technical Report AFFDL-TR-72-235, Air Force Flight Dynamics Laboratory, Wright-Patterson Air Force Base, Ohio, November 1972.
56. Brown, W. F., Jr. and Srawley, J. E., "Fracture Toughness Testing Methods," in Fracture Toughness Testing and Its Application, ASTM Special Technical Publication 381, 1965.
57. Irwin, G. R., "Fracture Testing of High Strength Sheet Materials Under Conditions Appropriate for Stress Analysis," Report 5486, United States Naval Research Laboratory, July 1960.
58. Irwin, G. R., "Crack-Extension Force for a Part-Through Crack in a Plate," Journal of Applied Mechanics, Vol. 33, No. 4, December 1966.

59. Theocaris, P. S., "Local Yielding Around a Crack Tip in Plexiglas," American Society of Mechanical Engineers, Paper 70-APM-BB.
60. Segedin, C. M., "Some Three-Dimensional Mixed Boundary Value Problems in Elasticity," Report, Department of Aeronautics and Astronautics, University of Washington, Seattle, Washington, June 1967.

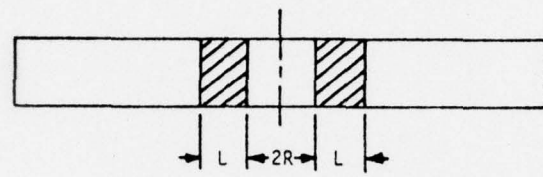


Top View

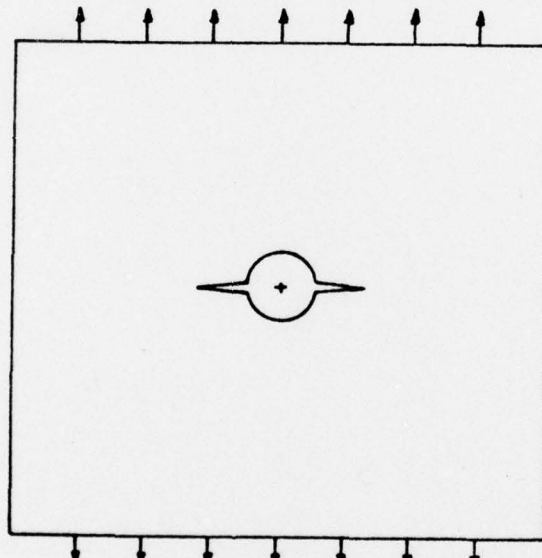


Front View

Figure 1.1 A Single Through-Crack Emanating From a Hole in a Plate



Top View



Front View

Figure 1.2 Double Through-Cracks Emanating From a Hole in a Plate

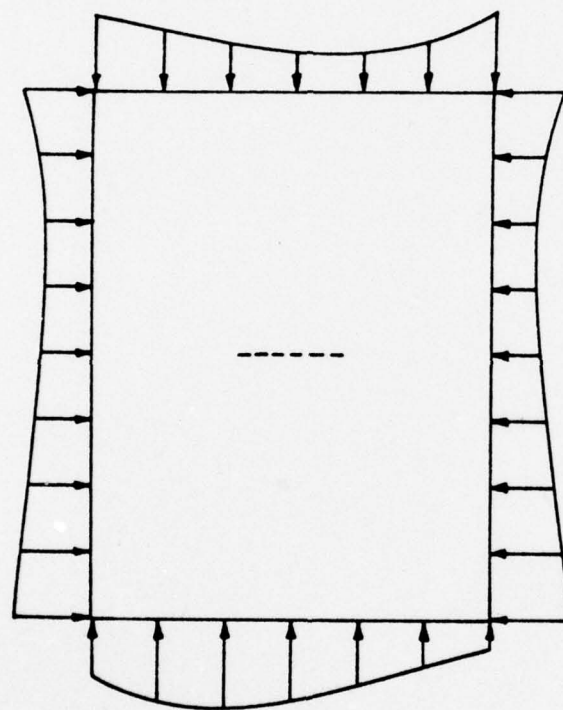
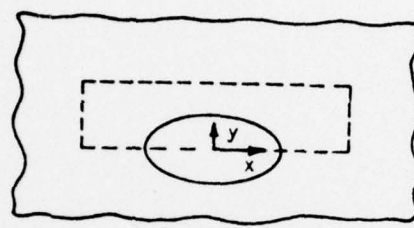
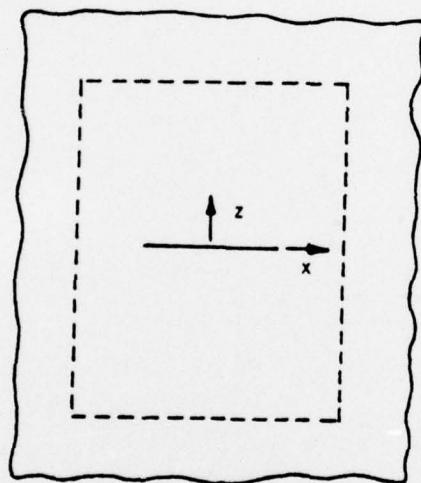


Figure 1.3 A Finite Body Without a Crack, Subject to Surface Traction

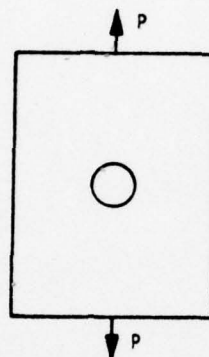


Top View



Front View

Figure 1.4 An Elliptical Crack in an Infinite Solid



(a) Open Hole

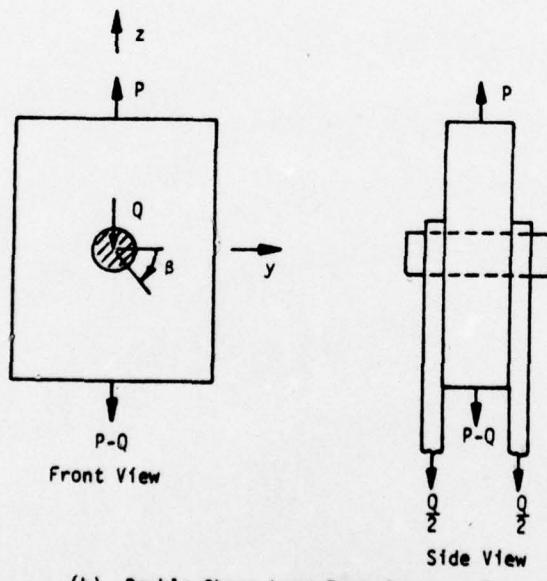
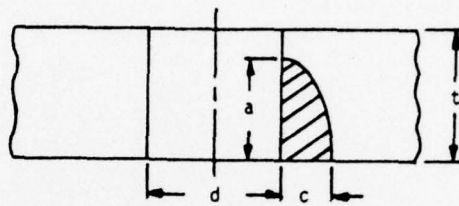
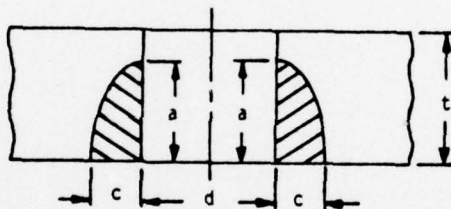


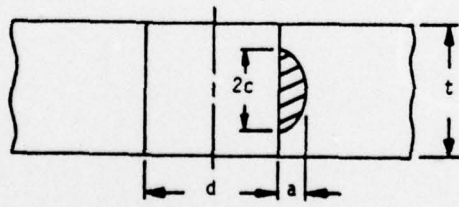
Figure 1.5 Plate Loading Conditions



(a) Single quarter-elliptical corner crack



(b) Double quarter-elliptical corner cracks



(c) Single semi-elliptical embedded crack

Figure 2.1 Crack Types and Locations Relative to a Fastener Hole

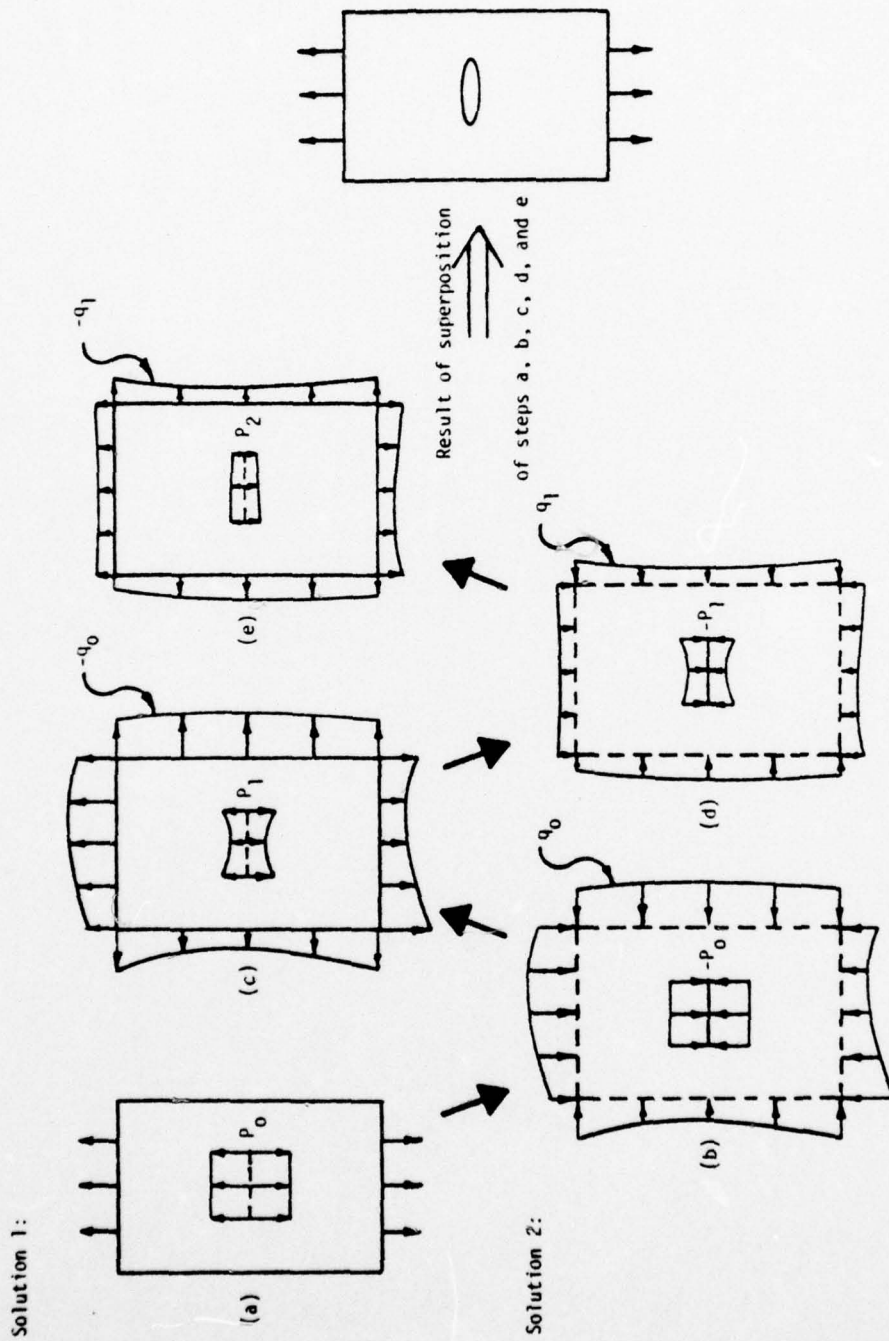


Figure 2.2 Finite Element-Alternating Method, Two Iterations

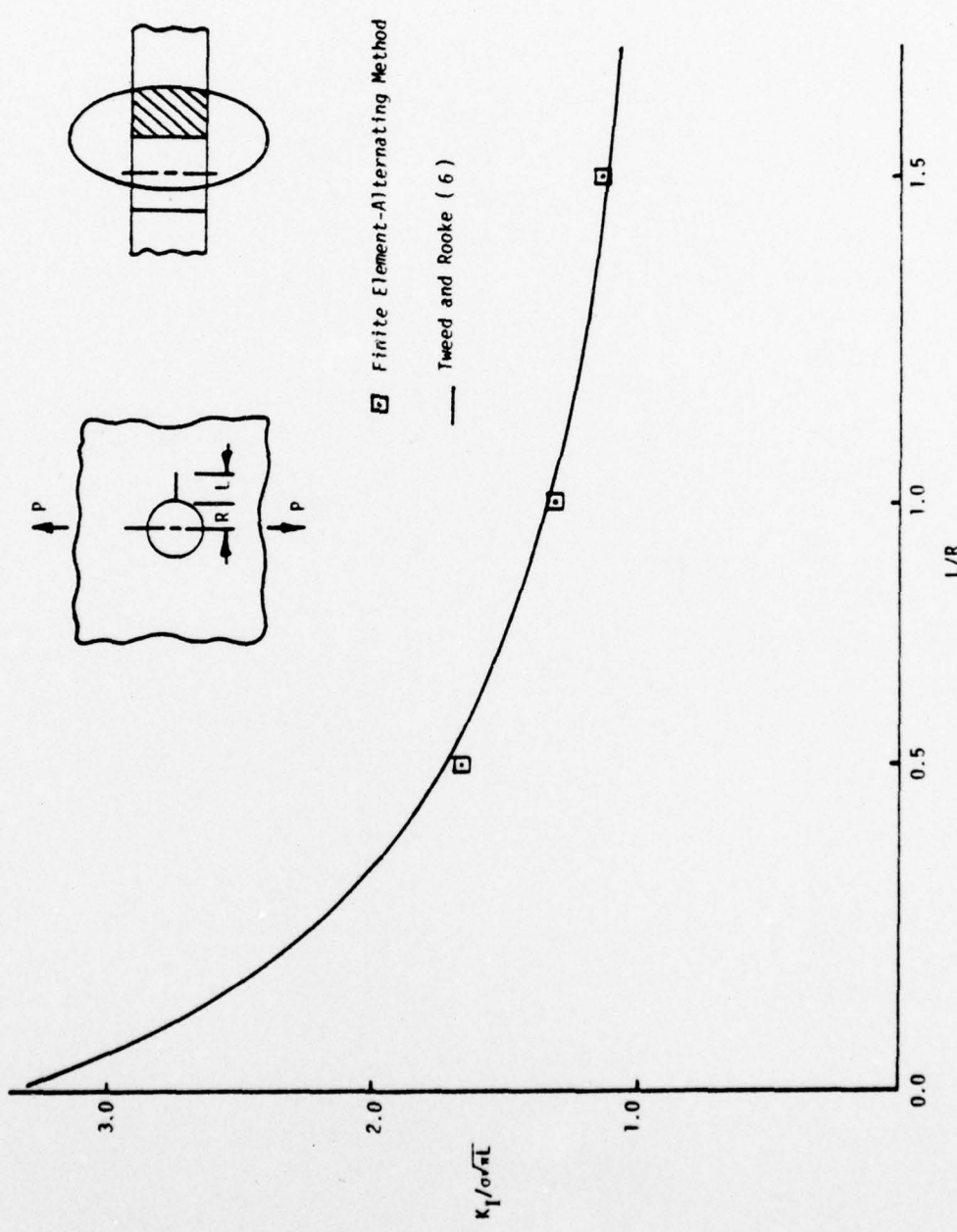


Figure 2.3 Three-Dimensional Approximation of a Two-Dimensional Problem

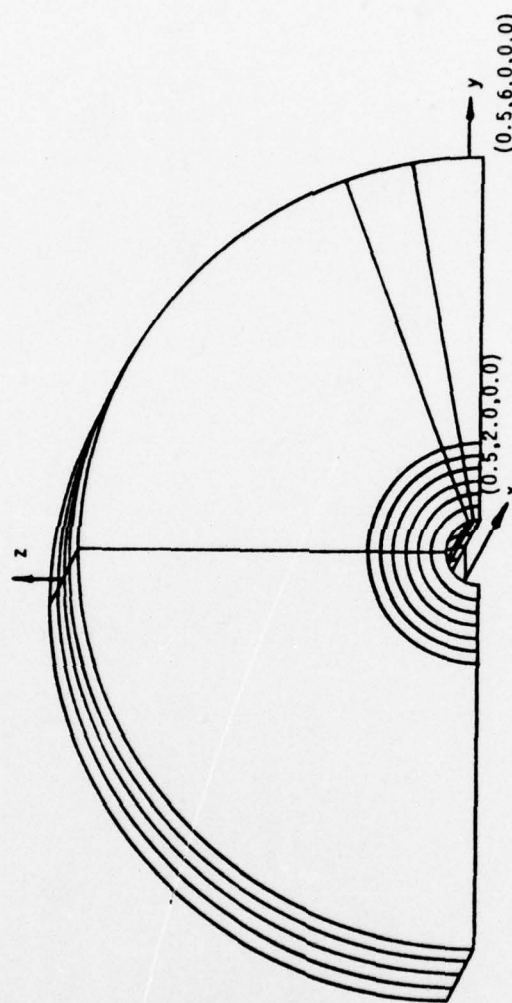


Figure 2.4 112-Element Finite Element Mesh  
Single Corner Crack Problem,  $d/t=1.0$

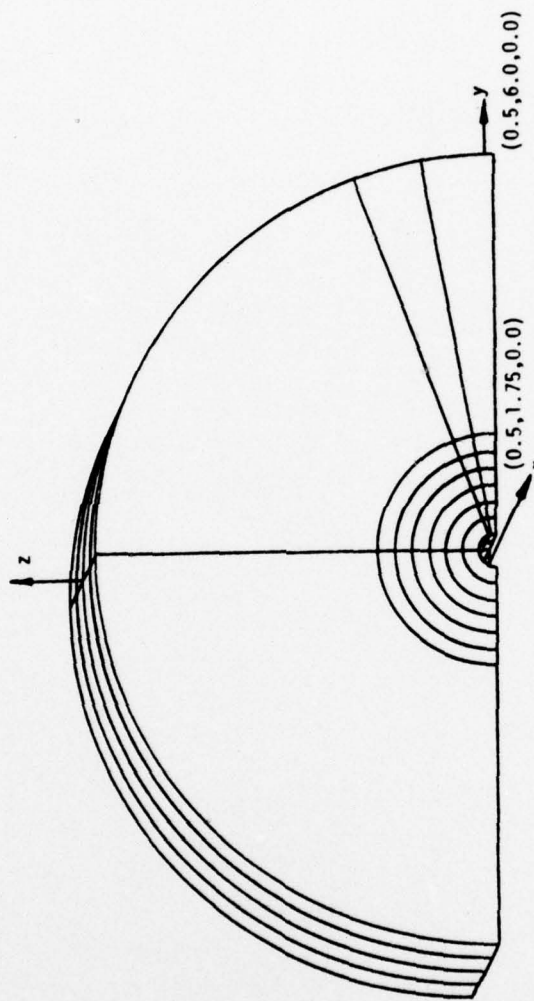


Figure 2.5  
112-Element Finite Element Mesh,  
Single Corner Crack Problem,  $d/t=0.5$

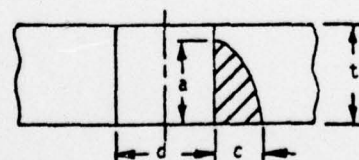
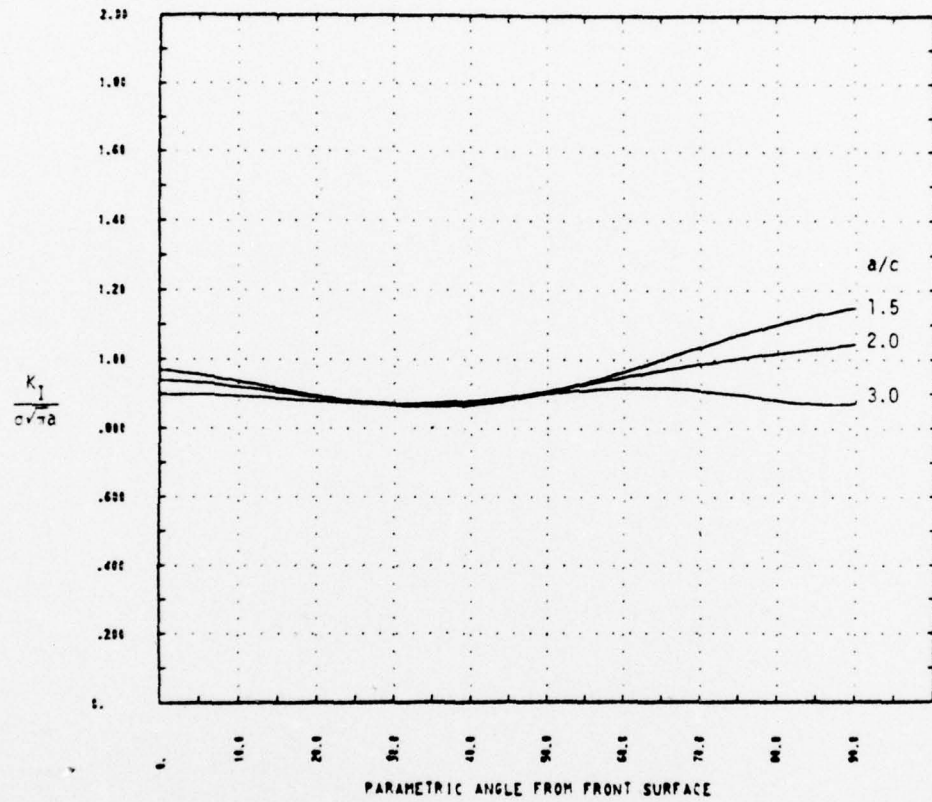


Figure 2.6 Magnification Factor Versus Angle from Front Surface  
 Single Corner Cracks  
 $a/t=0.9$ ,  $d/t=1.0$ ,  $Q/P=0.0$

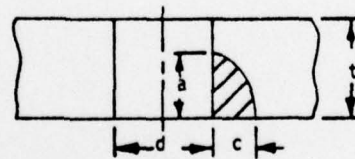
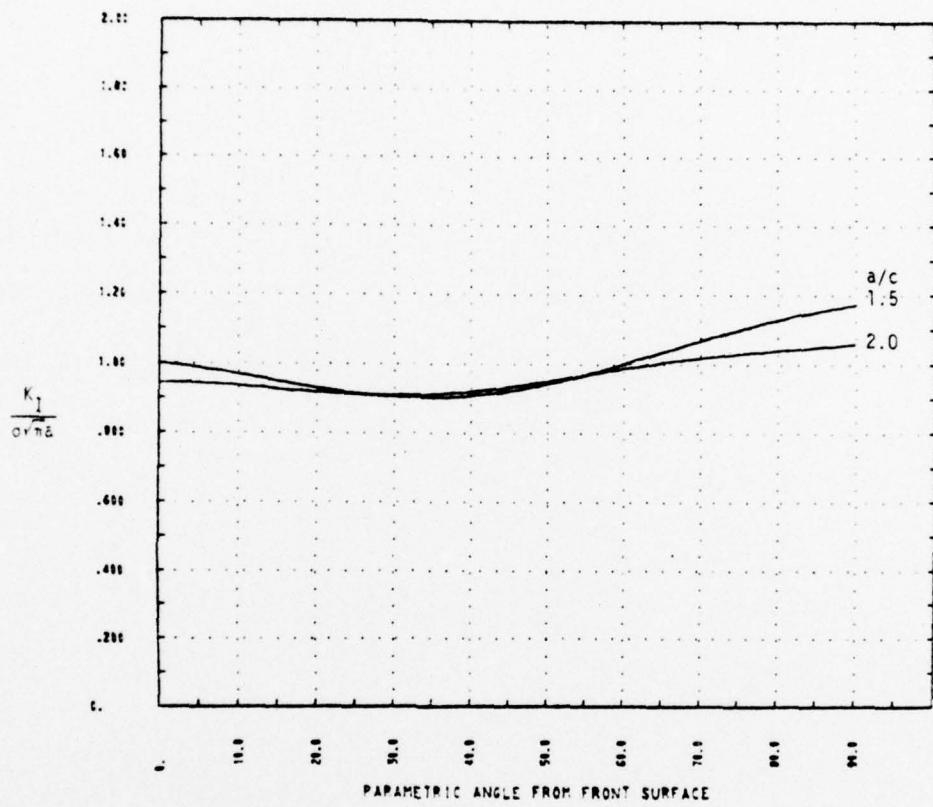


Figure 2.7 Magnification Factor Versus Angle from Front Surface  
 Single Corner Cracks  
 $a/t=0.75$ ,  $d/t=1.0$ ,  $Q/P=0.0$

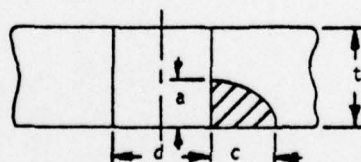
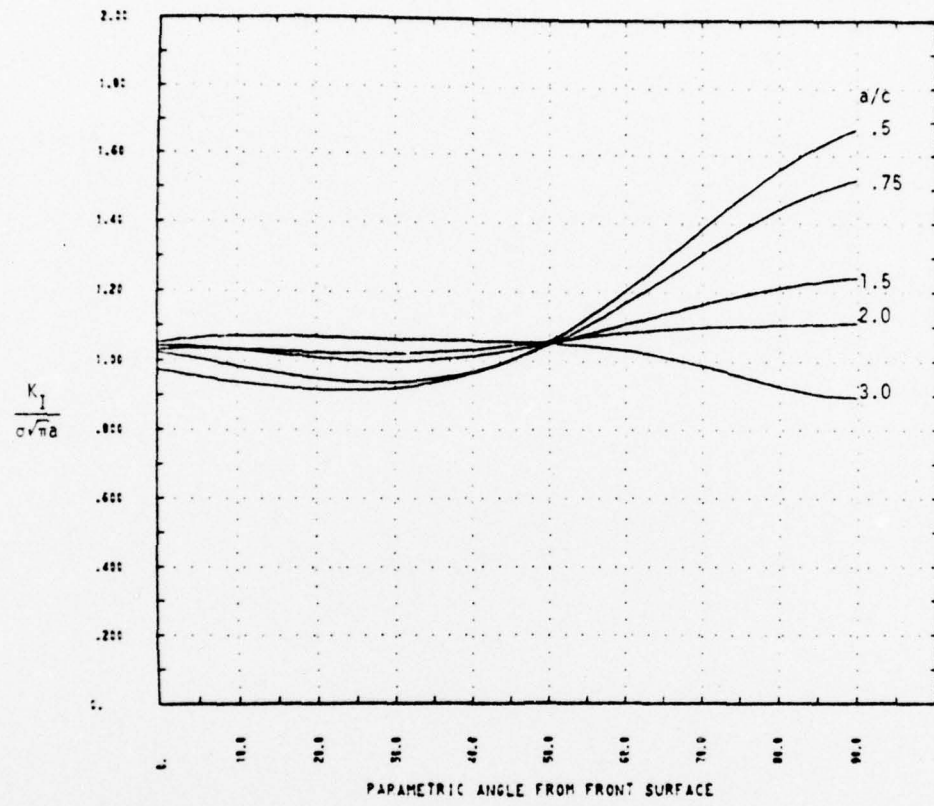


Figure 2.8 Magnification Factor Versus Angle from Front Surface  
 Single Corner Cracks  
 $a/t=0.5$ ,  $d/t=1.0$ ,  $Q/P=0.0$

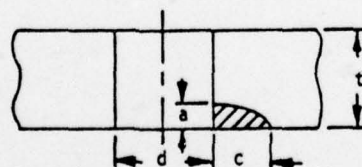
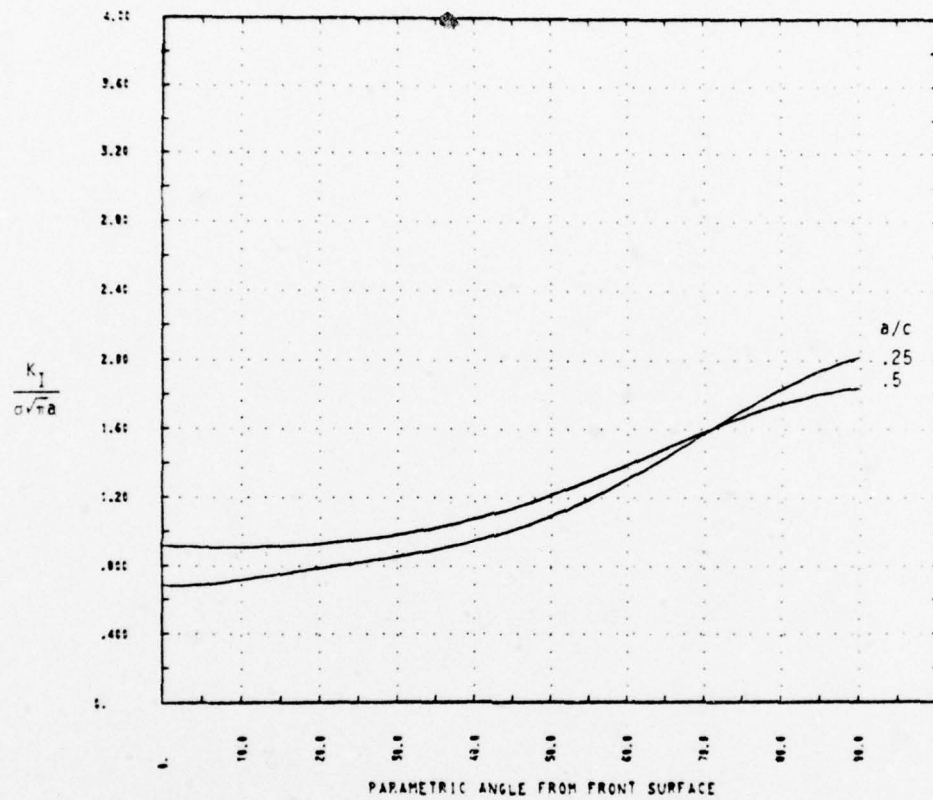


Figure 2.9 Magnification Factor Versus Angle from Front Surface  
 Single Corner Cracks  
 $a/t=0.25$ ,  $d/t=1.0$ ,  $Q/P=0.0$

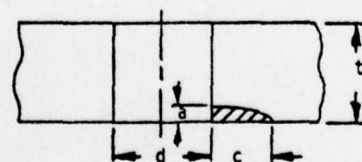
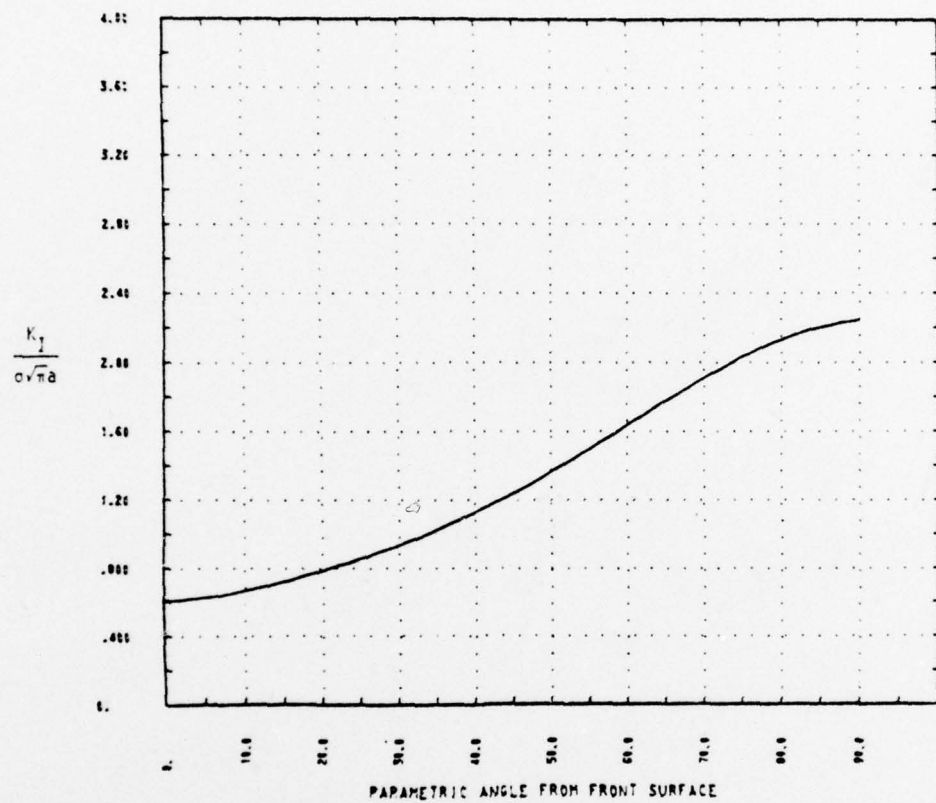


Figure 2.10 Magnification Factor Versus Angle from Front Surface  
 Single Corner Crack  
 $a/c=0.25$ ,  $a/t=0.125$ ,  $d/t=1.0$ ,  $Q/P=0.0$

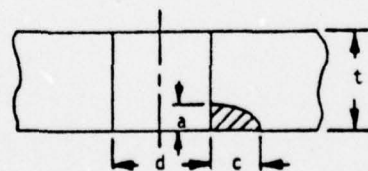
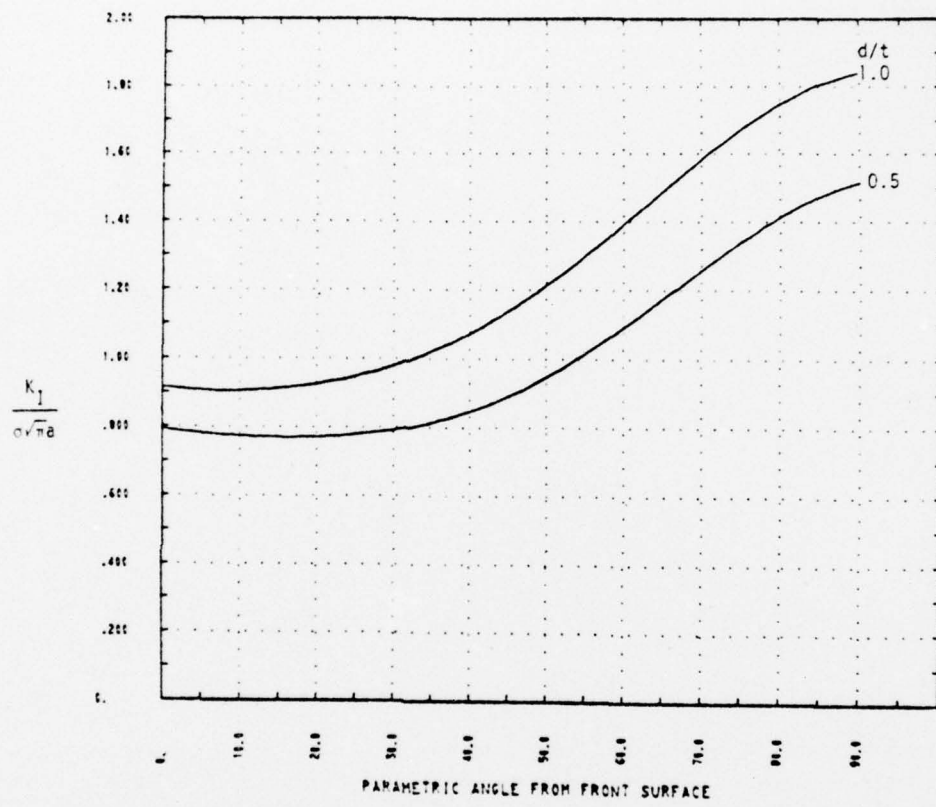


Figure 2.11 Magnification Factor Versus Angle from Front Surface  
 Single Corner Cracks  
 $a/c=0.50$ ,  $a/t=0.25$ ,  $Q/P=0.0$

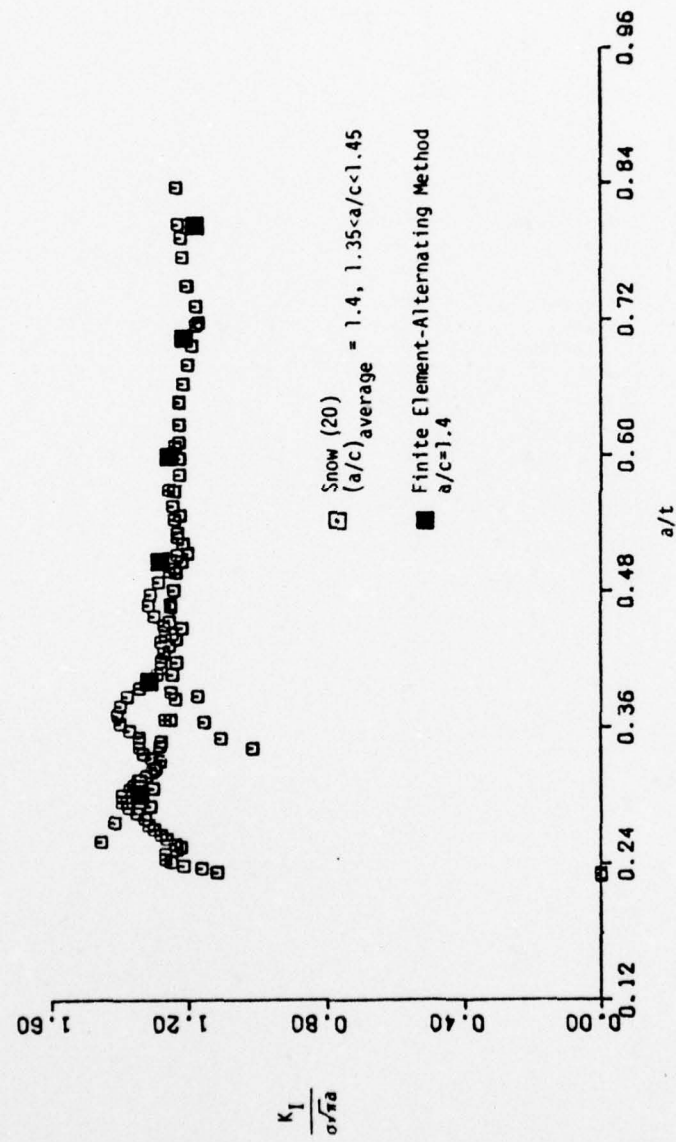


Figure 2.12 Comparison of Magnification Factors at the Hole, Single Corner Crack, Open Hole

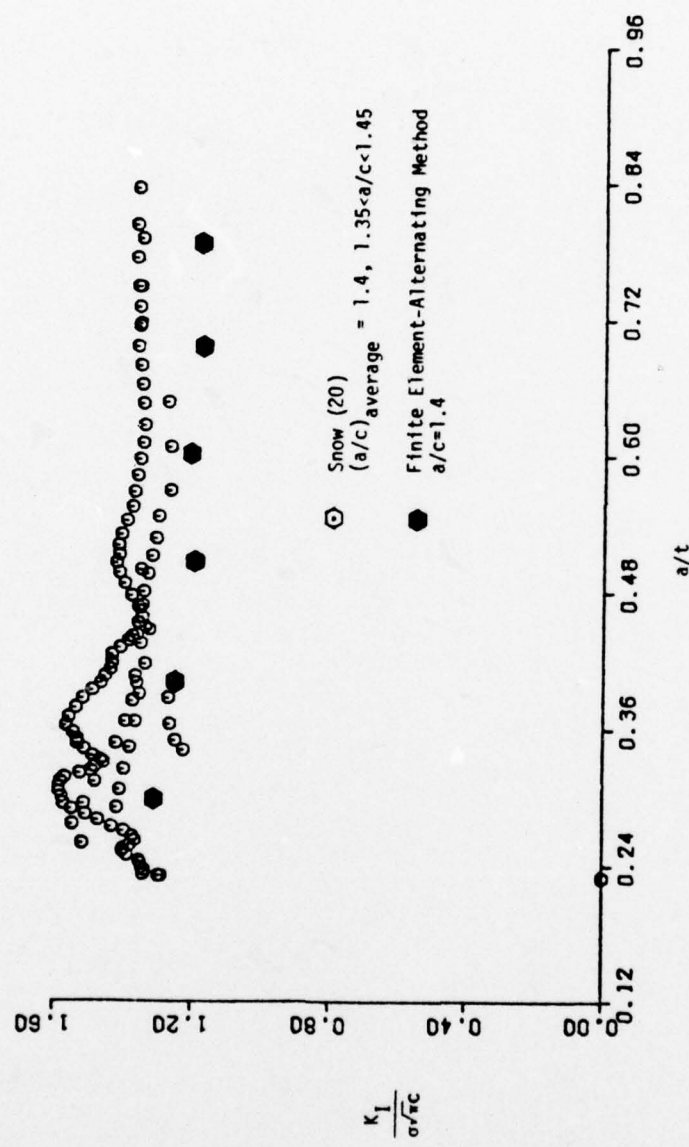


Figure 2.13 Comparison of Magnification Factors at the Front Surface, Single Corner Crack, Open Hole

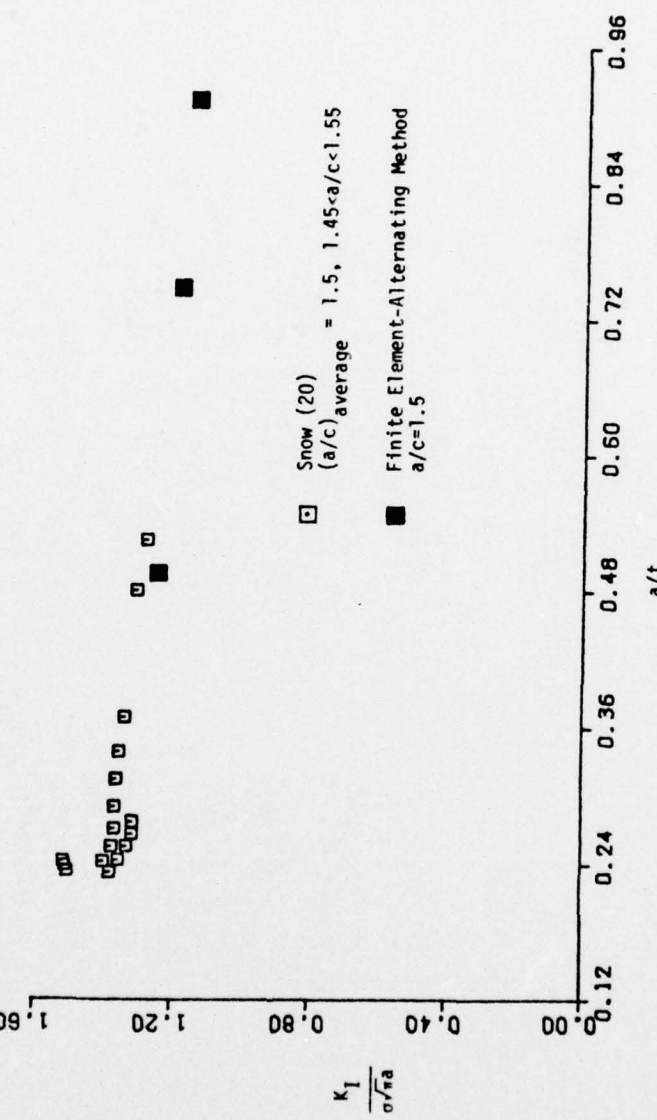


Figure 2.14 Comparison of Magnification Factors at the Hole, Single Corner Crack, Open Hole

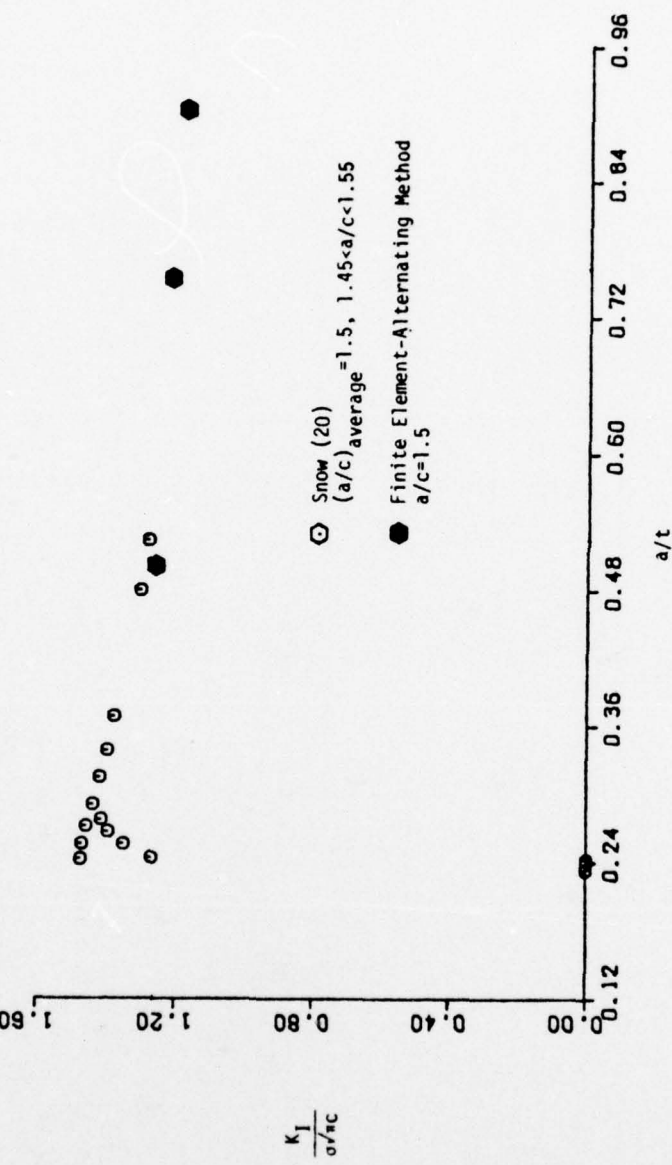


Figure 2.15 Comparison of Magnification Factors at the Front Surface, Single Corner Crack, Open Hole

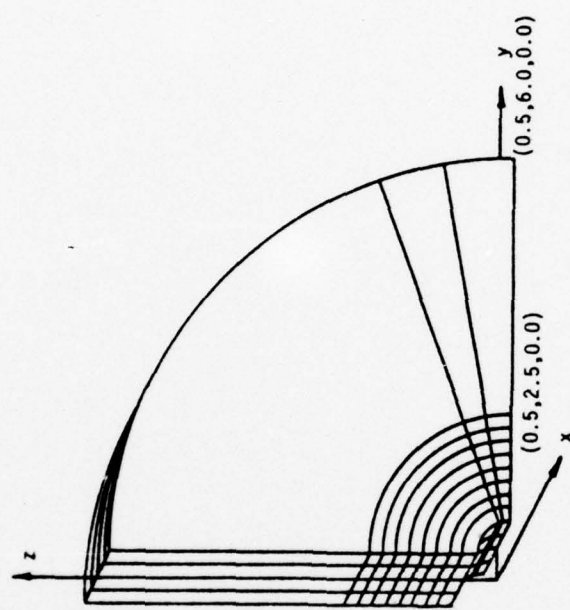


Figure 3.1 108-Element Finite Element Mesh, Double Corner Crack Problem,  $d/t = 1.0$

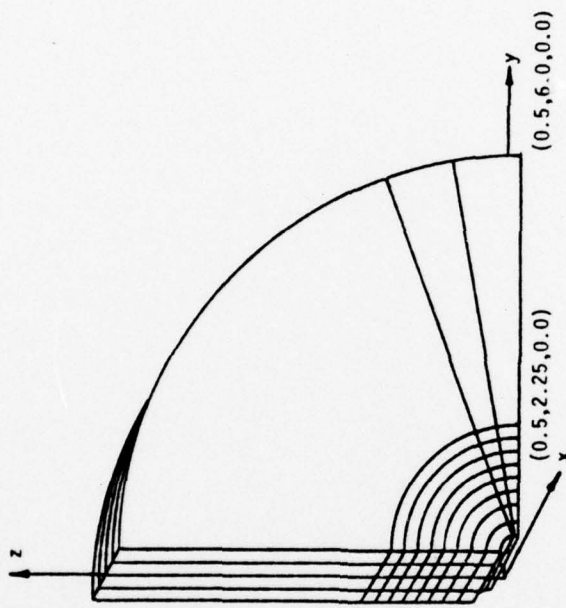


Figure 3.2 108-Element Finite Element Mesh, Double Corner Crack Problem,  $d/t = 0.5$

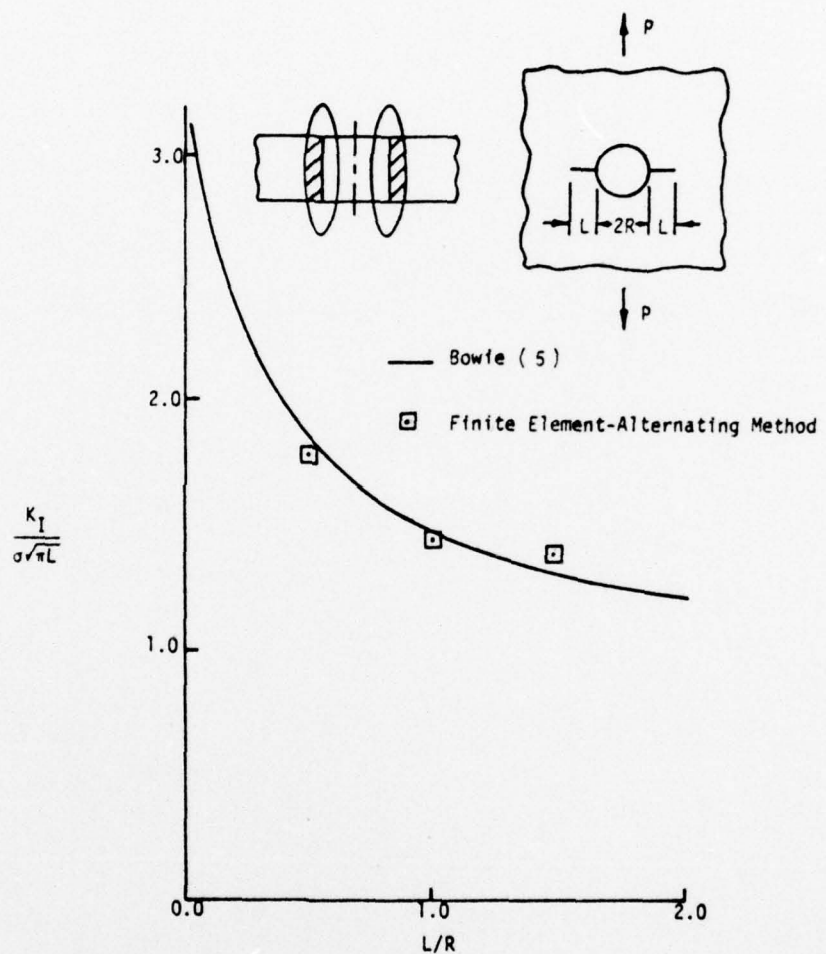


Figure 3.3 Three-Dimensional Approximation of a Two-Dimensional Problem

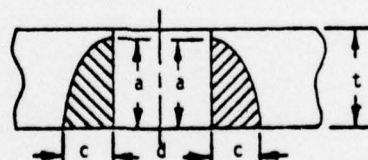
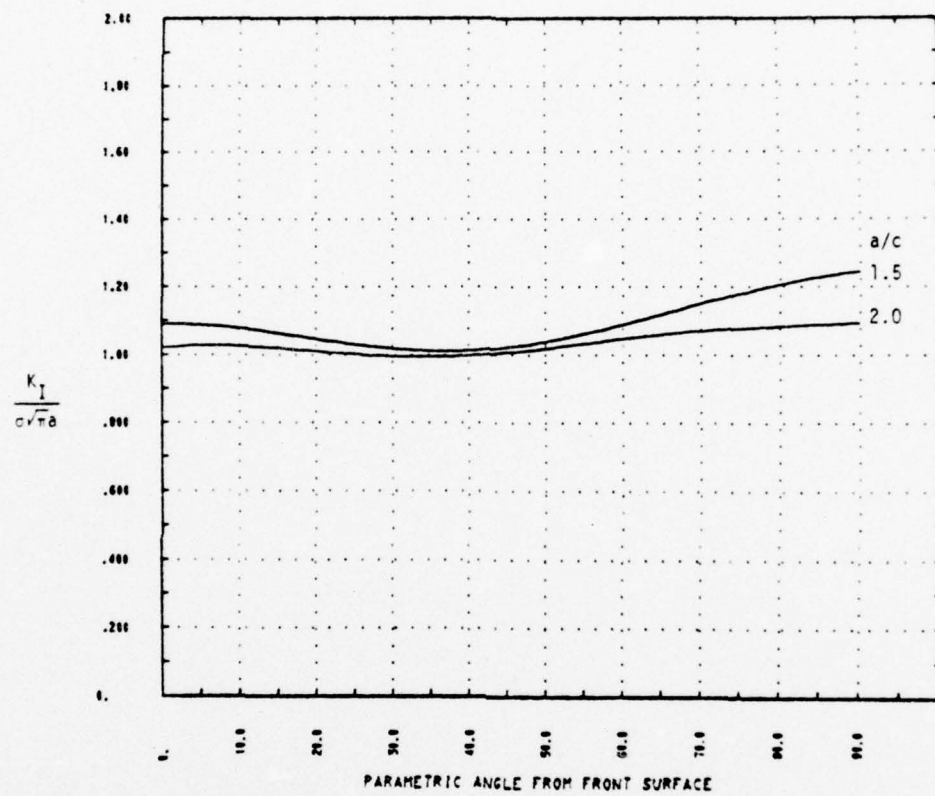


Figure 3.4 Magnification Factor Versus Angle from Front Surface  
Double Corner Cracks  
 $a/t=0.9$ ,  $d/t=1.0$ ,  $Q/P=0.0$

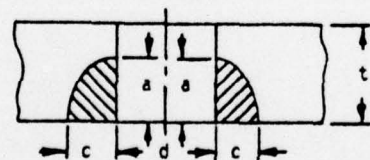
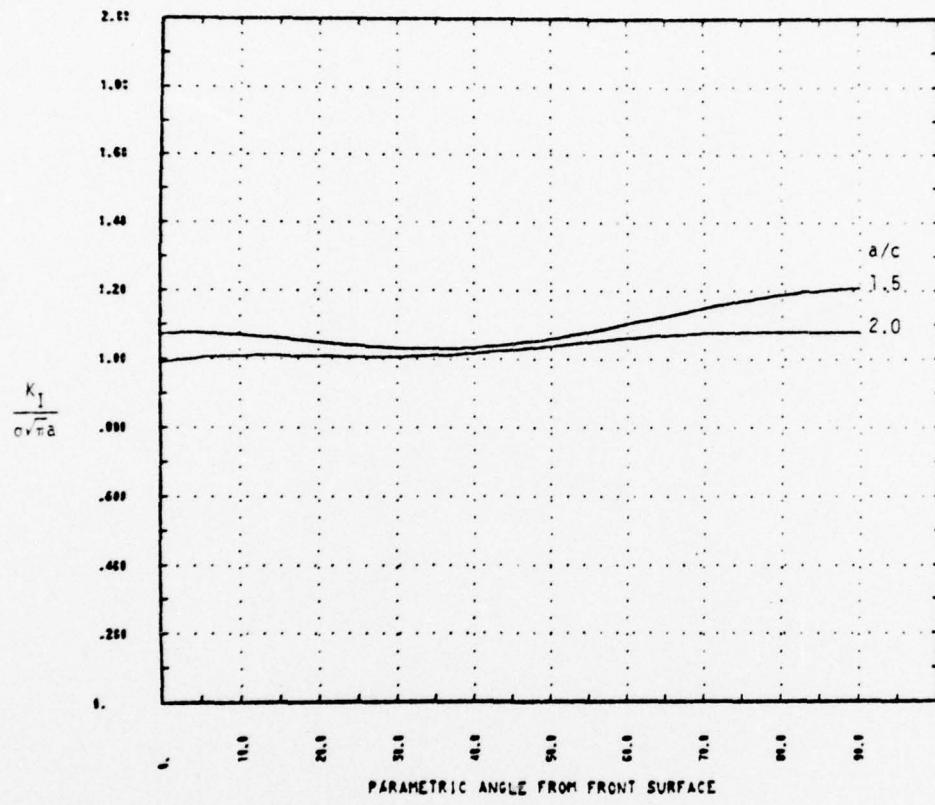


Figure 3.5 Magnification Factor Versus Angle from Front Surface  
Double Corner Cracks  
 $a/t=0.75$ ,  $d/t=1.0$ ,  $Q/P=0.0$

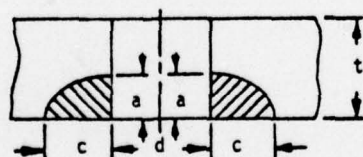
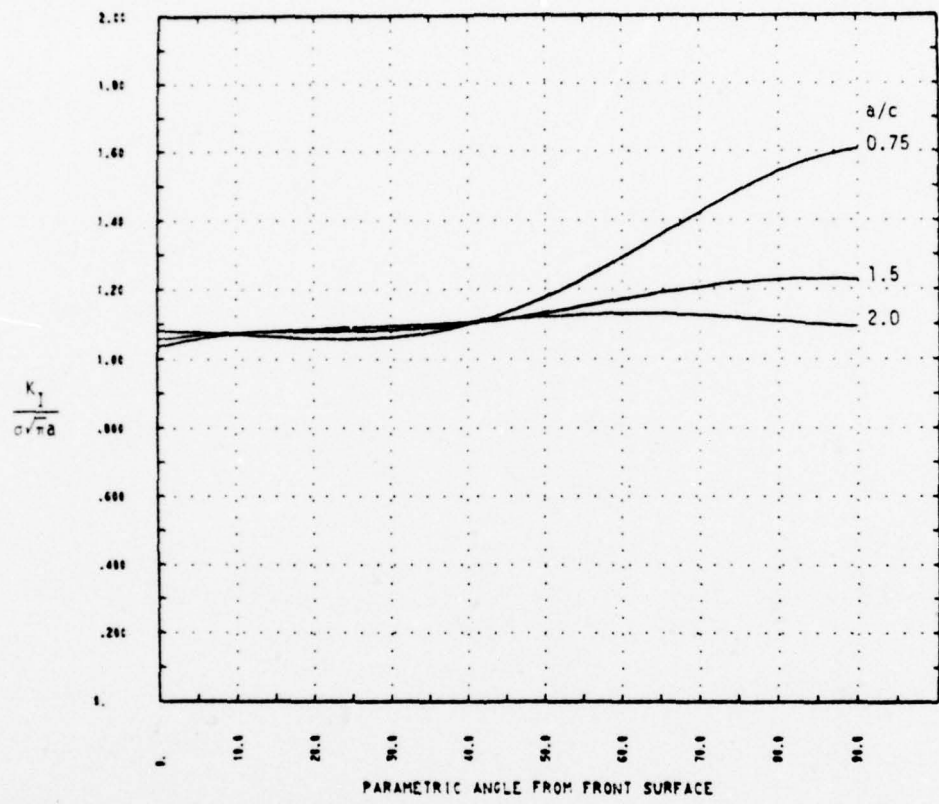


Figure 3.6 Magnification Factor Versus Angle from Front Surface  
 Double Corner Cracks  
 $a/t=0.5$ ,  $d/t=1.0$ ,  $Q/P=0.0$

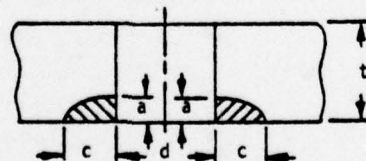
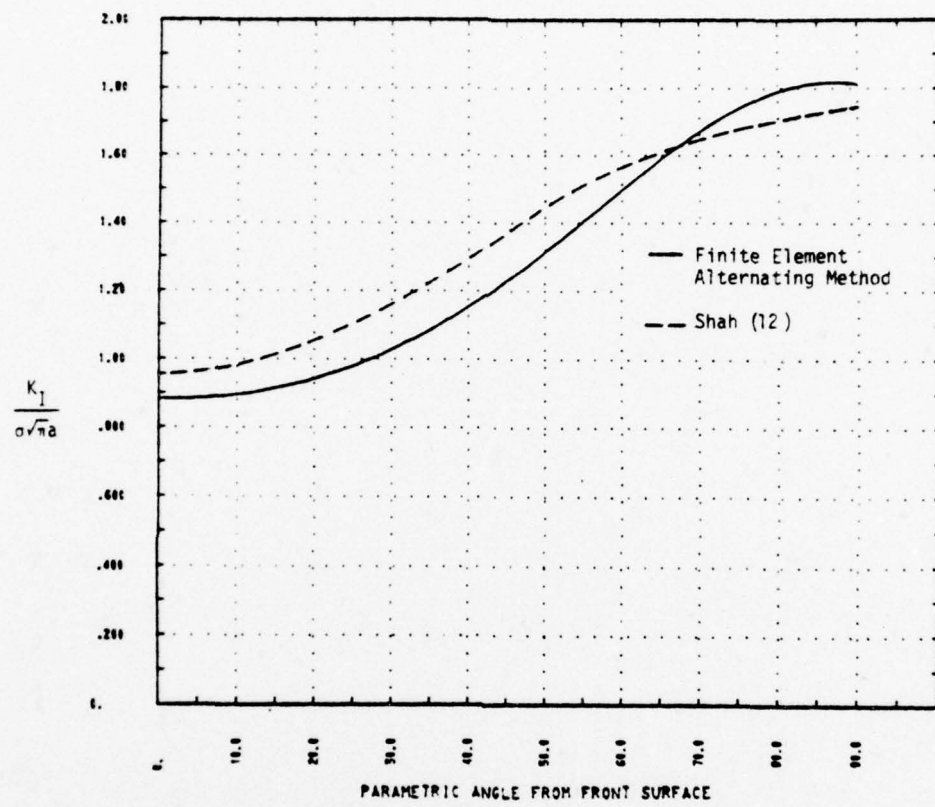


Figure 3.7 Magnification Factor Versus Angle from Front Surface  
Double Corner Cracks  
 $a/c=0.50$ ,  $a/t=0.25$ ,  $d/t=1.0$ ,  $Q/P=0.0$

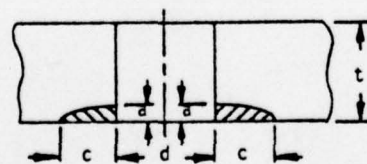
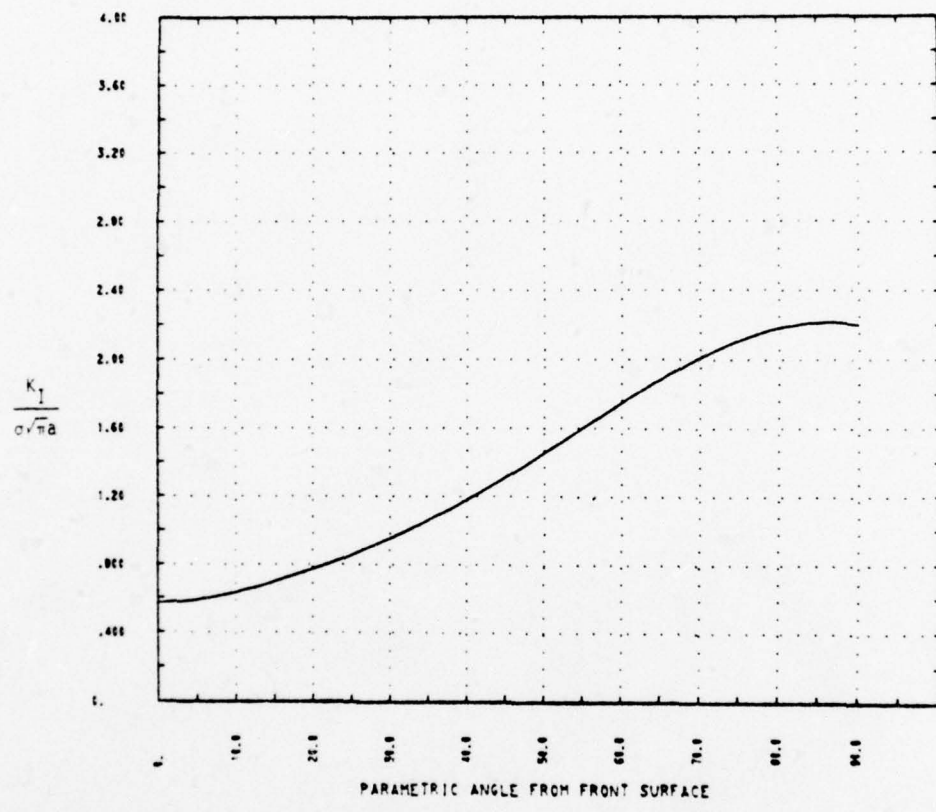


Figure 3.8 Magnification Factor Versus Angle from Front Surface  
Double Corner Crack  
 $a/c=0.25$ ,  $a/t=0.125$ ,  $d/t=1.0$ ,  $Q/P=0.0$

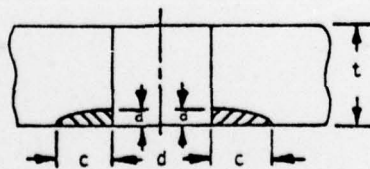
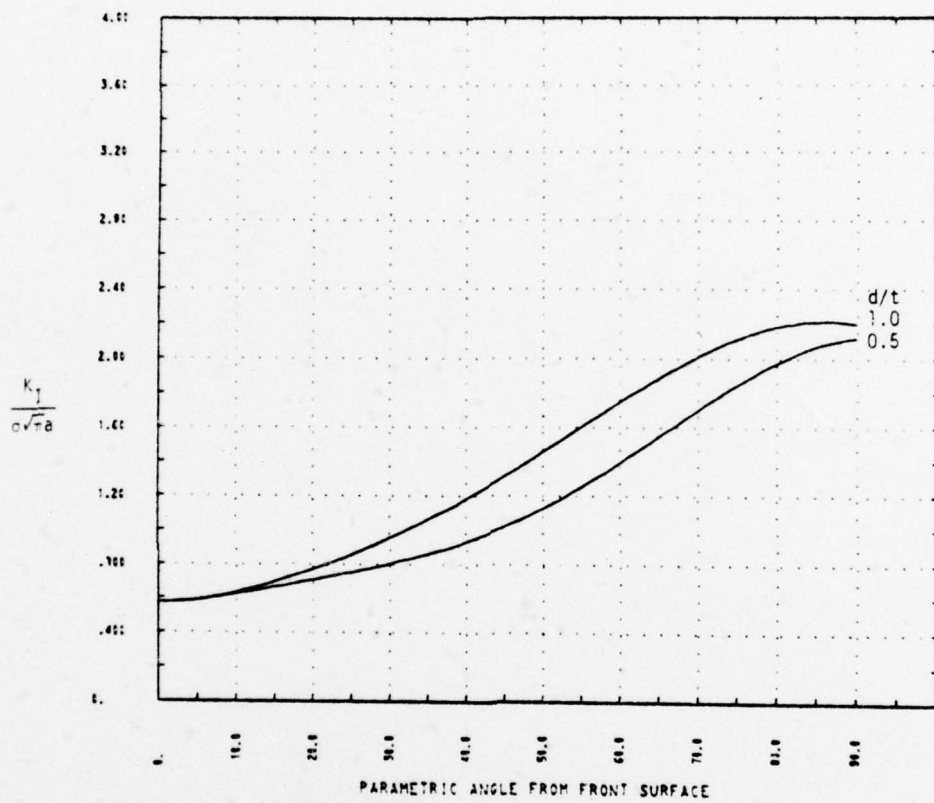


Figure 3.9 Magnification Factor Versus Angle from Front Surface  
Double Corner Cracks  
 $a/c=0.25$ ,  $a/t=0.125$ ,  $Q/P=0.0$

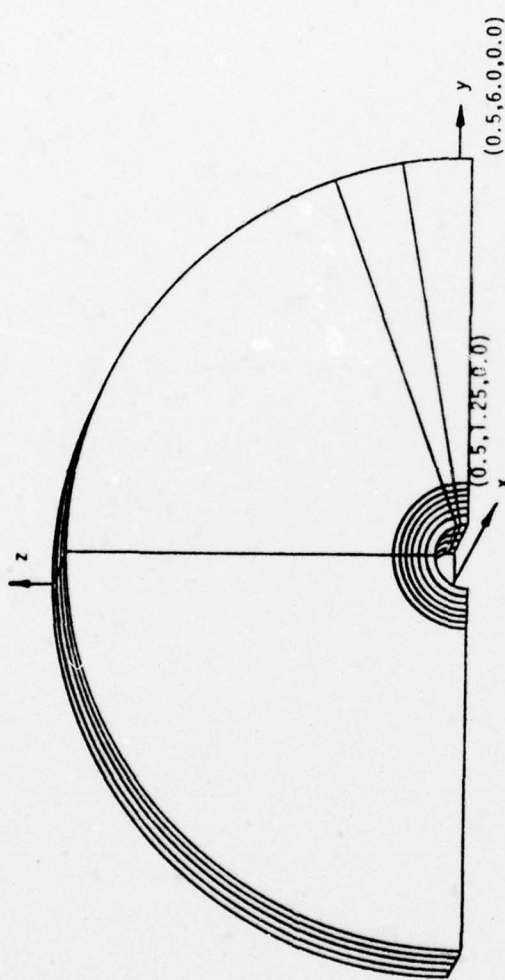


Figure 4.1 112-Element Finite Element Mesh  
Embedded Crack Problem,  $d/t=1.0$

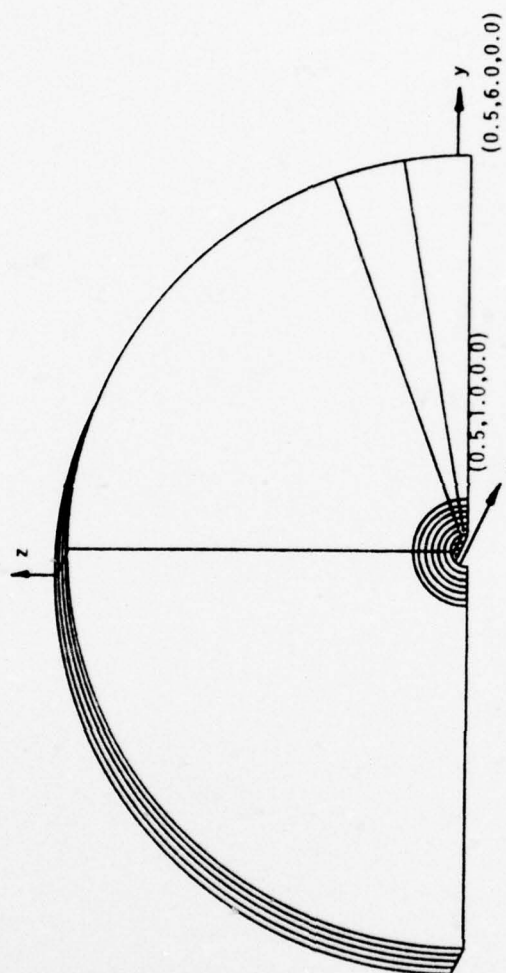


Figure 4.2  
112 Element Finite Element Mesh  
Embedded Crack Problem,  $d/t=0.5$

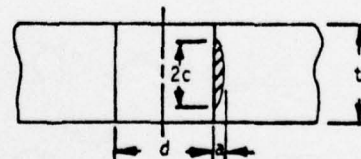
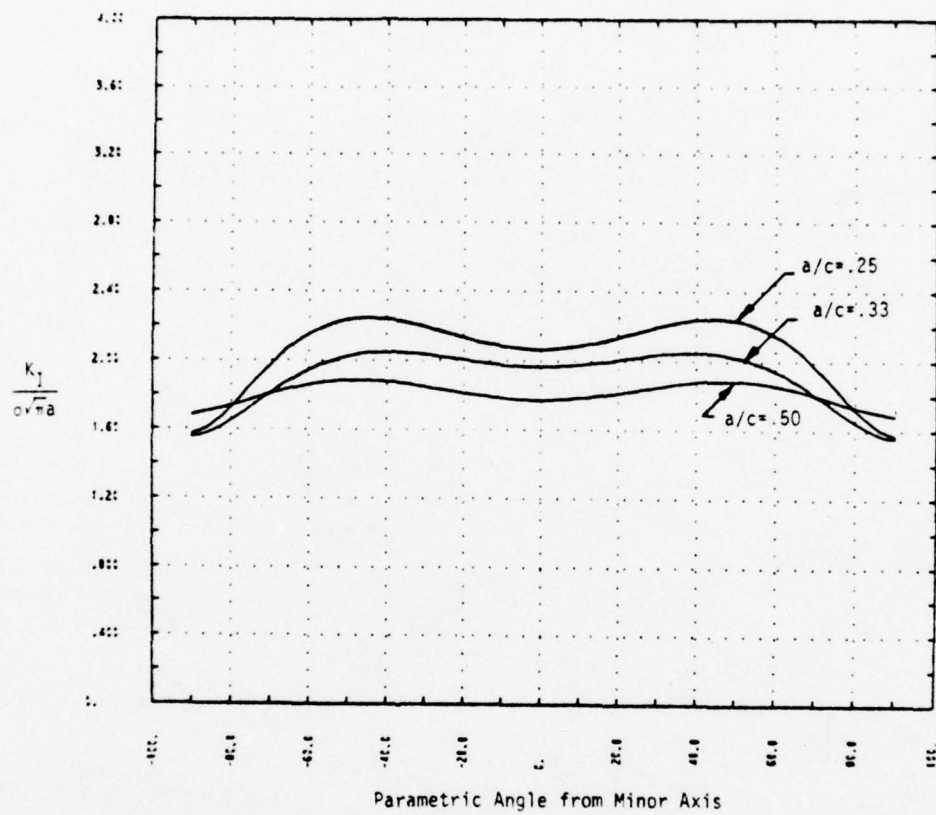
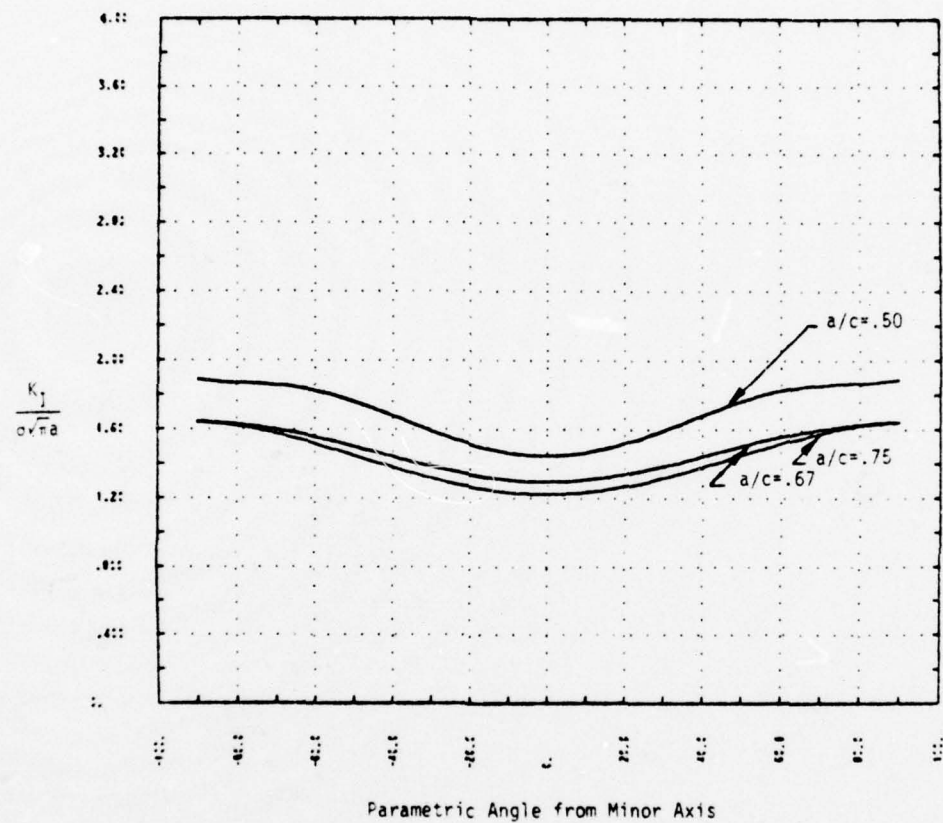


Figure 4.3 Magnification Factor Versus Angle from Minor Axis  
Embedded Cracks  
 $a/t=0.125$ ,  $d/t=1.0$ ,  $Q/P=0.0$



Parametric Angle from Minor Axis

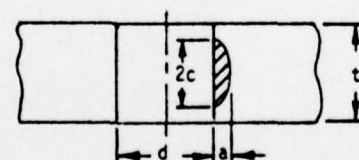


Figure 4.4 Magnification Factor Versus Angle from Minor Axis  
Embedded Cracks  
 $a/t = 0.25$ ,  $d/t = 1.0$ ,  $Q/P = 0.0$

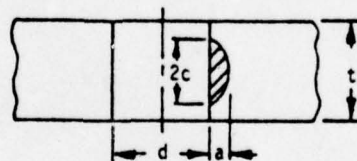
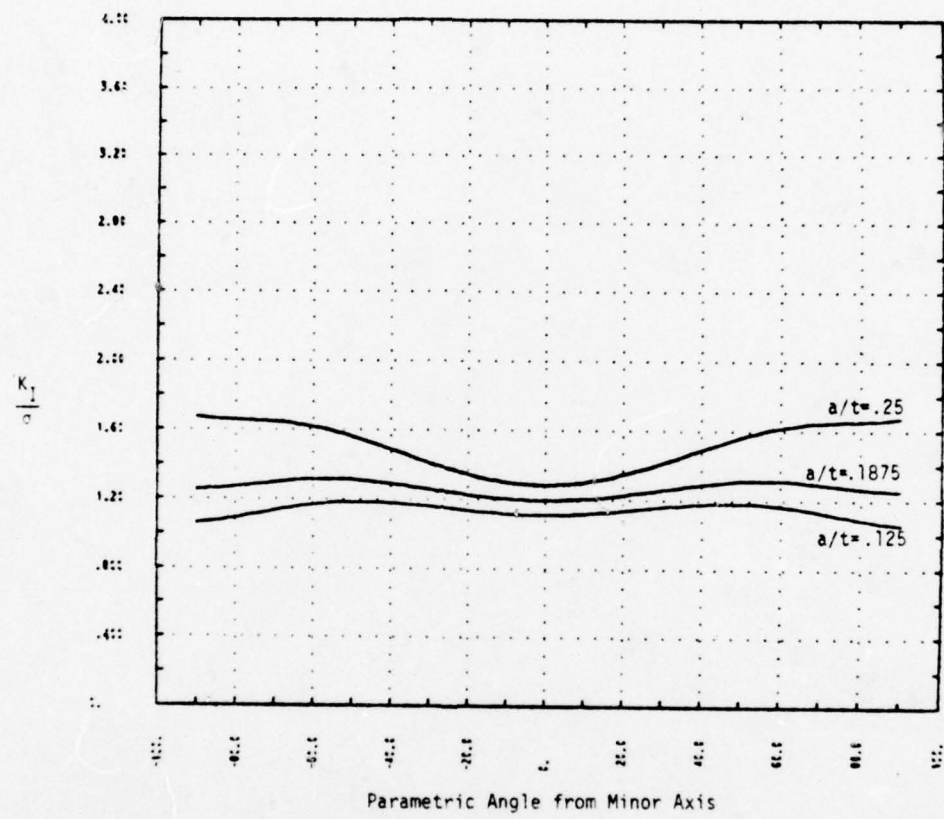


Figure 4.5 Magnification Factor Versus Angle from Minor Axis  
Embedded Cracks  
 $a/c=0.5$ ,  $d/t=1.0$ ,  $Q/P=0.0$

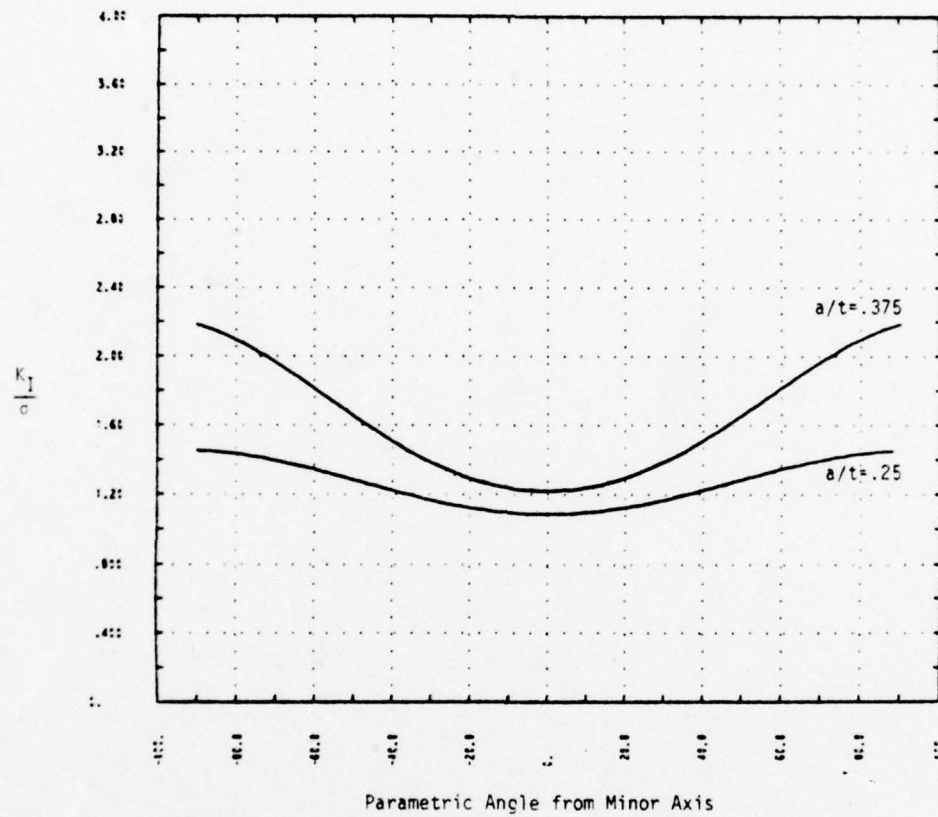


Figure 4.6 Magnification Factor Versus Angle from Minor Axis  
 Embedded Cracks  
 $a/c=0.75$ ,  $d/t=1.0$ ,  $Q/P=0.0$

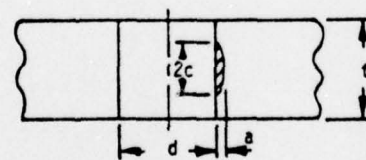
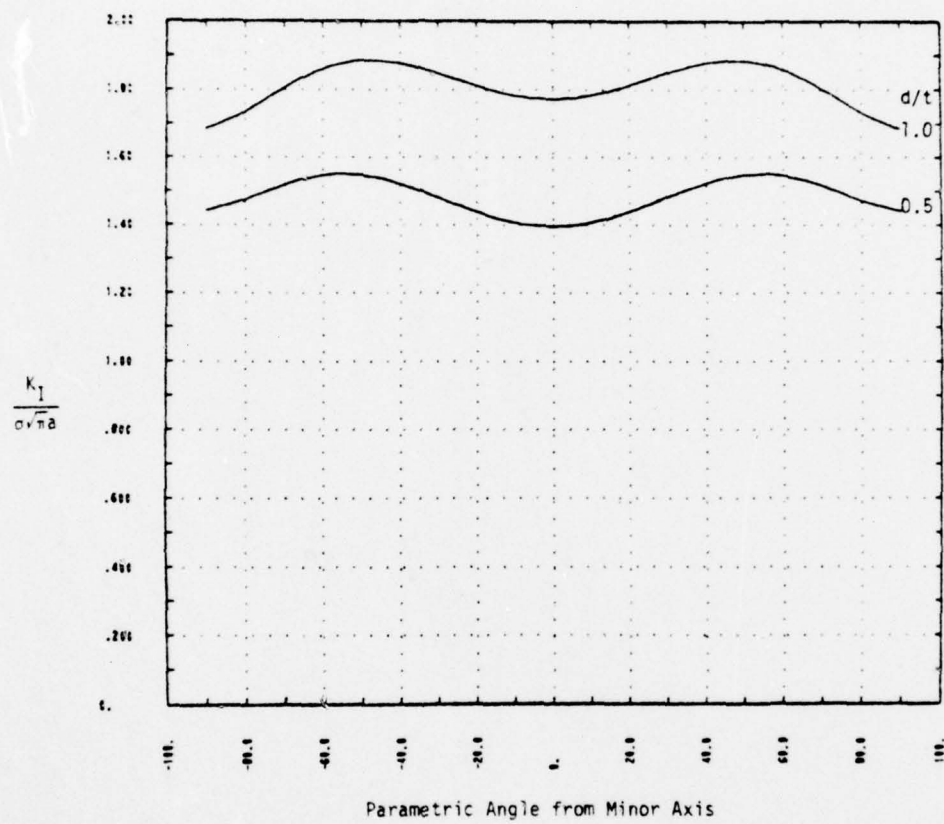


Figure 4.7 Magnification Factor Versus Angle from Minor Axis  
Embedded Cracks  
 $a/c=0.50$ ,  $a/t=0.125$ ,  $Q/P=0.0$

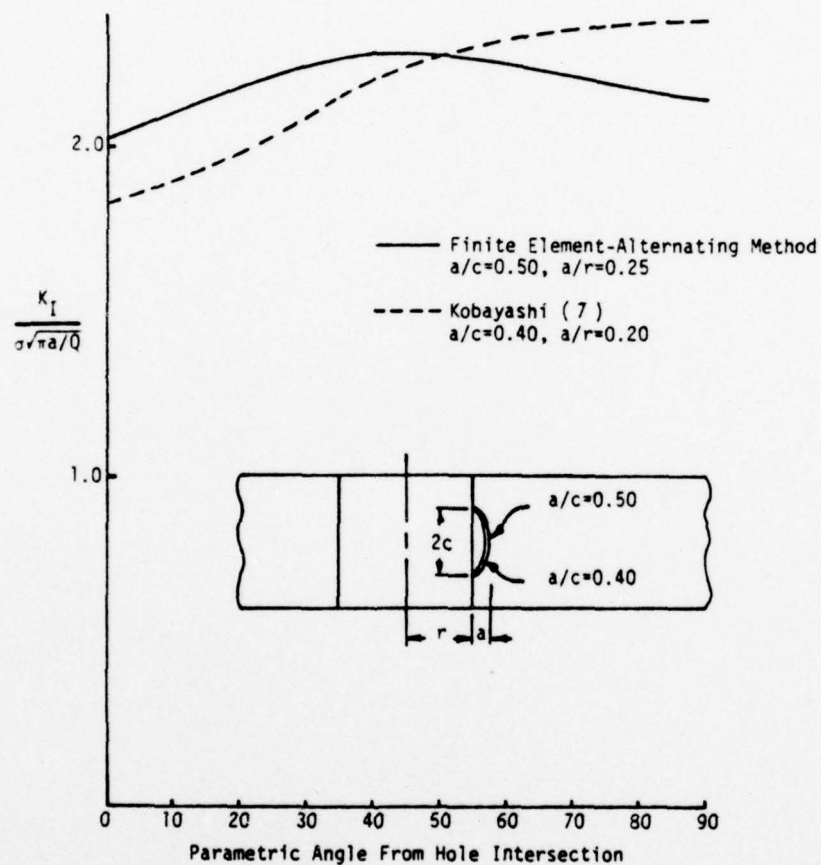


Figure 4.8 Comparison of Present Results with Another Author's Estimate

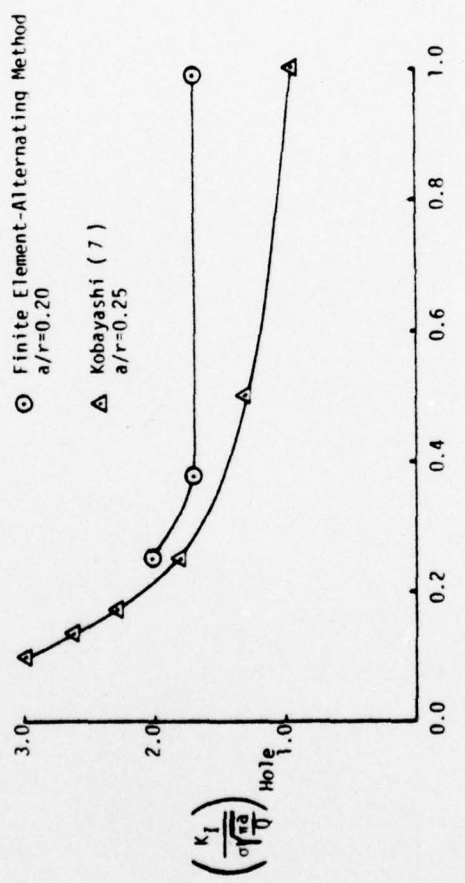


Figure 4.9 Comparative Parametric Plot, Estimates by Another Author Versus Present Solution Results

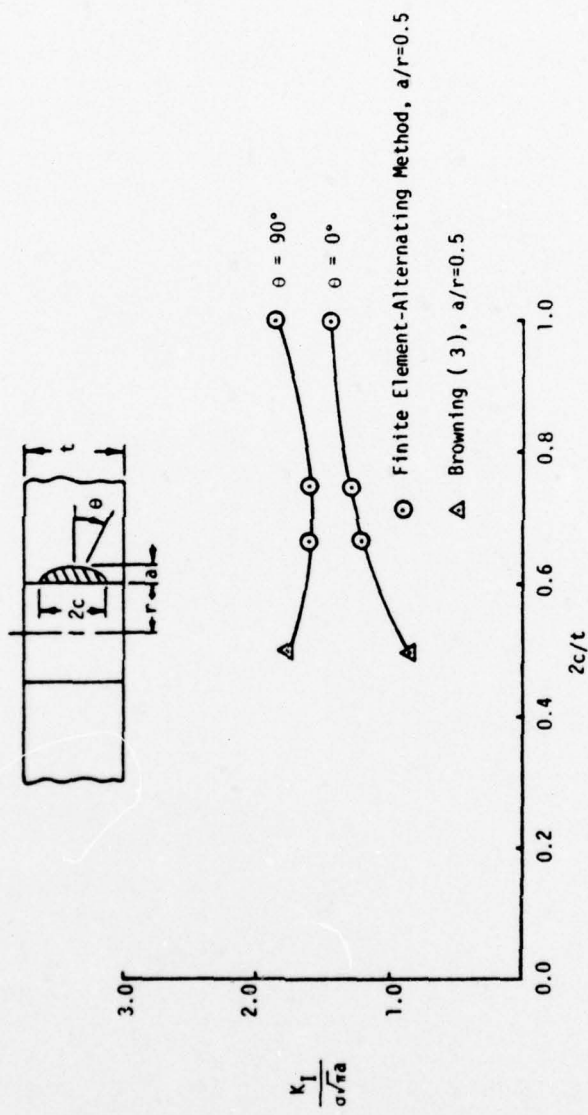


Figure 4.10 Comparative Parametric Plot, Solution By Another Author Versus Present Solution Results

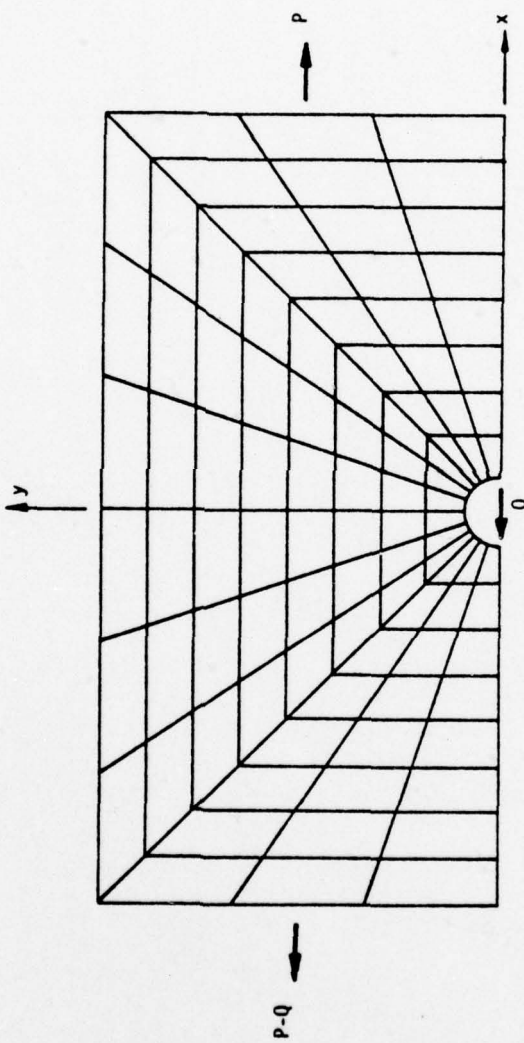


Figure 5.1 96-Element Finite Element Mesh Used to Generate Crack Plane Stresses for Loaded Fastener Hole Cases

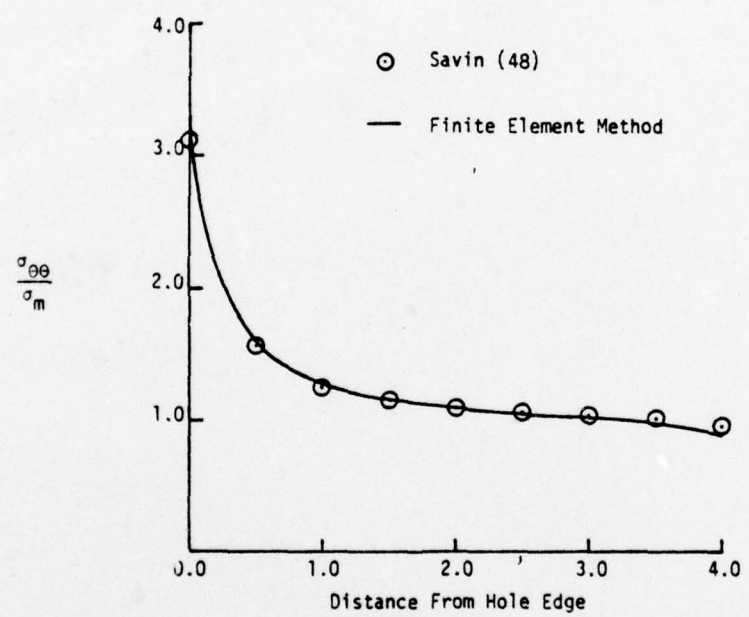


Figure 5.2 Tangential Stress Along the Minimum Section in a Plate Under Uniaxial Loading, Open Hole,  $\lambda=0.2$

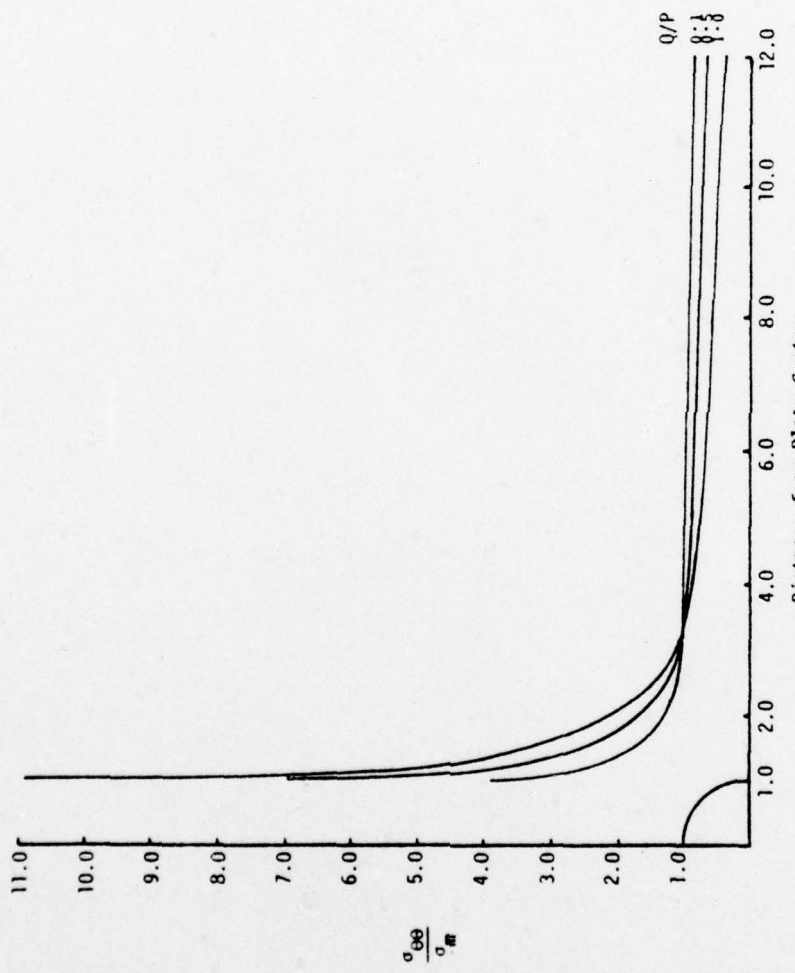


Figure 5.3 Tangential Stress Along the Minimum Section in a Plate with Load Transfer to a Fastener,  $\lambda=0.0833$

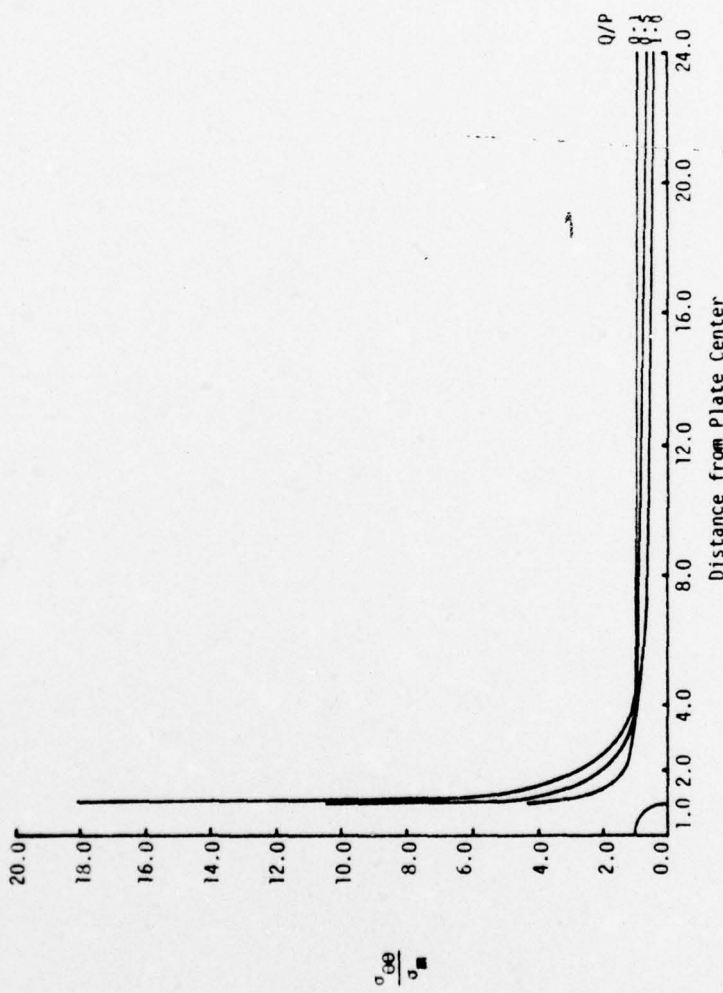


Figure 5.4 Tangential Stress Along the Minimum Section in a Plate with Load Transfer to a Fastener,  $\lambda=0.04167$

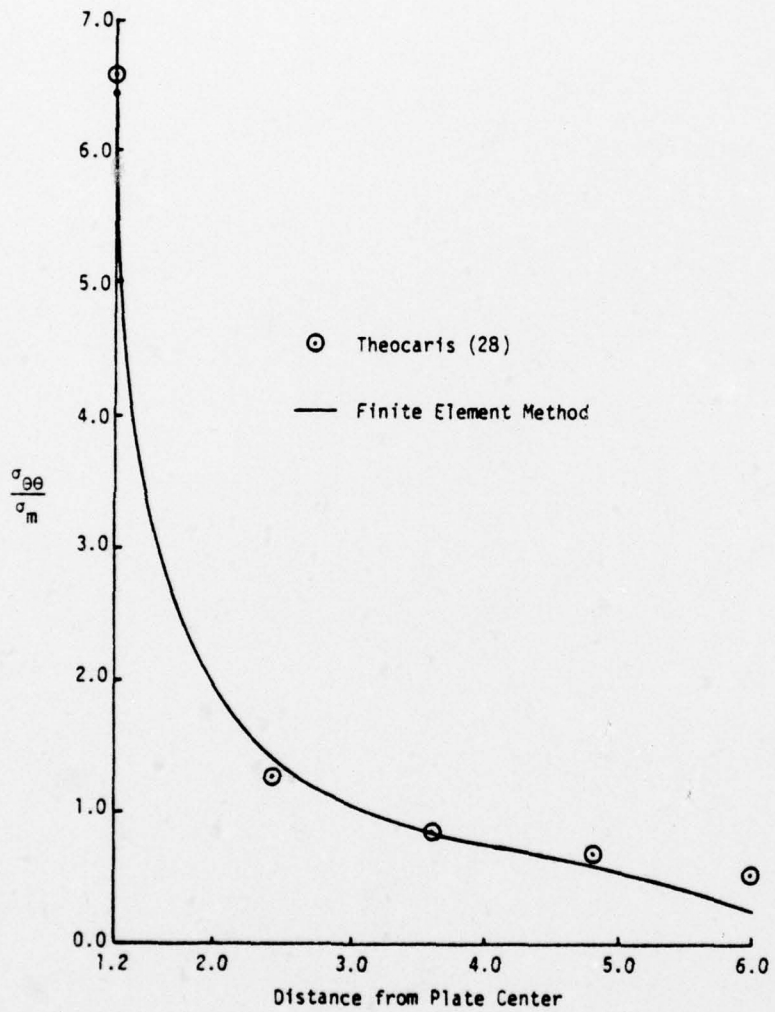


Figure 5.5 Tangential Stress Along the Minimum Section in a Plate with 100% Load Transfer to a Fastener,  $\lambda=0.2$

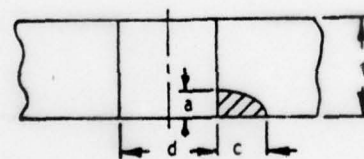
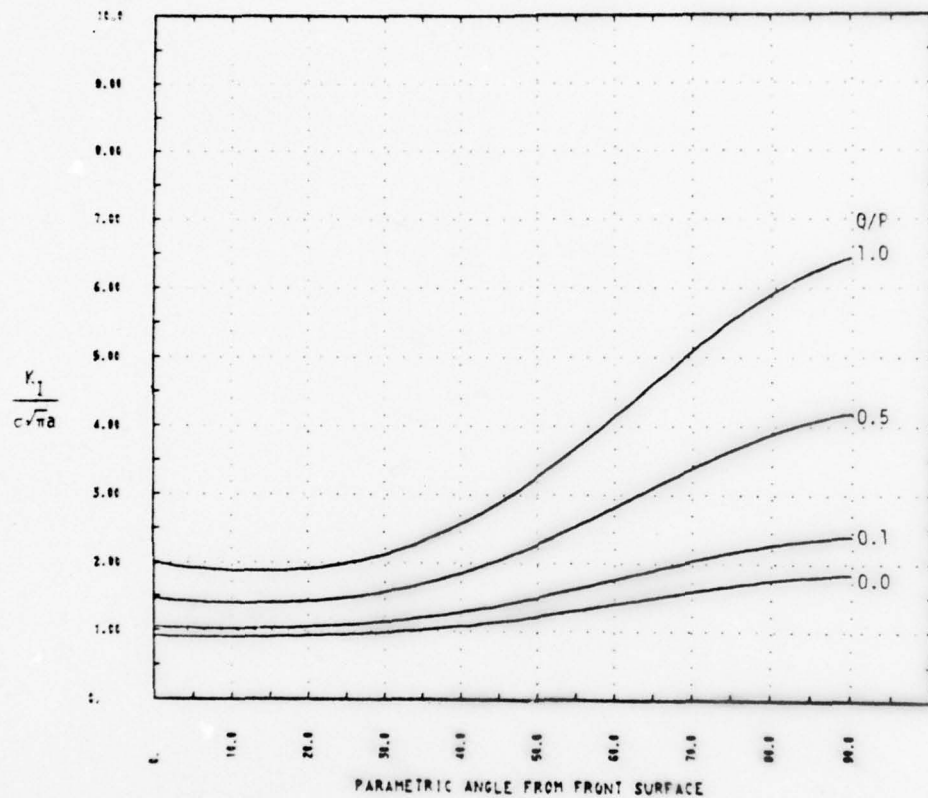


Figure 5.6 Magnification Factor Versus Angle from Front Surface  
Single Corner Cracks  
 $a/c=0.5$ ,  $a/t=0.25$ ,  $d/t=1.0$

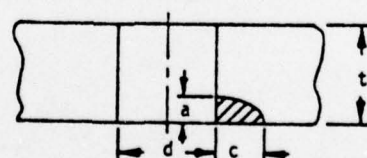
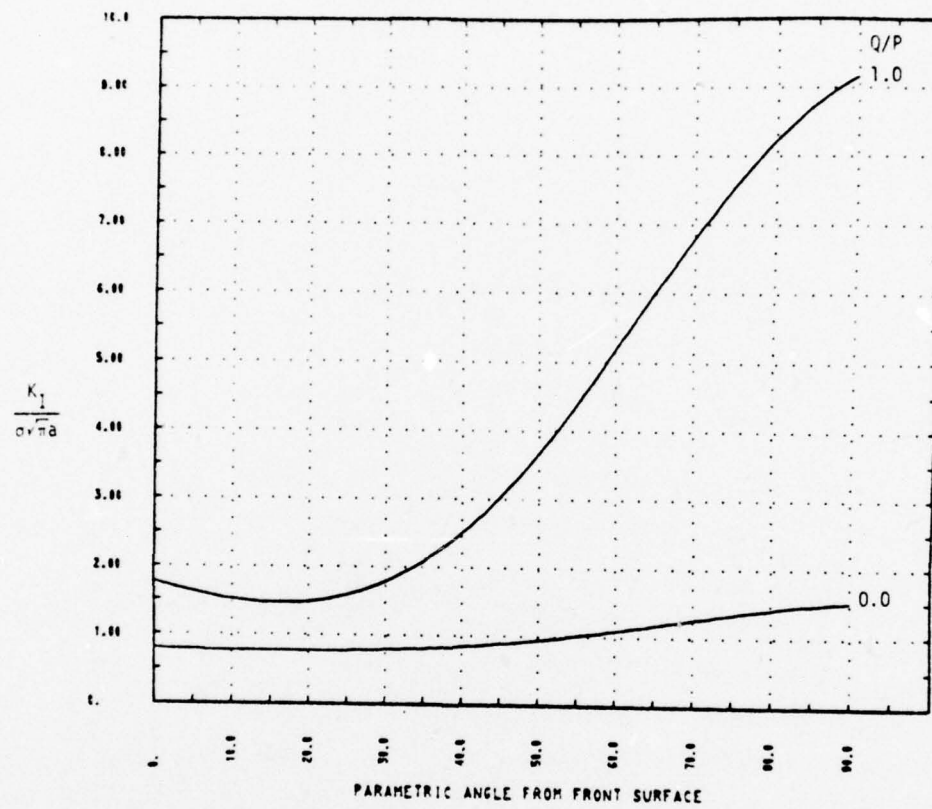


Figure 5.7 Magnification Factor Versus Angle from Front Surface  
 Single Corner Cracks  
 $a/c=0.5$ ,  $a/t=0.25$ ,  $d/t=0.5$

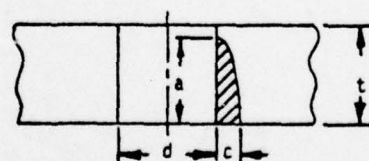
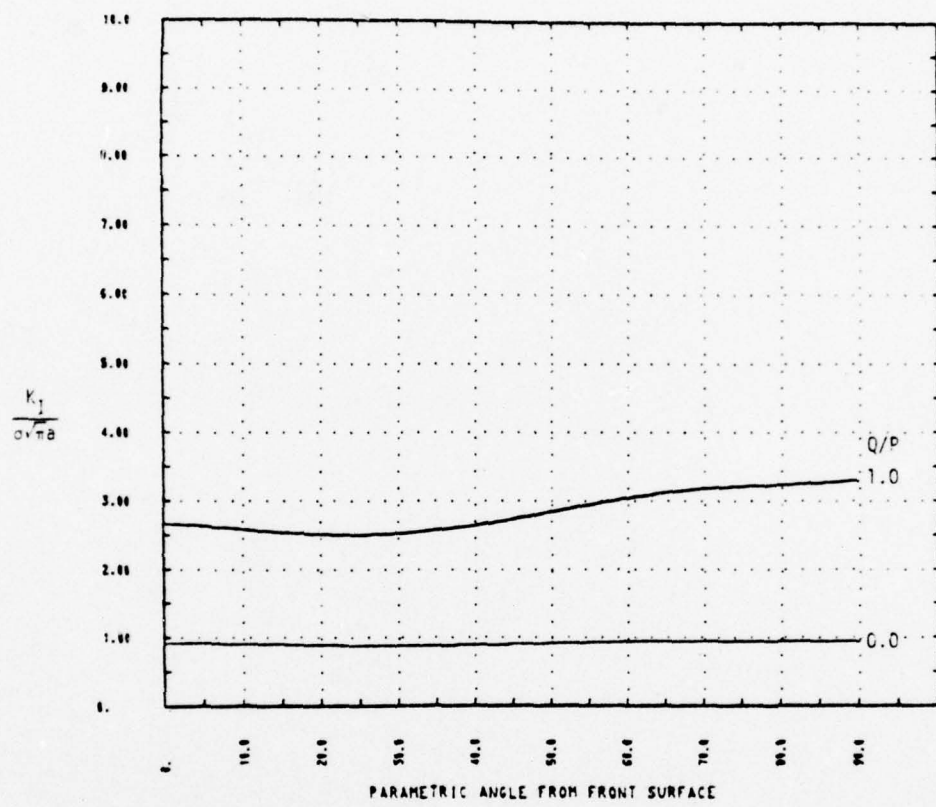


Figure 5.8 Magnification Factor Versus Angle from Front Surface  
 Single Corner Cracks  
 $a/c=2.5$ ,  $a/t=0.85$ ,  $d/t=1.0$

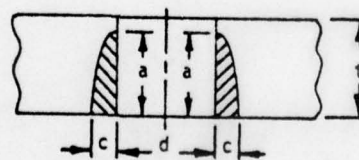
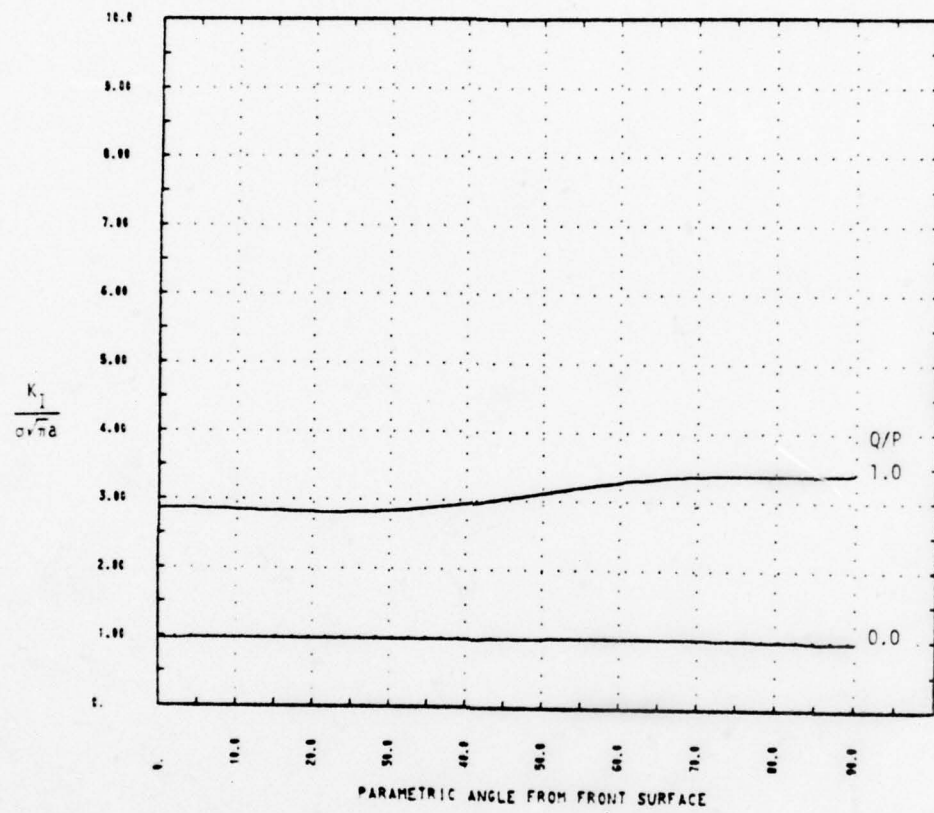


Figure 5.9 Magnification Factor Versus Angle from Front Surface  
 Double Corner Cracks  
 $a/c=2.5$ ,  $a/t=0.85$ ,  $d/t=1.0$

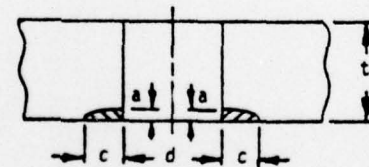
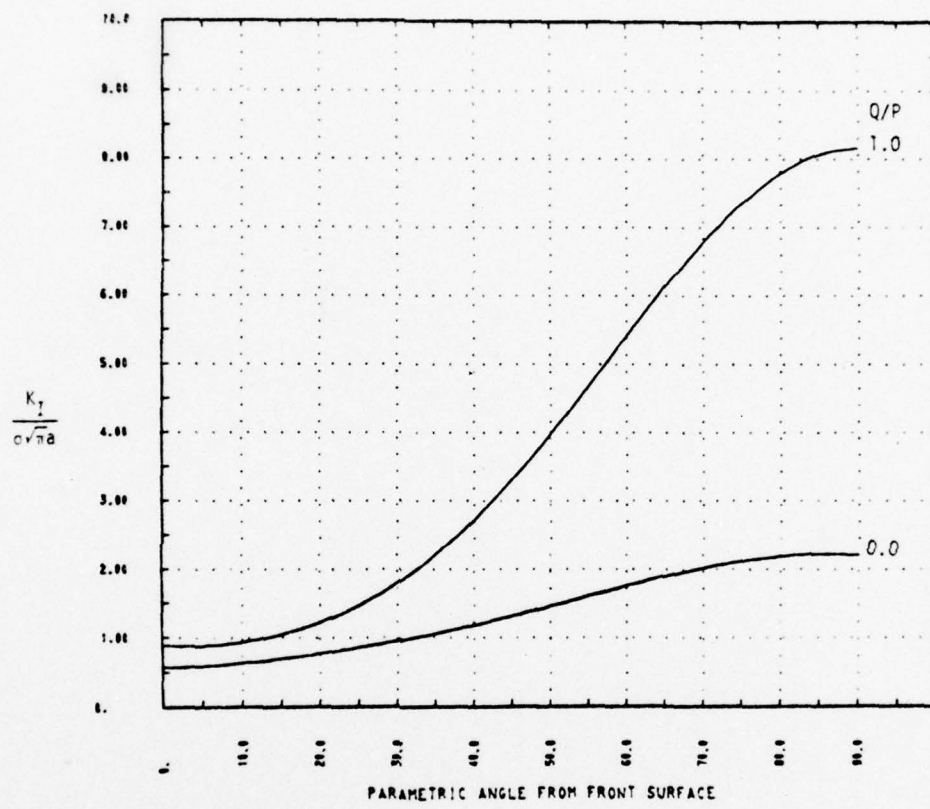


Figure 5.10 Magnification Factor Versus Angle from Front Surface  
 Double Corner Cracks  
 $a/c=0.25$ ,  $a/t=0.125$ ,  $d/t=1.0$

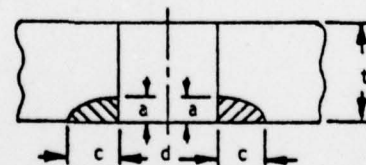
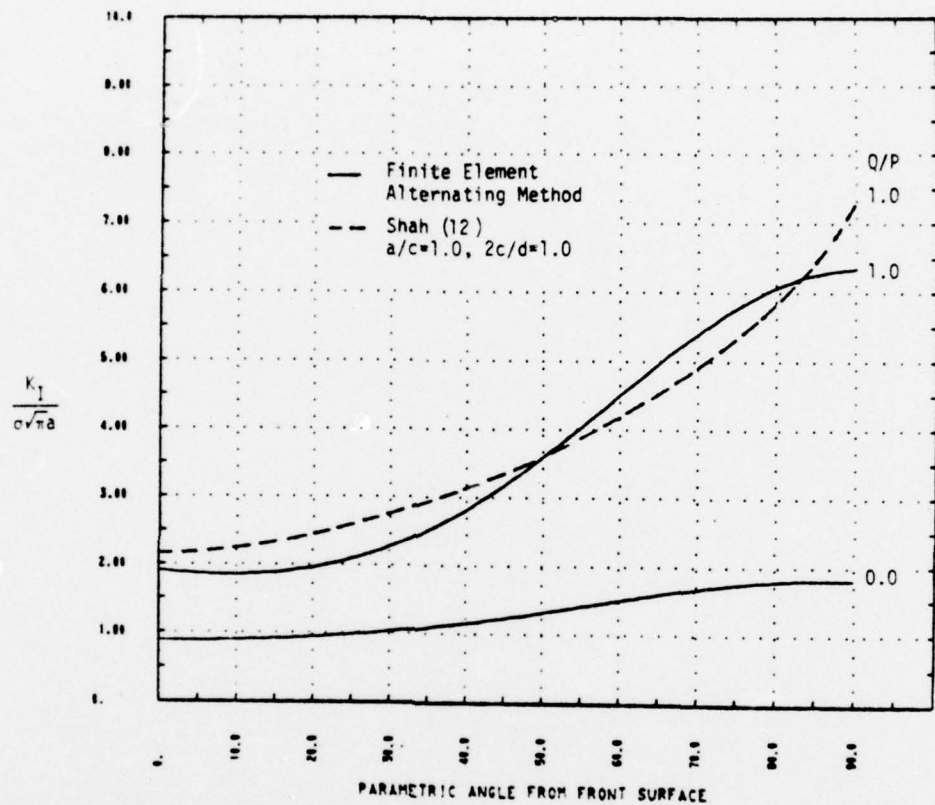


Figure 5.11 Magnification Factor Versus Angle from Front Surface  
 Double Corner Cracks  
 $a/c=0.5$ ,  $a/t=0.25$ ,  $d/t=1.0$

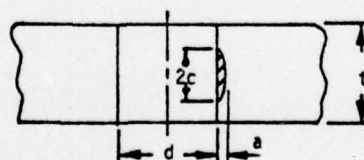
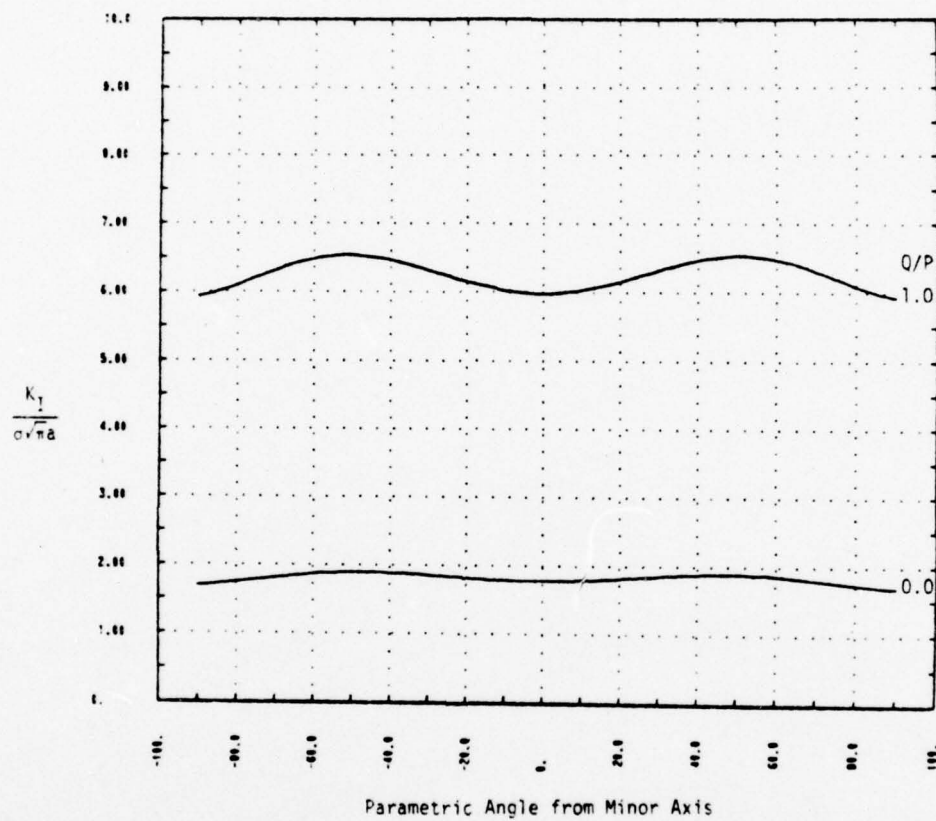


Figure 5.12 Magnification Factor Versus Angle from Minor Axis  
Embedded Cracks  
 $a/c=0.5$ ,  $a/t=0.125$ ,  $d/t=1.0$

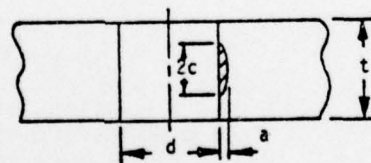
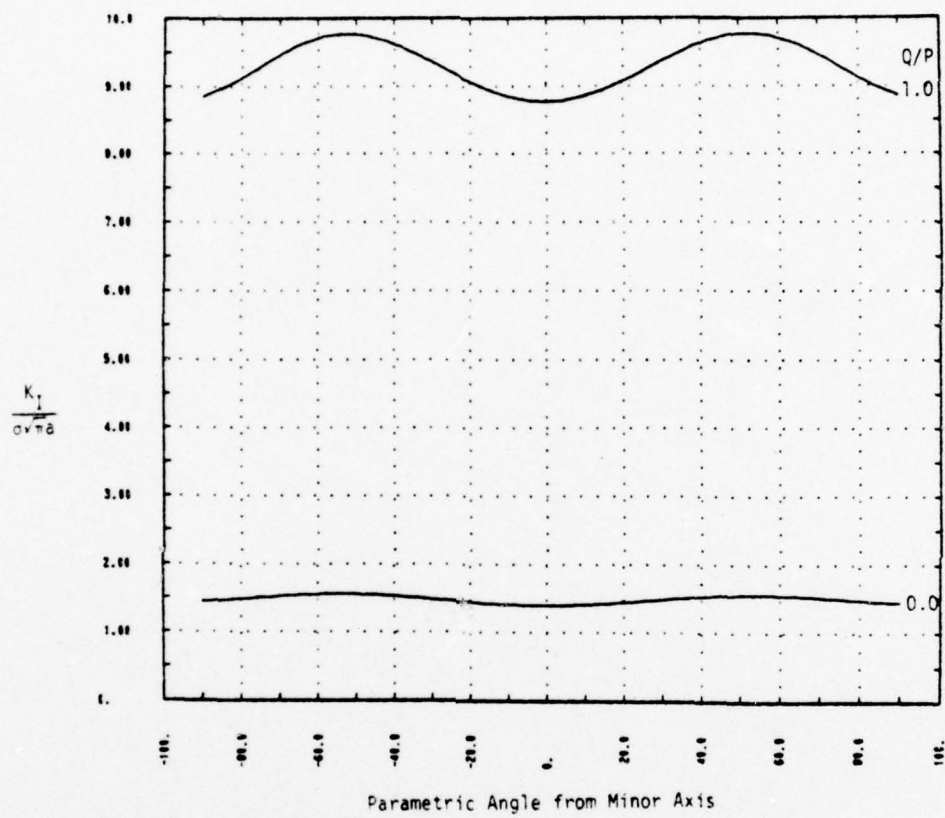


Figure 5.13 Magnification Factor Versus Angle from Minor Axis  
Embedded Cracks  
 $a/c=0.5$ ,  $a/t=0.125$ ,  $d/t=0.5$

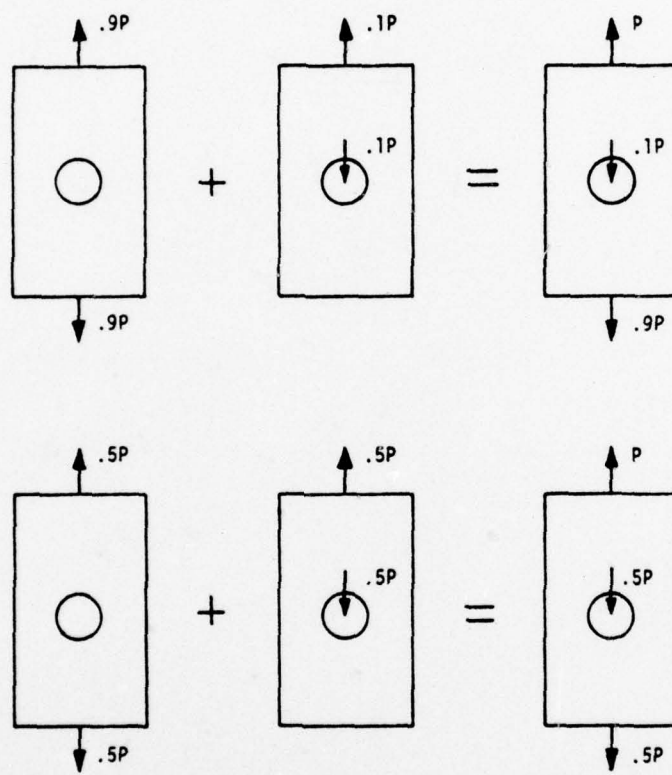


Figure 5.14 Superposition for Cases of Partial Load Transfer to a Fastener

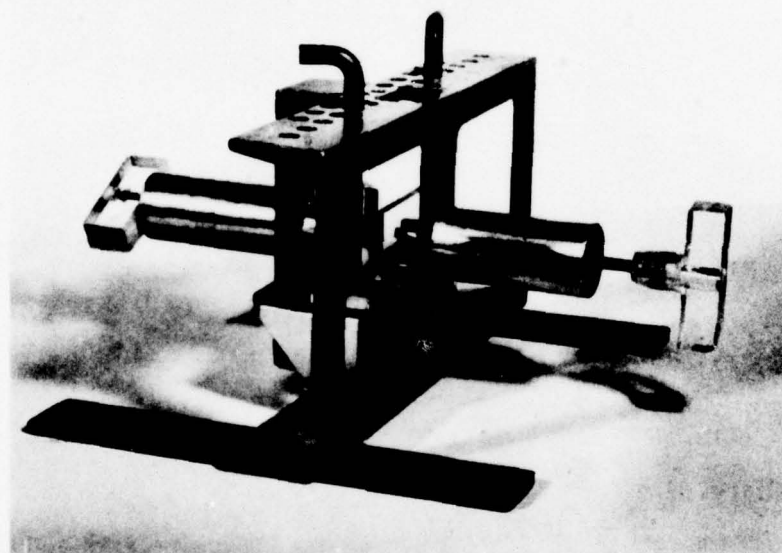


Figure 6.1 Cracking Jig for Growing Shallow Single and Double Corner Cracks

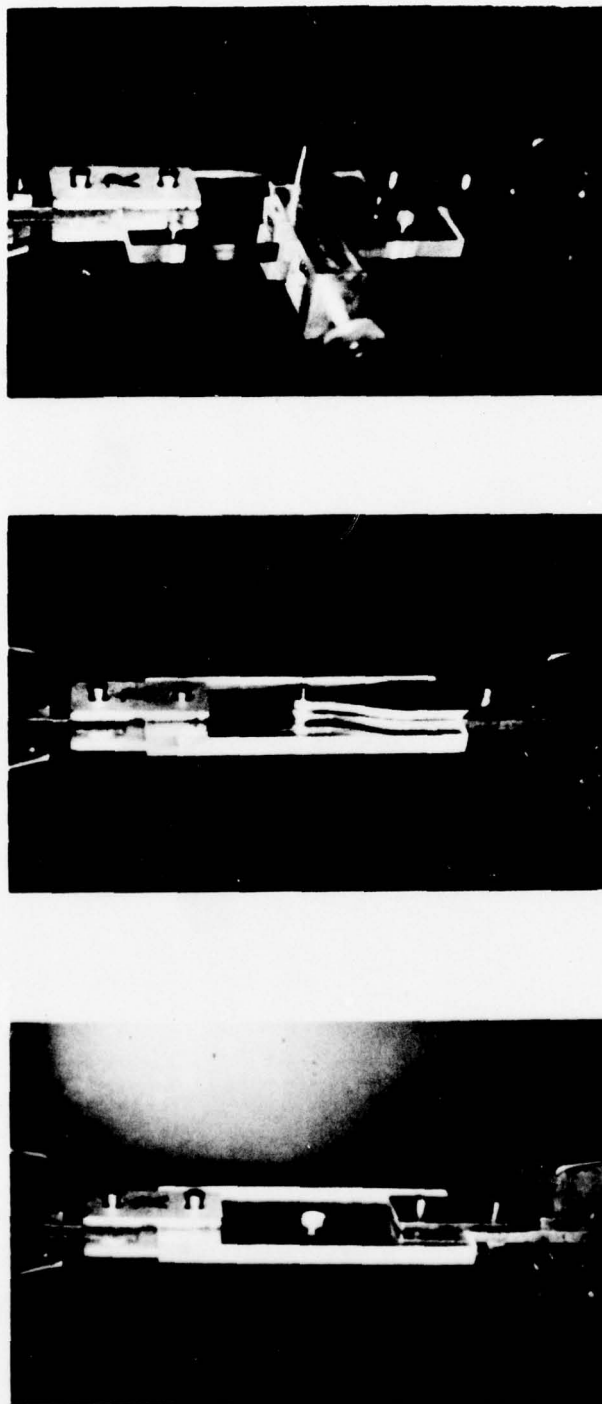


Figure 6.2 Experimental Loading Arrangements

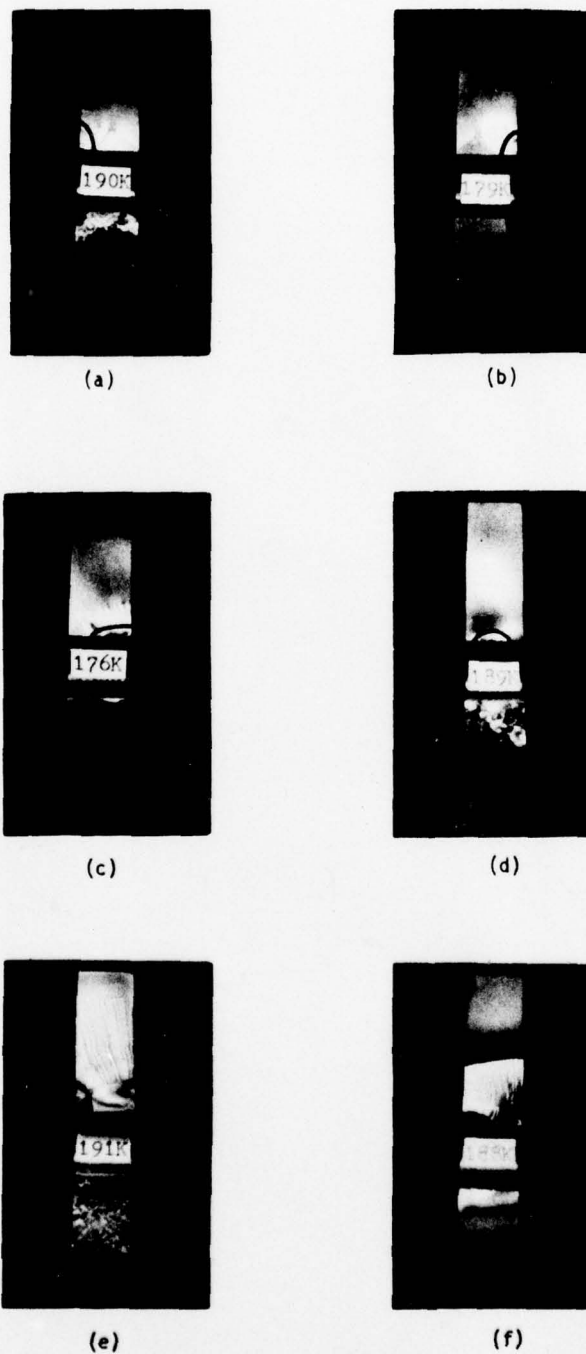


Figure 6.3 Typical Fractured Surfaces in PMMA Specimens with Cracks Emanating from Fastener Holes

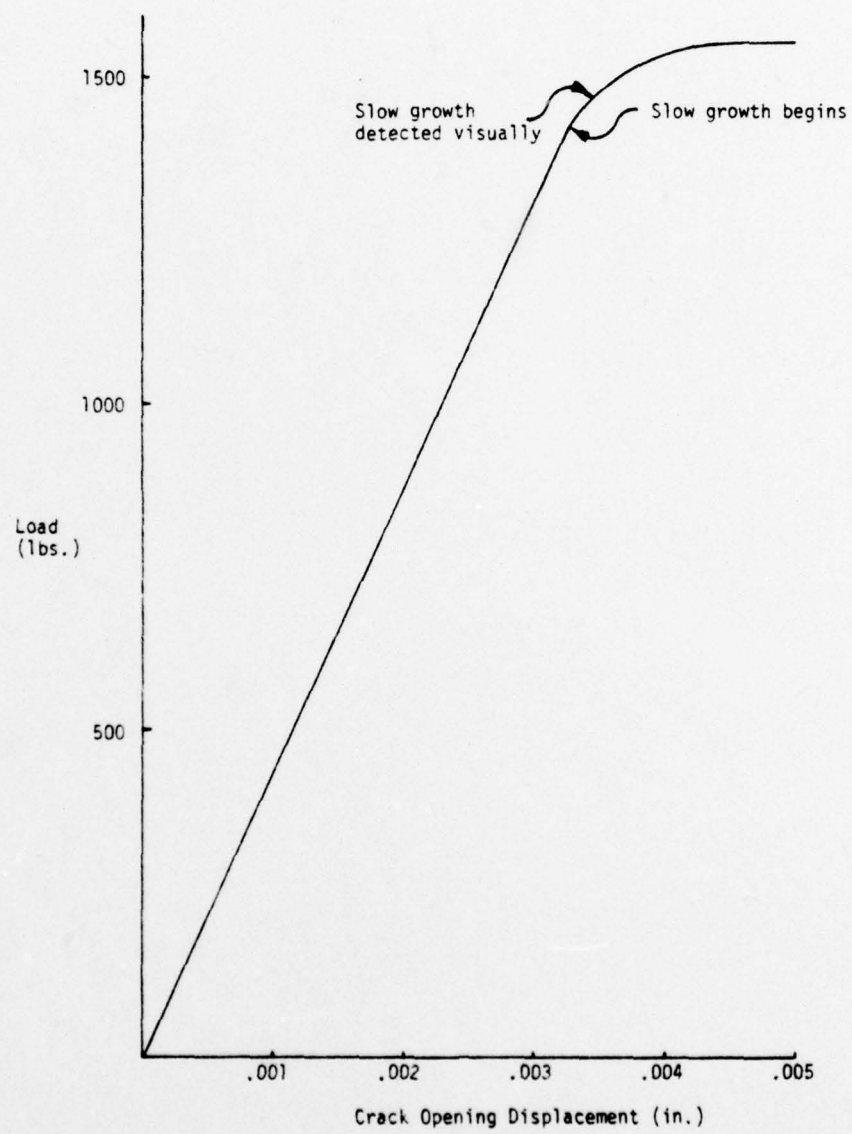


Figure 6.4 Load-Displacement Record, Double Corner Cracks at an Open Fastener Hole.

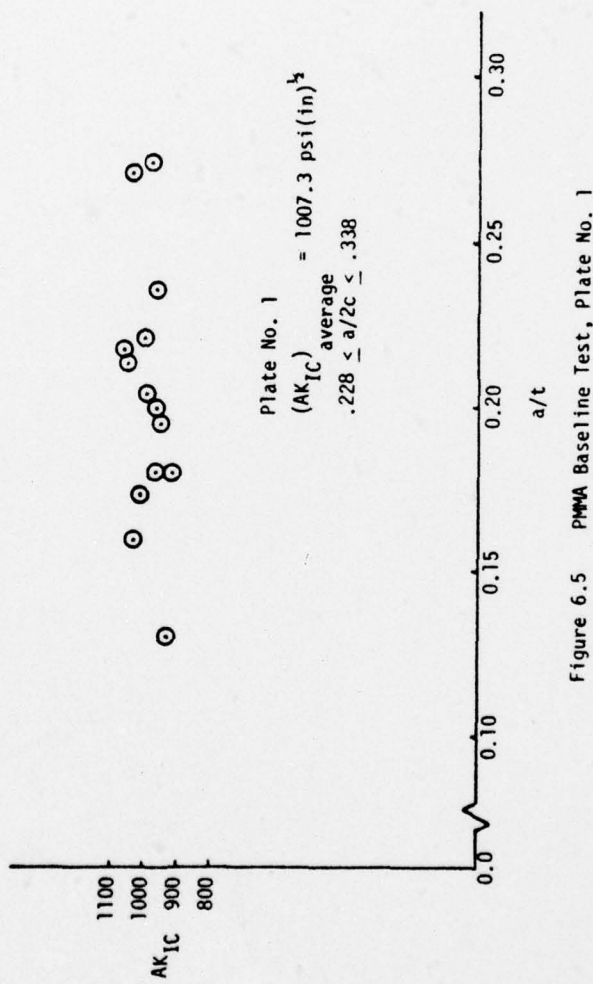


Figure 6.5 PMMA Baseline Test, Plate No. 1

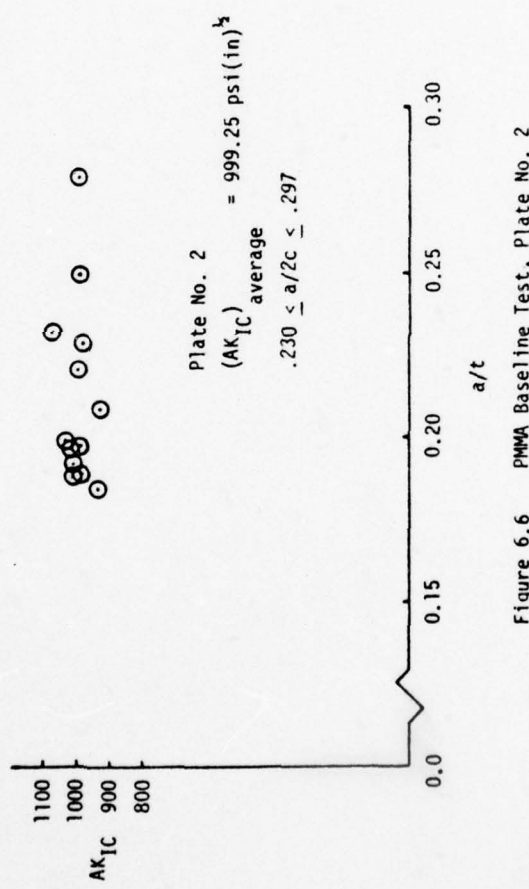


Figure 6.6 PMMA Baseline Test, Plate No. 2

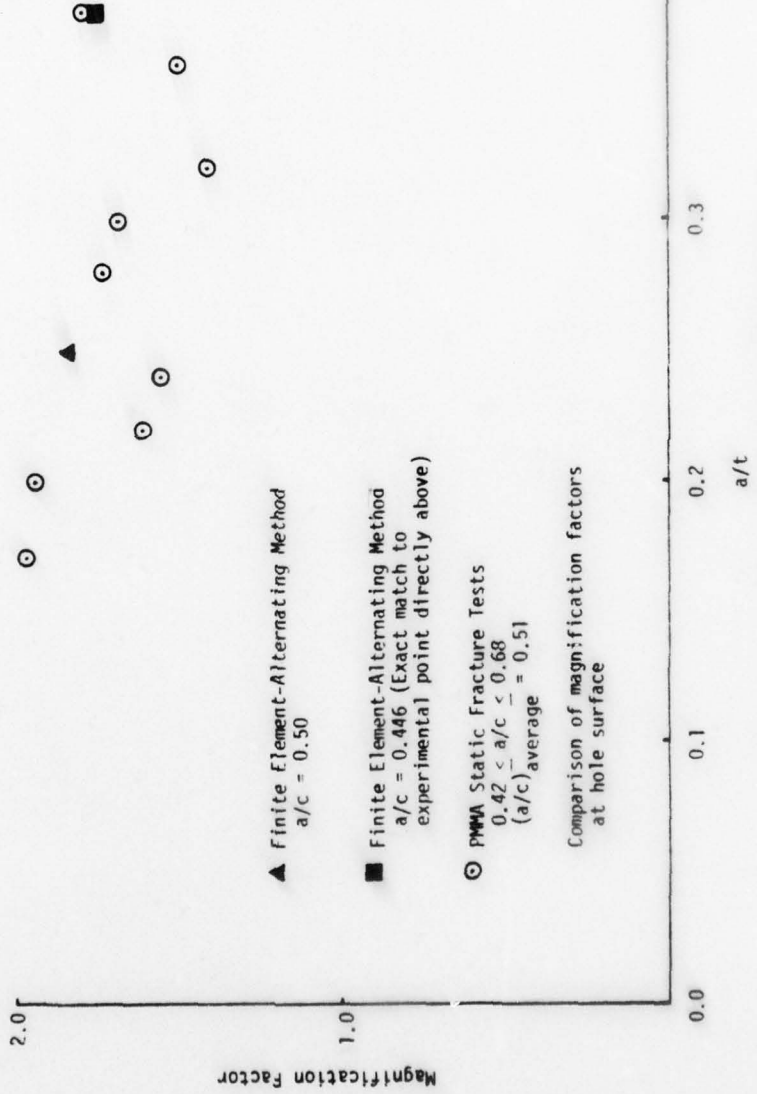


figure 6.7 Comparison of Theory and PMMA Experiments  
Single Corner Crack,  $a/t = 1.0$ ,  $Q/P = 0.0$

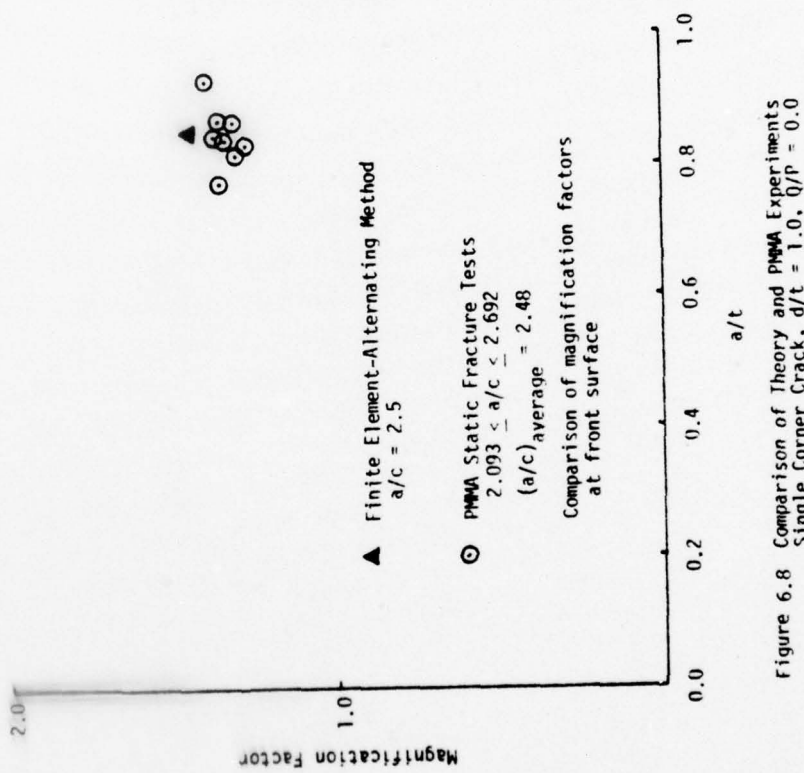


Figure 6.8 Comparison of Theory and PMMA Experiments  
Single Corner Crack,  $d/t = 1.0$ ,  $Q/P = 0.0$

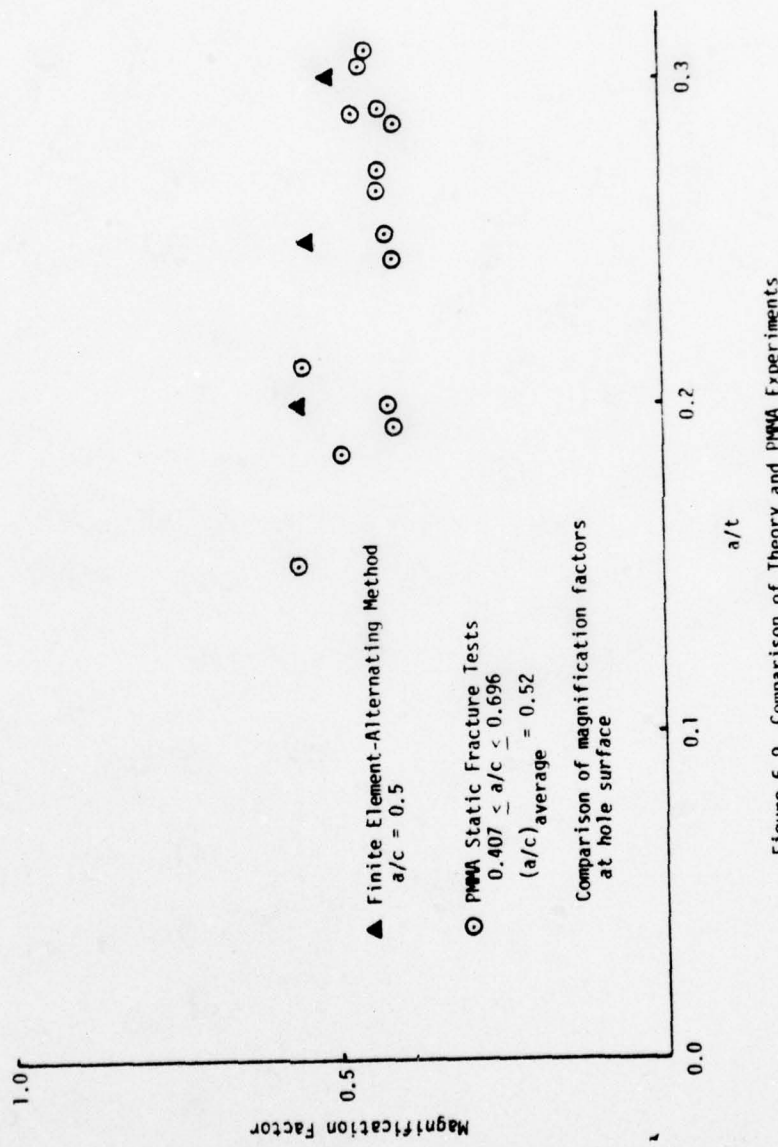


Figure 6.9 Comparison of Theory and PMMA Experiments  
 Single Corner Crack,  $d/t \approx 1.0$ ,  $Q/P = 1.0$

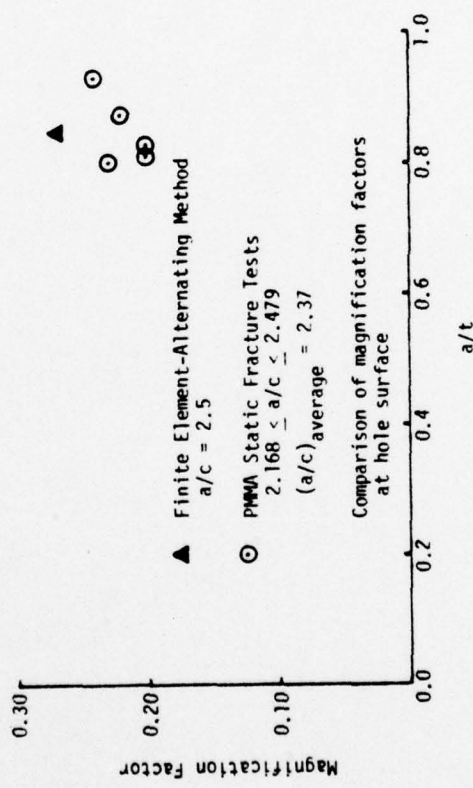


Figure 6.10 Comparison of Theory and PMMA Experiments  
 Single Corner Crack,  $d/t = 1.0$ ,  $Q/P = 1.0$

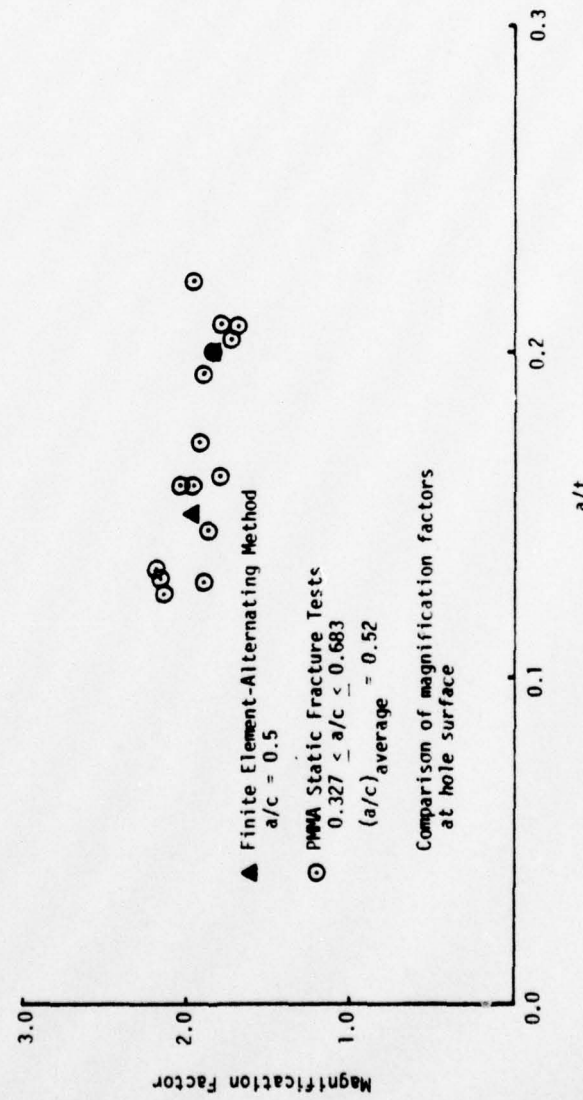


Figure 6.11 Comparison of Theory and PMMA Experiments  
Double Corner Cracks,  $d/t = 1.0$ ,  $Q/P = 0.0$

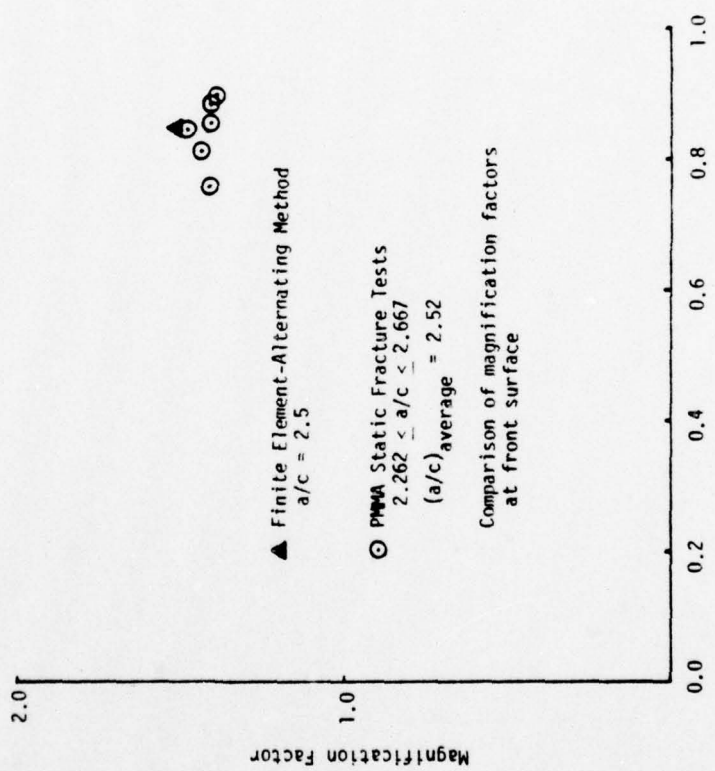


Figure 6.12 Comparison of Theory and PMMA Experiments  
Double Corner Cracks,  $d/t = 1.0$ ,  $Q/P = 0.0$

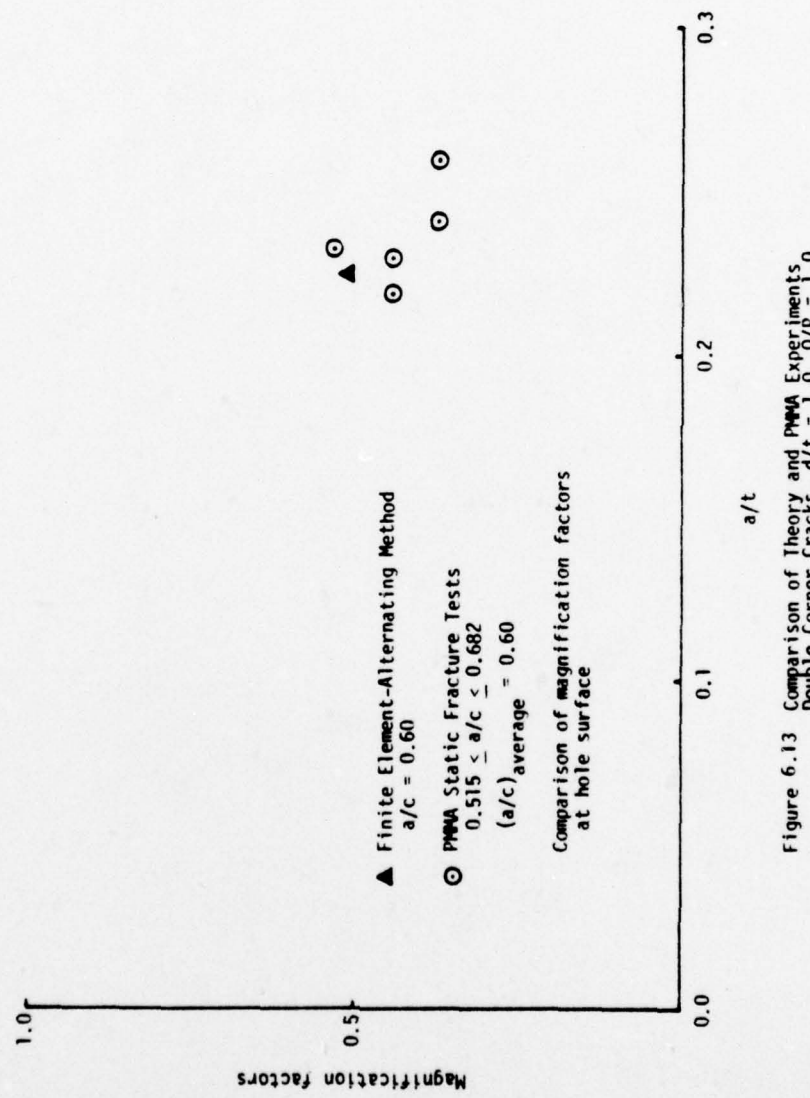


Figure 6.13 Comparison of Theory and PMMA Experiments  
Double Corner Cracks,  $d/t = 1.0$ ,  $Q/p = 1.0$

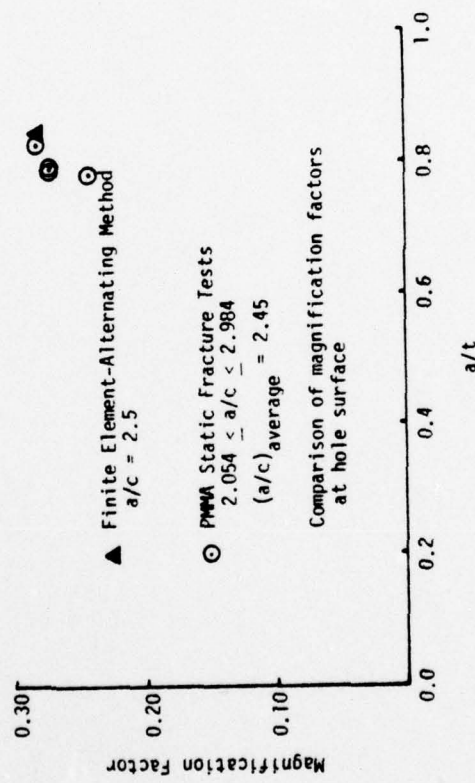


Figure 6.14 Comparison of Theory and PMMA Experiments  
 Double Corner Cracks,  $d/t = 1.0$ ,  $Q/p = 1.0$

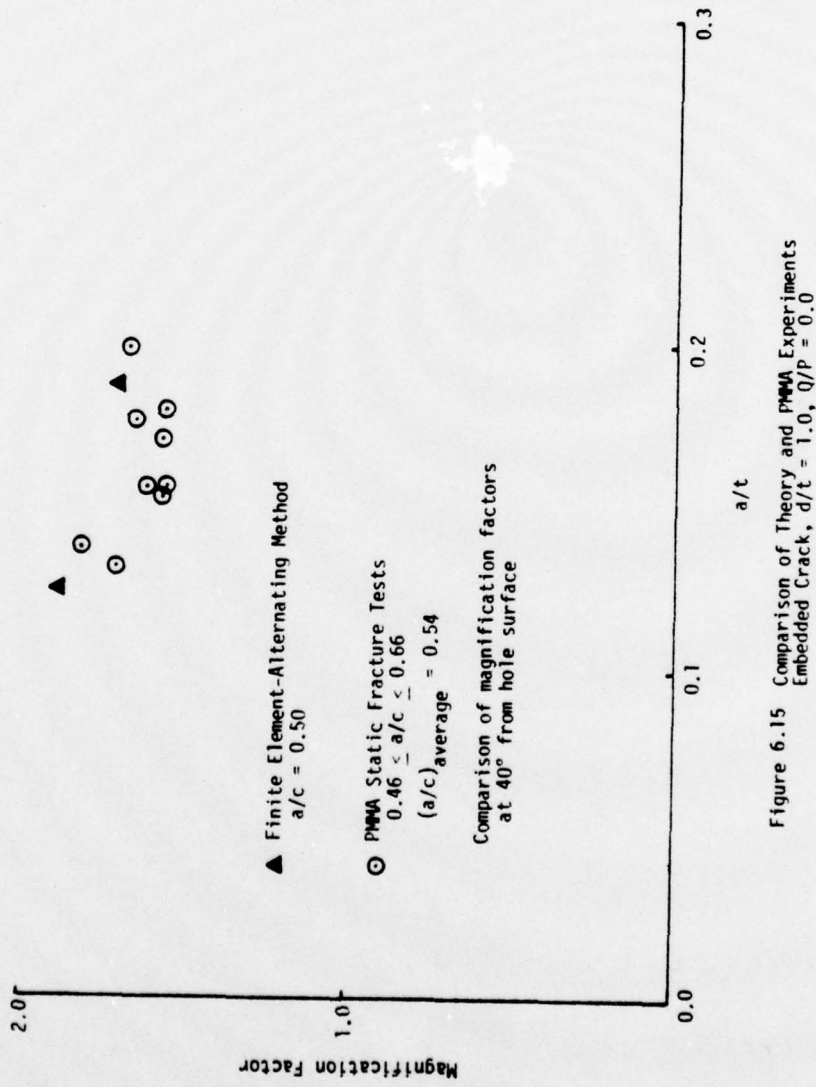


Figure 6.15 Comparison of Theory and PMMA Experiments  
 Embedded Crack,  $d/t = 1.0$ ,  $Q/p = 0.0$

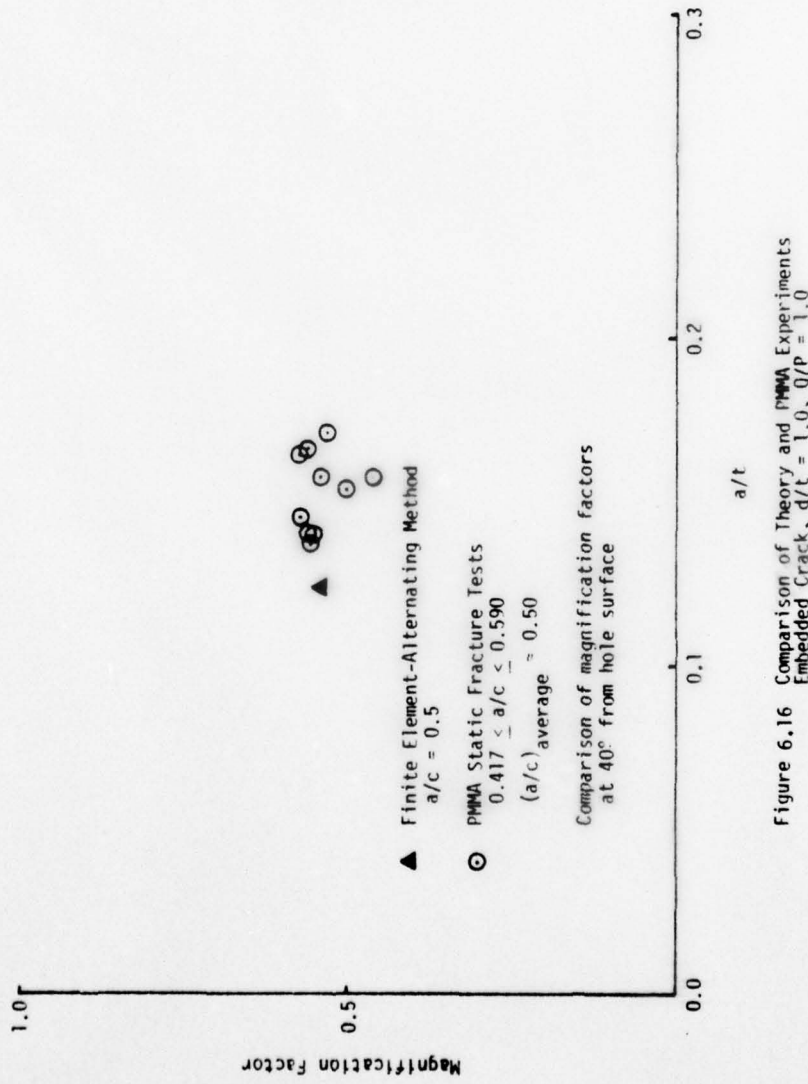


Figure 6.16 Comparison of Theory and PMMA Experiments  
 Embedded Crack,  $d/t = 1.0$ ,  $Q/p = 1.0$

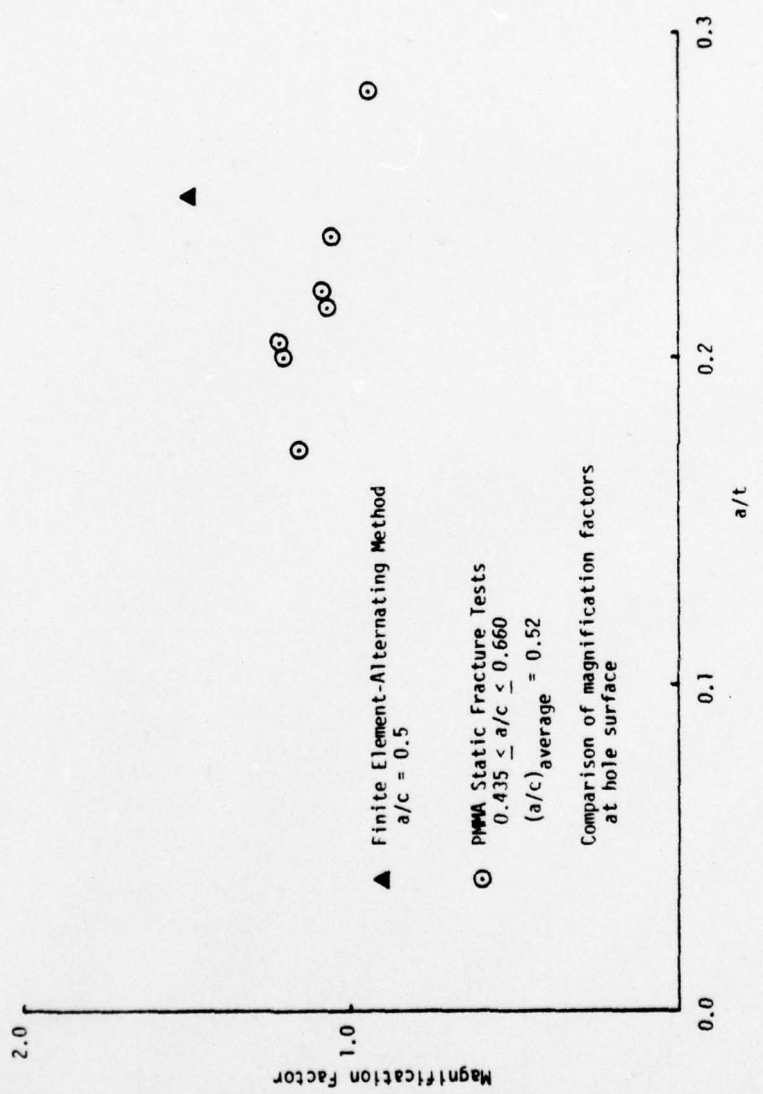


Figure 6.17 Comparison of Theory and PMMA Experiments  
Single Corner Crack,  $d/t = 0.5$ ,  $\alpha/p = 0.0$

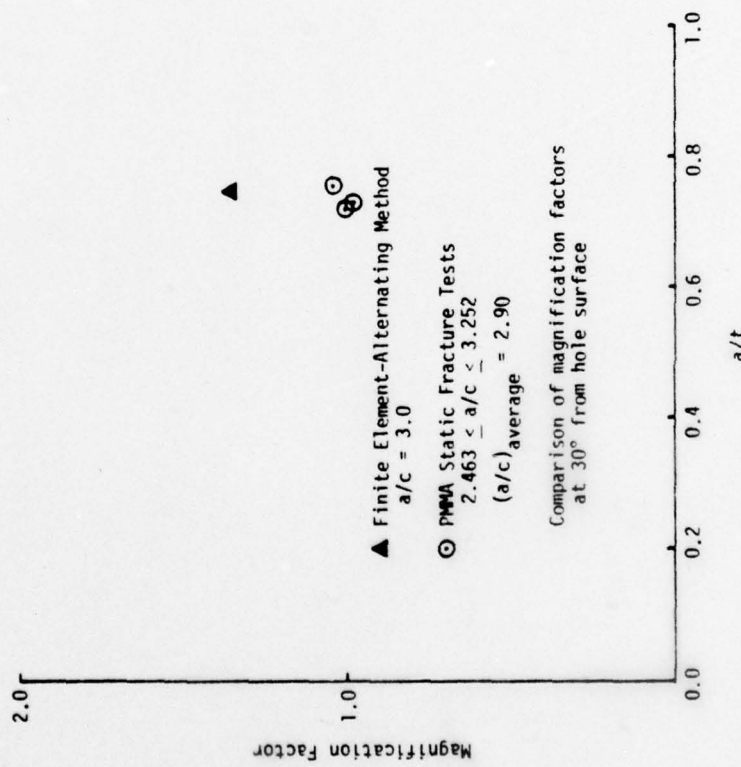


Figure 6.18 Comparison of Theory and PMMA Experiments  
Single Corner Crack,  $d/t = 0.5$ ,  $Q/P = 0.0$

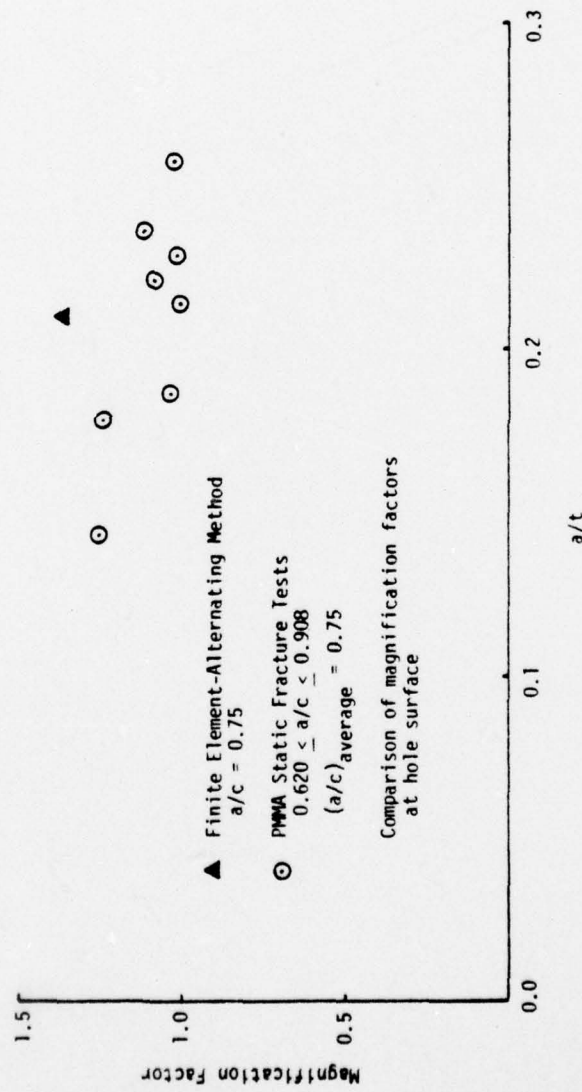


Figure 6.19 Comparison of Theory and PMMA Experiments  
Double Corner Crack,  $d/t = 0.5$ ,  $\eta/p = 0.0$

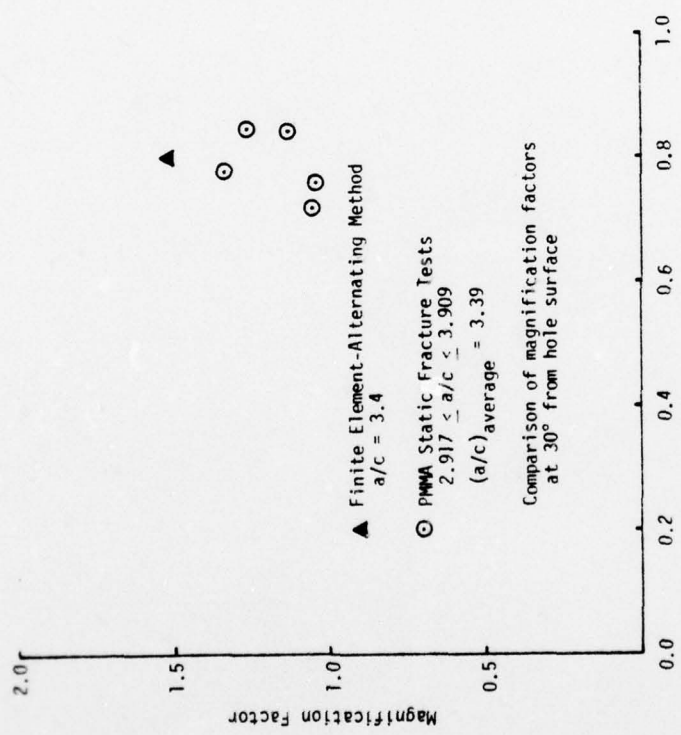


Figure 6.20 Comparison of Theory and PMMA Experiments  
for Double Corner Cracks,  $d/t = 0.5$ ,  $Q/p = 0.0$

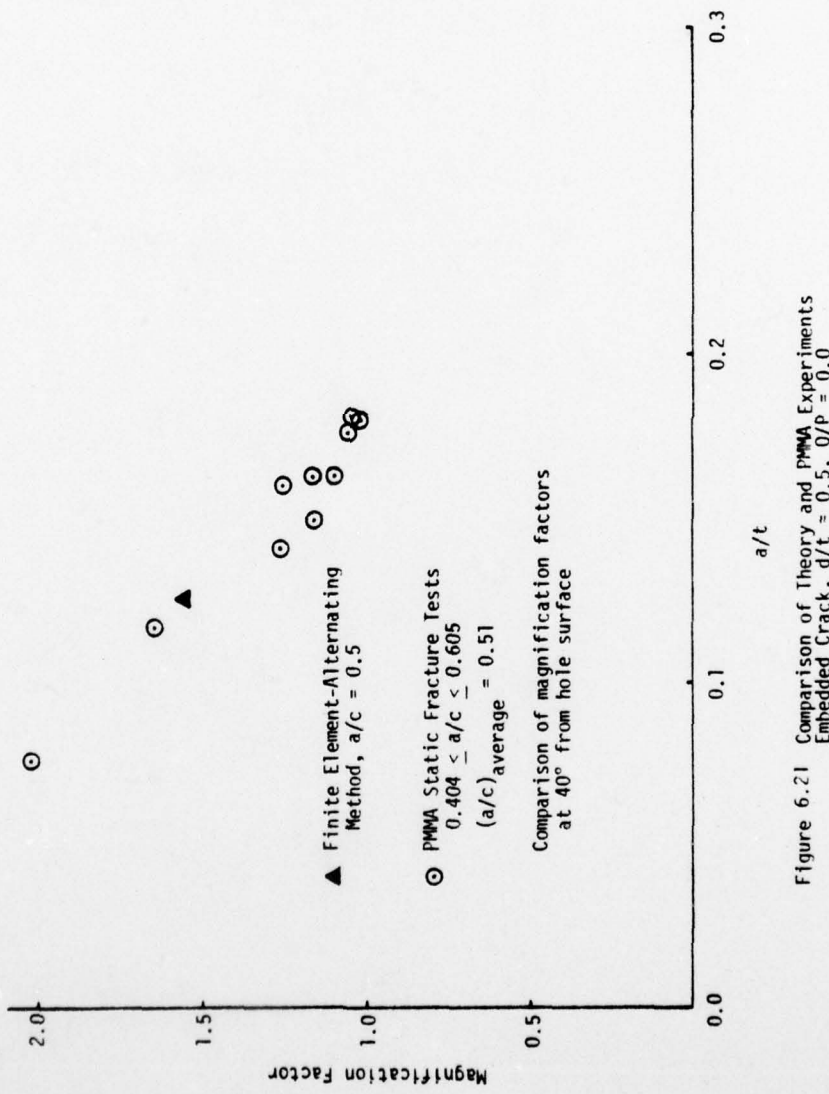


Figure 6.21 Comparison of Theory and PMMA Experiments  
Embedded Crack,  $d/t = 0.5$ ,  $Q/P = 0.0$

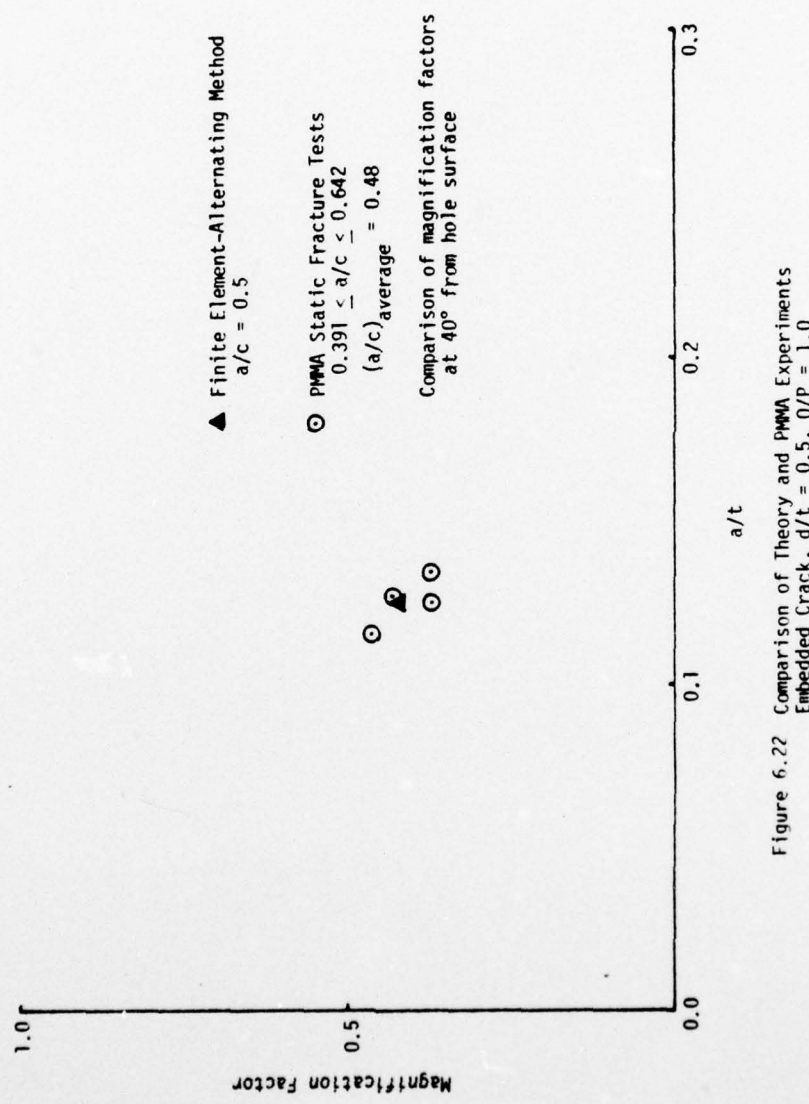


Figure 6.22 Comparison of Theory and PMMA Experiments  
Embedded Crack,  $d/t = 0.5$ ,  $Q/P = 1.0$

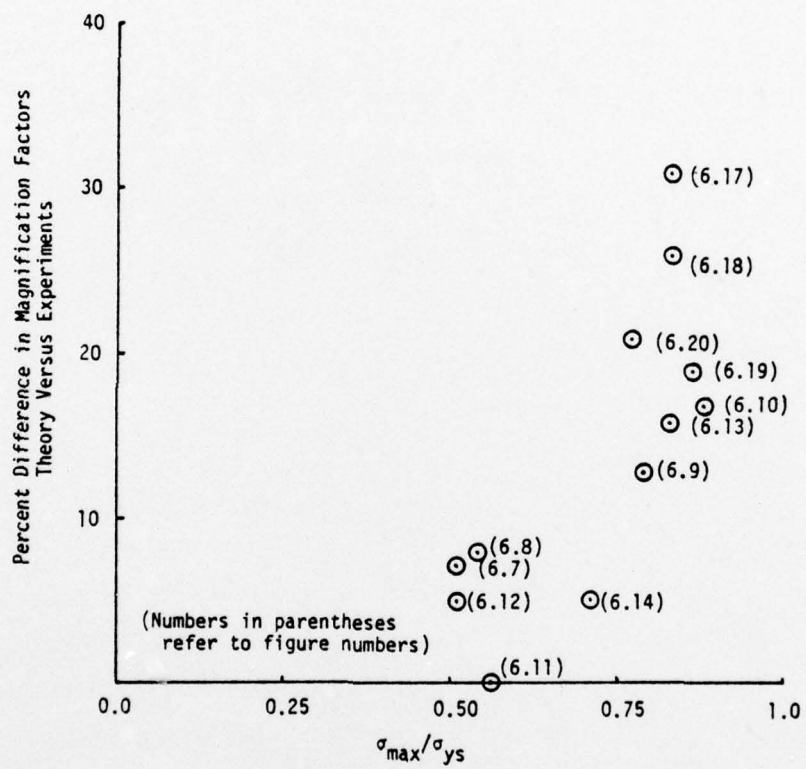


Figure 6.23 Difference Between Theoretical and Experimental Results as a Function of Maximum Local Crack Plane Normal Stress in the Experiments

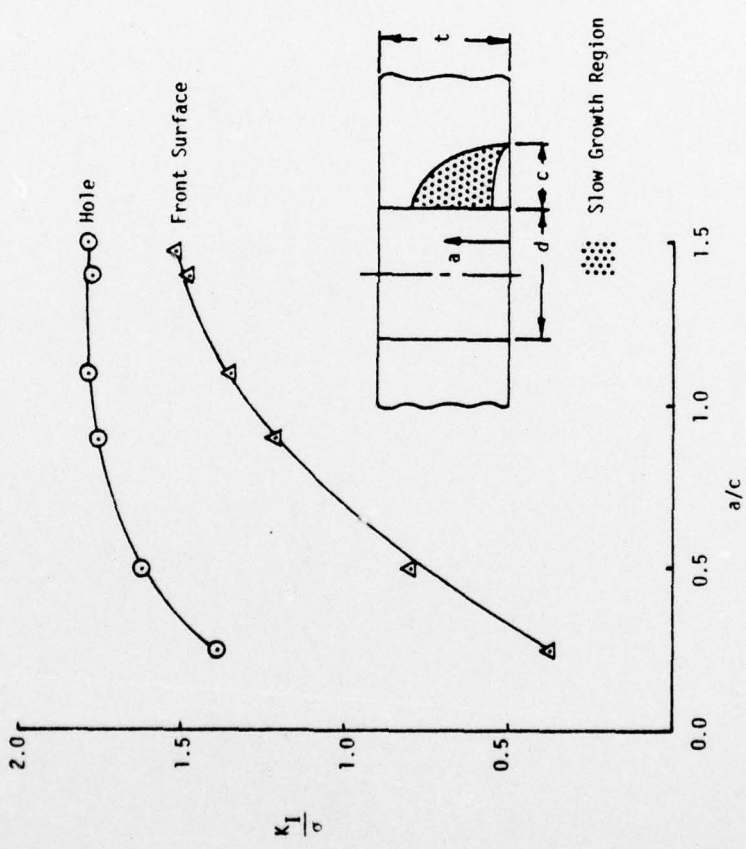


Figure 6.24 Parametric Plot of Theory to Approximate Slow Growth,  
Single Corner Crack,  $c/t=0.5$ ,  $d/t=1.0$

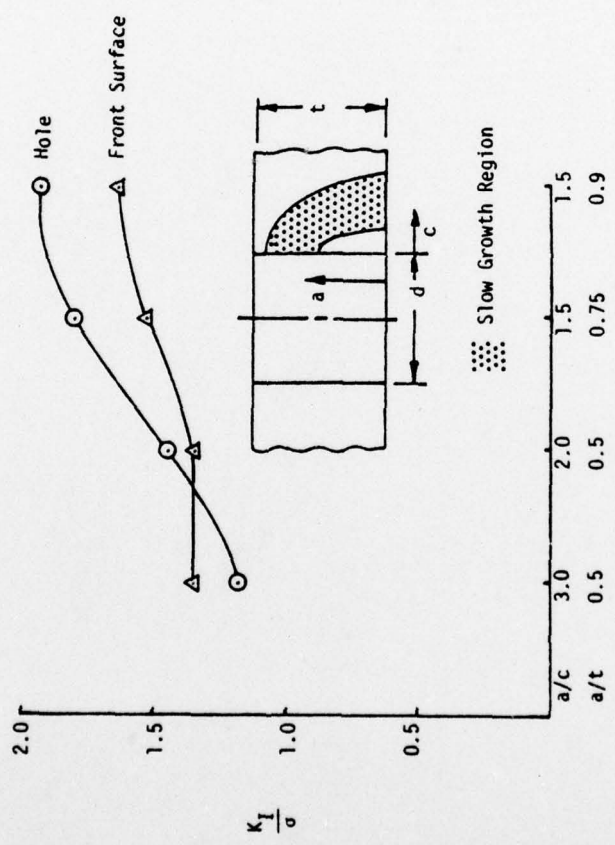


Figure 6.25 Parametric Plot of Theory to Approximate Slow Growth,  
Single Corner Crack,  $d/t=1.0$

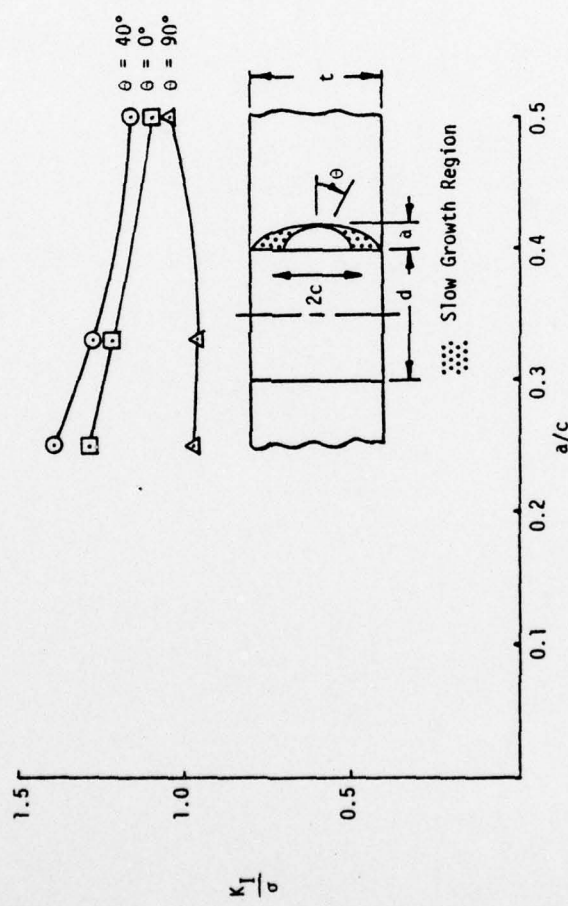


Figure 6.26 Parametric Plot of Theory to Approximate Slow Growth, Embedded Crack,  $a/t=0.125$ ,  $d/t=1.0$

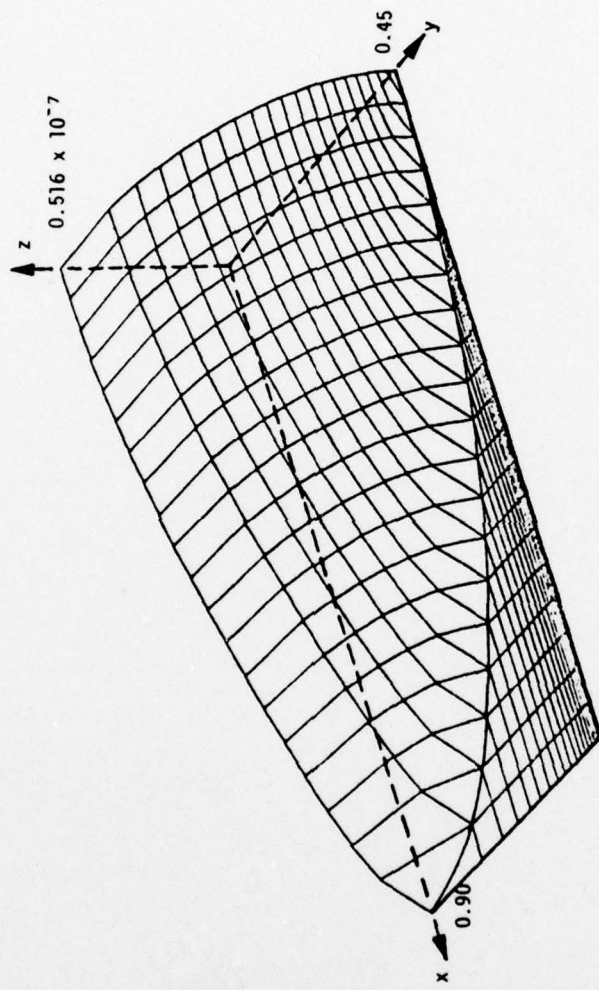


Figure 7.1 Crack Opening Displacement, Single Corner Flaw Adjacent to Open Fastener Hole,  
 $a/c = 2.0$ ,  $a/t = 0.9$

## APPENDIX A

FINITE ELEMENT-ALTERNATING METHOD CALCULATIONS  
AND STRESS FUNCTION COEFFICIENTS

Case	Crack Configuration	d/t	Q/P	a/t	a/c
1	Single corner	1.0	0.0	0.5	2.0
2				0.5	1.5
3				0.5	0.75
4				0.5	0.5
5				0.5	3.0
6			0.376	0.446	
7			0.9	3.0	
8			0.9	2.0	
9			0.9	1.5	
10			0.75	2.0	
11			0.75	1.5	
12			0.25	0.25	
13			0.125	0.25	
14			0.2	2.0	
15			0.45	0.9	
16			0.55	1.1	
17			0.3	1.4	
18			0.4	1.4	
19			0.5	1.4	
20			0.6	1.4	
21			0.7	1.4	

Case	Crack Configuration	d/t	Q/P	a/t	a/c
22	Single corner	1.0	0.0	0.8	1.4
23				0.85	2.5
24				0.25	0.5
25		0.1		0.25	0.5
26		0.5		0.25	0.5
27		1.0		0.25	0.5
28		1.0		0.85	2.5
29		1.0		0.2	0.5
30		1.0		0.2	2.0
31		1.0		0.3	0.5
32		0.5	0.0	0.75	3.0
33		0.5	0.0	0.25	0.5
34		0.5	1.0	0.25	0.5
35	Double corner	1.0	0.0	0.85	2.5
36				0.125	0.25
37				0.25	0.5
38				0.5	0.75
39				0.9	2.0
40				0.75	2.0
41				0.5	2.0
42				0.5	1.5
43				0.75	1.5
44				0.9	1.5
45				0.15	0.5
46				0.2	0.5
47		0.1	0.23		0.6

<u>Case</u>	<u>Crack Configuration</u>	<u>d/t</u>	<u>Q/P</u>	<u>a/t</u>	<u>a/c</u>
48	Double corner	1.0	1.0	0.25	0.6
49			1.0	0.85	2.5
50			1.0	0.125	0.25
51			1.0	0.25	0.5
52		0.5	0.0	0.21	0.75
53		0.5	0.0	0.75	3.4
54		0.5	1.0	0.25	0.5
55	Embedded	1.0	0.0	0.125	0.5
56				0.125	0.25
57				0.125	0.33
58				0.1875	0.5
59				0.25	0.67
60				0.25	0.75
61				0.375	0.75
62				0.25	0.5
63			1.0	0.125	0.5
64		0.5	0.0	0.125	0.5
65		0.5	1.0	0.125	0.5

## COEFFICIENTS OF THE STRESS FUNCTION

CASE	C00	C10	C01	C20	C11	C02	C30	C21	C12	C03
1	+5342E-09	+953E-10	+1043E-10	+7479E-11	+7754E-12	+2466E-11	+3667E-11	+1323E-11	+1613E-11	+2039E-12
2	+8307E-09	+1199E-09	+2237E-10	+1074E-10	+5111E-12	+7177E-11	+5631E-11	+3156E-11	+3277E-11	+9500E-12
3	+2235E-08	+1436E-09	+1624E-09	+9686E-10	+5473E-10	+2310E-10	+3071E-10	+3327E-10	+2581E-10	+1322E-10
4	+3797E-08	+6296E-09	+2137E-09	+4347E-09	+2249E-09	+3331E-10	+2270E-09	+1666E-09	+8577E-10	+2107E-10
5	+2745E-09	+6318E-10	+5061E-11	+4589E-11	+4361E-12	+4611E-12	+1737E-11	+4499E-12	+2758E-12	+2411E-13
6	+1672E-08	+2514E-09	+9221E-10	+1573E-09	+5853E-10	+8536E-11	+6718E-10	+4139E+00	+1715E-13	+3781E-13
7	+1459E-08	+5651E-09	+1477E-10	+6253E-10	+1393E-10	+8598E-11	+7844E-10	+1688E-10	+9371E-11	+1153E-11
8	+2300E-08	+8355E-09	+6211E-10	+1145E-09	+4564E-10	+6513E-10	+1456E-09	+5622E-10	+4140E-10	+8591E-11
9	+4395E-08	+10145E-08	+1666E-09	+1747E-09	+1373E-09	+1190E-09	+2111E-09	+1330E-09	+1080E-09	+3522E-10
10	+1666E-08	+4210E-09	+3170E-10	+4905E-10	+6308E-11	+1713E-10	+4642E-10	+1737E-10	+1327E-10	+2687E-11
11	+2627E-08	+5100E-09	+9233E-10	+7636E-10	+4320E-10	+4950E-10	+7027E-10	+4207E-10	+3697E-10	+1152E-10
12	+1061E-08	+2270E-09	+4684E-10	+2146E-09	+4328E-10	+7136E-12	+1146E-09	+1229E-10	+7989E-11	+4346E-12
13	+1433E-09	+1396E-10	+4533E-11	+6661E-11	+4215E-12	+2466E-13	+1199E-11	+2876E-12	+7282E-13	+4414E-14
14	+3655E-10	+3346E-11	+7116E-12	+8628E-13	+6590E-13	+2106E-13	+6645E-14	+5419E-14	+4053E-14	+5237E-15
15	+1279E-08	+6759E-10	+1687E-09	+2379E-10	+1274E-10	+1110E-10	+6299E-11	+9726E-11	+7589E-11	+5455E-11
16	+1719E-08	+2191E-09	+7918E-10	+2417E-10	+2246E-10	+3660E-10	+1511E-10	+1504E-10	+1638E-10	+6026E-11

CASE	C03	C10	C01	C20	C11	C02	C30	C21	C12	C03
17	$2151E-39$	$214E-10$	$4933E-11$	$1014E-11$	$6104E-12$	$7962E-12$	$2131E-12$	$1373E-12$	$1d39E-12$	$4d37E-13$
18	$4463E-29$	$5d32E-13$	$1259E-10$	$4007E-11$	$5373E-12$	$3216E-11$	$1520E-11$	$3672E-12$	$1115E-11$	$3282E-12$
19	$4148E-29$	$4273E-19$	$2495E-10$	$1126E-10$	$9134E-12$	$9463E-11$	$6505E-11$	$3735E-11$	$55d4E-11$	$12d8E-11$
20	$1545E-04$	$2410E-03$	$5333E-10$	$2934E-10$	$11302E-10$	$2145E-10$	$1433E-10$	$1262E-10$	$1229E-10$	$4153E-11$
21	$2396E-06$	$4153E-03$	$9139E-10$	$6069E-10$	$3629E-10$	$4611E-10$	$4230E-10$	$3277E-10$	$3041E-10$	$1052E-10$
22	$3523E-08$	$6624E-09$	$1507E-09$	$1173E-09$	$9033E-10$	$6676E-10$	$1143E-09$	$7966E-10$	$6331E-10$	$2455E-10$
23	$1661E-03$	$5d45E-09$	$2524E-10$	$6324E-10$	$11552E-10$	$1314E-10$	$7149E-10$	$2092E-10$	$1295E-10$	$1954E-11$
24	$5033E-09$	$3574E-13$	$2597E-10$	$1569E-10$	$3374E-11$	$1016E-11$	$3115E-11$	$2133E-11$	$9748E-12$	$2403E-12$
25	$6667E-09$	$3510E-10$	$2927E-10$	$2309E-10$	$5153E-11$	$1418E-11$	$3652E-11$	$2918E-11$	$11414E-11$	$3317E-12$
26	$1156E-08$	$1133E-10$	$5193E-10$	$4451E-10$	$13145E-10$	$2654E-11$	$7136E-11$	$5566E-11$	$1911E-11$	$5495E-12$
27	$1724E-06$	$-2.52E-16$	$6332E-10$	$7127E-10$	$-2331E-10$	$2866E-11$	$-1156E-10$	$8877E-11$	$2875E-11$	$9119E-12$
28	$5726E-18$	$1637E-05$	$-4700E-10$	$2116E-09$	$-1153E-09$	$5562E-10$	$-2932E-09$	$6267E-10$	$5150E-10$	$6407E-11$
29	$9461E-09$	$1030E-13$	$3546E-10$	$2375E-10$	$-4020E-11$	$1166E-11$	$-2524E-11$	$2263E-11$	$5903E-12$	$1953E-12$
30	$1414E-09$	$1221E-15$	$2758E-11$	$3787E-12$	$2274E-12$	$8115E-13$	$-2722E-13$	$2264E-13$	$1528E-13$	$1973E-14$
31	$2805E-06$	$-1161E-09$	$1426E-09$	$1721E-09$	$-7371E-10$	$6016E-11$	$-3543E-10$	$2518E-10$	$9567E-11$	$2924E-11$
32	$6703E-09$	$2243E-09$	$7935E-11$	$-1560E-10$	$-3352E-11$	$2603E-11$	$-2512E-10$	$5843E-11$	$2961E-11$	$3153E-12$

CASE	C00	C10	C01	C02	C11	C02	C30	C21	C12	C03
33	*3923E-19	*3285E-10	*1919E-10	*1164E-10	*5069E-11	*6111E-12	*2958E-11	*1757E-11	*1102E-11	*2486E-12
34	*2274E-08	*0497E-10	*9609E-10	*1102E-09	*4573E-10	*1944E-11	*1372E-10	*1432E-10	*4597E-11	*1717E-11
35	*1E12E-04	*4518E-09	*1270E-09	*8340E-10	*1662E-10	*1405E-10	*5541E-10	*3024E-10	*1694E-10	*1142E-11
36	*1265E-09	*3145E-10	*6675E-11	*7411E-11	*3110E-12	*1411E-13	*6740E-12	*4715E-12	*7395E-13	*1386E-14
37	*4615E-19	*5462E-10	*4214E-10	*1715E-10	*2951E-11	*1152E-11	*1554E-11	*3156E-11	*1024E-11	*1315E-12
38	*2261E-08	*4521E-09	*3765E-09	*1173E-09	*1831E-10	*2372E-10	*2473E-10	*3980E-10	*3637E-10	*6492E-11
39	*2839E-08	*1539E-08	*2432E-09	*1715E-09	*3332E-10	*4508E-10	*1171E-09	*8082E-10	*5536E-10	*5717E-11
40	*1616E-19	*6704E-09	*1249E-09	*6654E-10	*2636E-10	*1957E-10	*3439E-10	*2423E-10	*1771E-10	*1524E-11
41	*4955E-09	*1449E-09	*3037E-10	*9421E-11	*6529E-11	*2506E-11	*2424E-11	*1917E-11	*1565E-11	*7796E-13
42	*7816E-19	*1224E-09	*6549E-10	*1389E-10	*1224E-10	*7735E-11	*3737E-11	*4246E-11	*4360E-11	*4479E-12
43	*2051E-08	*3356E-09	*2825E-09	*1125E-09	*3642E-10	*5549E-10	*5331E-10	*5519E-10	*4943E-10	*7266E-11
44	*4732E-09	*1335E-08	*3938E-09	*2935E-09	*7315E-10	*1303E-09	*1652E-09	*1690E-09	*1569E-09	*3011E-10
45	*1055E-19	*1209E-13	*6895E-11	*1463E-11	*6622E-12	*8435E-13	*4451E-13	*1564E-12	*3226E-13	*2625E-14
46	*2423E-09	*3060E-10	*1867E-10	*5762E-11	*1942E-11	*3942E-12	*3207E-12	*3152E-12	*2214E-12	*2023E-13
47	*3834E-09	*5099E-10	*3224E-10	*8393E-11	*3276E-11	*1007E-11	*2309E-12	*1366E-11	*4149E-12	*7294E-13
48	*1297E-08	*1287E-09	*1203E-09	*3805E-10	*3106E-11	*3413E-11	*1878E-11	*7196E-11	*1814E-11	*4427E-12

AD-A045 349

AIR FORCE INST OF TECH WRIGHT-PATTERSON AFB OHIO  
SURFACE CRACKS EMANATING FROM FASTENER HOLES. (U)  
1976 T E KULLGREN  
AFIT-CI-77-21

UNCLASSIFIED

F/6 20/11

NL

3 OF 3  
AD  
A045349



END

DATE

FILED

11-77

DDC

CASE	C00	C10	C01	C20	C11	C02	C30	C21	C12	C03
49	+5525E-03	+2735E-04	+2520E-04	+2301E-04	+5072E-10	+5796E-10	+2445E-09	+3313E-16	+6781E-13	+3454E-11
50	+4514E-09	+7223E-10	+2306E-10	+3349E-10	+1120E-11	+2316E-13	+2668E-11	+2059E-11	+2374E-12	+7745E-14
51	+1560E-08	+1560E-09	+1404E-09	+7551E-13	+5103E-11	+3366E-11	+5615E-11	+1313E-10	+2863E-11	+5449E-12
52	+1368E-19	+1193E-20	+1224E-10	+1259E-11	+6499E-12	+5019E-12	+6367E-13	+2179E-12	+9401E-13	+2204E-13
53	+6666E-13	+34975E-09	+2370E-10	+2939E-10	+9129E-12	+2497E-11	+2555E-10	+6676E-11	+3360E-11	+1976E-12
54	+2415E-13	+6046E-09	+1677E-09	+1639E-03	+8665E-11	+3032E-11	+5005E-11	+2504E-11	+6434E-11	+1608E-11
55	+5532E-10	0	+1464E-11	+1734E-12	0	+1114E-12	0	+1634E-14	0	+1481E-14
56	+1991E-19	0	+2769E-11	+3332E-11	0	+2473E-12	0	+3779E-13	0	+3323E-14
57	+1423E-19	0	+2181E-11	+7675E-12	0	+1750E-12	0	+3593E-14	0	+2436E-14
58	+2692E-09	0	+3646E-11	+1677E-11	0	+8440E-12	0	+9214E-13	0	+3269E-13
59	+4125E-09	0	+5601E-11	+2775E-11	0	+2525E-11	0	+3117E-12	0	+1663E-12
60	+3485E-19	0	+5176E-11	+1718E-11	0	+2201E-11	0	+2114E-12	0	+1445E-12
61	+1166E-19	0	+1556E-11	+3111E-10	0	+1904E-10	0	+6416E-11	0	+2114E-11
62	+6229E-19	0	+4893E-11	+1373E-10	0	+3637E-11	0	+1592E-11	0	+2552E-12
63	+3607E-19	0	+4785E-11	+6517E-12	0	+6091E-12	0	+4417E-14	0	+4441E-14
64	+6826E-13	0	+1161E-11	+2313E-12	0	+9235E-13	0	+5182E-14	0	+1507E-14
65	+4270E-19	0	+6946E-11	+1297E-11	0	+5762E-12	0	+1229E-13	0	+3171E-14

APPENDIX B  
CRACK OPENING DISPLACEMENT EQUATION

$$w = -2(1-\eta) \left\{ -C_{00} \frac{4(\mu\nu)^{1/2}}{a^2 b^2} - C_{01} \frac{4y(\mu\nu)^{1/2}}{a^2 b^4} \right. \\ - C_{02} \left[ \frac{8(\mu\nu)^{3/2}}{a^4 b^6} - \frac{8y^2(\mu\nu)^{1/2}}{a^2 b^6} \right] - C_{03} \left[ \frac{12y(\mu\nu)^{3/2}}{a^4 b^8} - \frac{16y^2(\mu\nu)^{1/2}}{a^2 b^8} \right] \\ - C_{10} \frac{4x(\mu\nu)^{1/2}}{a^4 b^2} - C_{11} \frac{4(\mu\nu)^{1/2}}{a^4 b^4} - C_{12} \frac{8x(\mu\nu)^{3/2}}{a^6 b^6} \\ - C_{20} \left[ \frac{8(\mu\nu)^{3/2}}{a^6 b^4} - \frac{16x^2(\mu\nu)^{1/2}}{a^6 b^2} \right] - C_{21} \left[ \frac{8y(\mu\nu)^{3/2}}{a^6 b^6} - \frac{16x^2y(\mu\nu)^{1/2}}{a^6 b^4} \right] \\ \left. - C_{30} \left[ \frac{24x(\mu\nu)^{3/2}}{a^8 b^4} - \frac{16x^2(\mu\nu)^{1/2}}{a^8 b^2} \right] \right\}$$

where:  $\mu\nu = a^2b^2 - b^2x^2 - a^2y^2$

$a$  = crack semi-major axis

$b$  = crack semi-minor axis

$x$  = crack coordinate in major axis direction, origin at crack center

$y$  = crack coordinate in minor axis direction, origin at crack center

$\eta$  = Poission's ratio (Stress function coefficients in Appendix A generated with  $\eta = 0.25$ )

## APPENDIX C

### BENCHMARK PROBLEM

As three-dimensional fracture mechanics becomes more sophisticated and capable of producing usable solutions, the need arises for a standard problem configuration, or a so-called "benchmark problem," which can be used by all investigators in the field. Such a problem statement is necessary so that solutions obtained by the many varied methods can be compared, one against another, without the uncertainties of interpolation or extrapolation of results.

The Workshop on Three-Dimensional Fracture Analysis held in Columbus, Ohio, April 26-28, 1976, and attended by most of the leading three-dimensional fracture mechanics investigators in the United States, defined several of these "benchmark problems." For the case of a flaw adjacent to a fastener hole in an infinite plate, the following configuration was agreed upon:

Single corner flaw

$$a/c = 2.0$$

$$a/t = 0.2$$

$$d/t = 1.0$$

The method described earlier in this paper was applied to the above stated "benchmark problem" and results are shown in the figures that follow.

For the open fastener hole case, with remote uniaxial plate loading, Figure C-1 shows plotted values of magnification factor versus parametric angle from the front surface of the plate while Table C-1 lists these same values in tabular form for each ten degrees of

parametric angle. Similarly, Figure C-2 and Table C-1 show results for the case of all the remote load transferred to the fastener.

Several interesting observations can be made regarding the "benchmark problem" solutions presented in this section. The open fastener hole case displays a higher stress intensity factor at the front surface and intermediate locations than at the hole. This same trend was also noted earlier in this work with other flaws having high  $a/c$  and low  $a/t$  ratios. Figure C-3 is a parametric plot of  $K_I/\sigma$  versus  $a/t$  for  $a/c = 2.0$  and reversal in the location of maximum stress intensity is clearly seen to occur at an  $a/t$  ratio very close to that of the "benchmark problem." Of perhaps more significance is a similar trend seen in the problem of all the remote load transferred to the fastener. Since the crack dimension is so small along the front surface and the crack shape is slim, the entire crack lies in an area of elevated stress. Thus, the crack does not extend out into an area where the steep stress gradient would cause a dramatic reduction in the stress intensity factor in the vicinity of the front surface. With respect to the "benchmark problem" solutions presented in this section, should  $a/c$  be slightly decreased (holding  $a/t$  constant) or  $a/t$  slightly increased (holding  $a/c$  constant), it seems apparent that the location of maximum stress intensity would shift to the hole intersection.

TABLE C-1  
BENCHMARK PROBLEM RESULTS

Parametric Angle From Front Surface	Open Fastener Hole	100% Load Transfer to Fastener Hole
	$\frac{K_I}{\sigma\sqrt{\pi a}}$	$\frac{K_I}{\sigma_b\sqrt{\pi a}}$
0	1.2684	0.4073
10	1.3223	0.4211
20	1.3450	0.4244
30	1.3468	0.4210
40	1.3353	0.4138
50	1.3133	0.4043
60	1.2799	0.3923
70	1.2357	0.3780
80	1.1897	0.3638
90	1.1574	0.3544

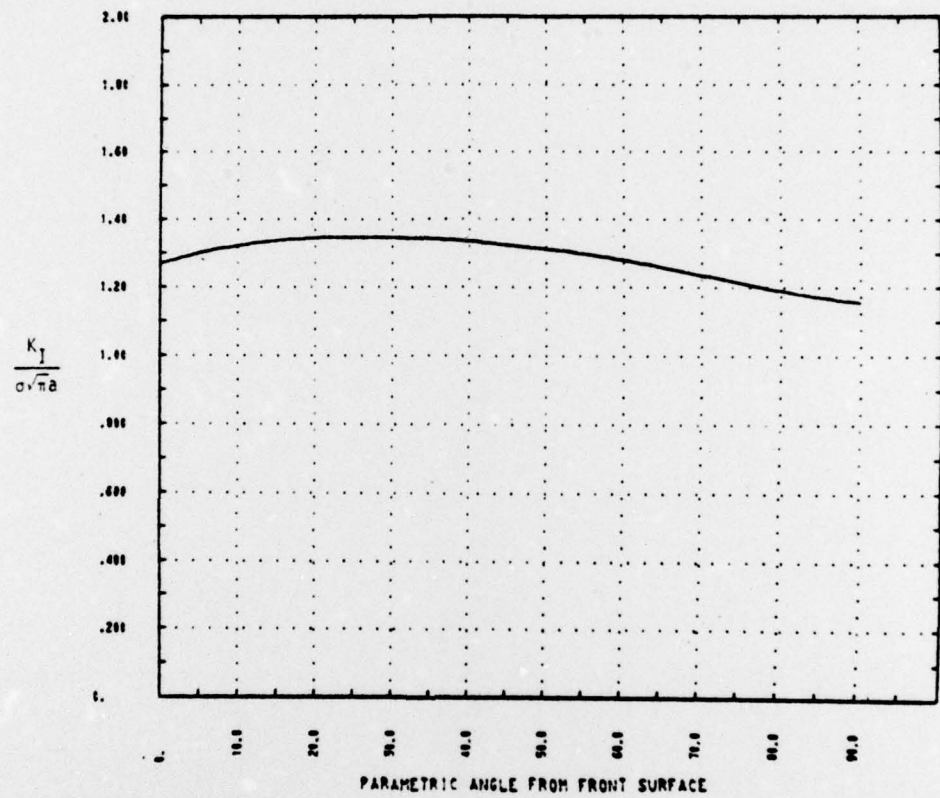


Figure C-1 Magnification Factor Versus Angle from Front Surface  
 Single Corner Crack, Benchmark Problem  
 $a/c=2.0$ ,  $a/t=0.2$ ,  $d/t=1.0$ ,  $Q/P=0.0$

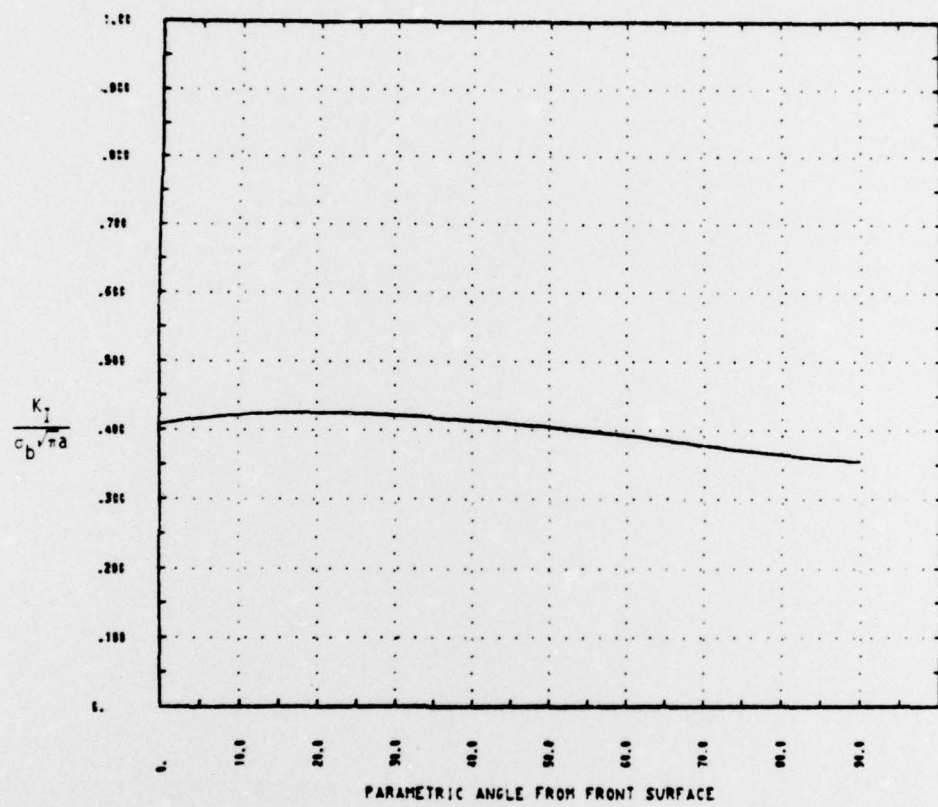


Figure C-2 Magnification Factor Versus Angle from Front Surface  
 Single Corner Crack, Benchmark Problem  
 $a/c=2.0$ ,  $a/t=0.2$ ,  $d/t=1.0$ ,  $Q/P=1.0$

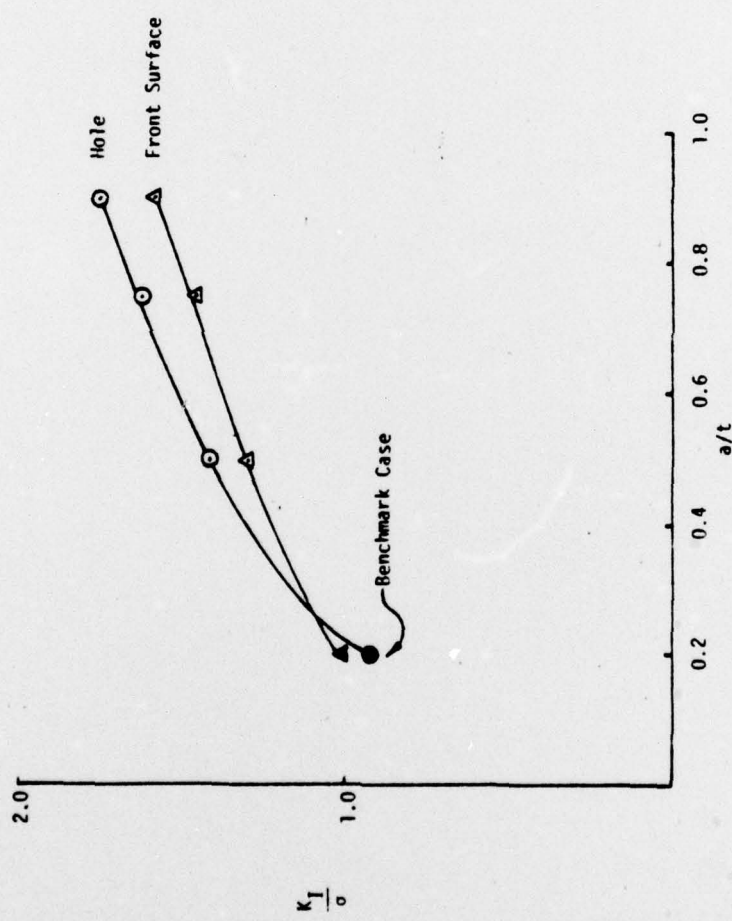


Figure C-3 Parametric Plot of Theoretical Results, Single Corner Cracks, Open Hole,  $a/c=2.0$